Universidade de Lisboa
Faculdade de Ciências
Departamento de Física

A 31P MR Spectroscopy Study on Rat Models of Liver Disease

Frederico Ribeiro da Silva Severo

Dissertação
Mestrado Integrado em Engenharia Biomédica e Biofísica
Perfil de Radiacões em Diagnóstico e Terapia

2014

Universidade de Lisboa
Faculdade de Ciências
Departamento de Física

A 31P MR Spectroscopy Study on Rat Models of Liver Disease

Frederico Ribeiro da Silva Severo

Dissertação
Mestrado Integrado em Engenharia Biomédica e Biofísica
Perfil de Radiacões em Diagnóstico e Terapia

Orientador externo: Professor Doutor Maurits Jansen
Orientador interno: Professor Doutor Hugo Ferreira

2014

Resumo

O objectivo deste projecto assenta no desenvolvimento e optimização de técnicas de Espectroscopia por Ressonância Magnética com Fósforo-31 (^{31}P MRS), para a avaliação do conteúdo metabólico e descoberta de biomarcadores em modelos de patologia hepática. A Espectroscopia por Ressonância Magnética é uma técnica não invasiva utilizada para estudos metabólicos, qualitativos e quantitativos. Esta técnica permite, especificamente no caso do Fósforo-31, a avaliação e quantificação de metabolitos cuja composição contenha Fósforo, como é caso da Fosfocreatina, Adenosinatrifosfato ou o Fosfato Monosódico. Através da avaliação qualitativa e quantitativa destes metabolitos há como objectivo a asserção de diversas patologias e alterações metabólicas de forma consistente, segura e não invasiva.

O estudo tem como base a optimização de sequências pré-existentes, como ISIS (Image Selected In-vivo Spectroscopy), CSI (Chemical Shift Imaging) e SPULS (Single Pulse and 1D acquire), assim como o desenvolvimento de uma sequência de localização 1D sem auxílio de gradientes. Esta sequência, denominada SATSP (SATurated Single Pulse), tem como base a sequência SPULS, que consiste na utilização de um único pulso de excitação (*hard pulse*) para a obtenção de informação espectroscópica, acrescentado-lhe um pulso de saturação prévio (neste caso específico baseado na sequência PRESS). O objectivo é proceder à saturação de toda a área não desejada antes da excitação do tecido e aquisição do sinal. O pulso de excitação é então aplicado uniformemente, sendo possível obter sinal apenas da região não saturada. Assim, todo o sinal adquirido terá como origem a área de interesse que, em última instância, deverá corresponder ao fígado.

O projecto inclui o design e posterior utilização de uma fantoma (denominado Liver Phantom) de dois compartimentos cujo objectivo é simular um corte transversal da região abdominal de um rato Sprague Dawley, contendo uma primeira camada simulando pele/músculo/gordura (1º compartimento, com um volume de 10ml situado em contacto com a *surface coil,* contendo Fosfato Dissódico, 40mM), e uma segunda camada simulando o fígado (2º compartimento, com um volume de 35ml, situado do lado oposto à *surface coil,* contendo Ácido Fenil Fosfórico, 10mM). A escolha dos componentes teve como base a sua fácil distinção a nível de frequência de ressonânica (apresentam-se bastante distantes no espectro), e o facto de ambas as substâncias gerarem apenas um pico visível no espectro.

Foram também adquiridos dados experimentais in-vivo (ratos Sprague-Dawley, grupo de controlo n=2, grupo de modelo de doença n=2), os quais foram posteriormente comparados com artigos de referência. Aos ratos pertencentes ao grupo de modelo de doença, administrou-se, por via intraperitoneal, Tetracloreto de Carbono (CCl4) durante um período de 8 semanas, duas vezes por semana,

causando fibrose hepática avançada ou início de cirrose.

Para ambas as situações, in vitro e in vivo, foram descritos protocolos experimentais específicos, que detalham a ordem dos acontecimentos, os métodos de calibração e possibilidades de shimming (manual e automático).

Todos os dados experimentais foram adquiridos especificamente para este projecto, utilizando um scanner pré-clínico de pequeno diâmetro Varian 7T, Surface Coil Tx/Rx Doty30 ($^{1}H/^{31}P$) e software de aquisição vNMRj 3.2, sendo os resultados processados com o auxílio do software jMRUI e Matlab.

Todo o hardware utilizado foi cuidadosamente descrito, começando pelo scanner e os seus vários componentes, até ao material utilizado na preparação da aquisição e durante a mesma. Foram especificadas as diferenças de material utilizado in vitro e in vivo, de modo a estabelecer um contraste de complexidade entre as duas modalidades.

Relativamente à análise dos resultados, o método de processamento de dados utilizado foi o AMARES (Advanced Method for Accurate, Robust and Efficient Spectral fitting), que tem em conta pârametros pré-estabelecidos pelo utilizador. Uma descrição detalhada do método de análise encontra-se disponível nesta dissertação, desde a preparação dos dados, ao nível da correcção de fase, *zero filling* ou truncagem, até à escolha de pârametros a utilizar com o algoritmo AMARES.

No contexto de análise espectroscópica in-vivo ao fígado, e no caso da espectroscopia com Fosfóro-31, foram 6 os metabolitos tidos em conta, nomeadamente Fosfomonoesteres (PME), Fosfodiesteres (PDE), Fosfato Inorgânico (Pi), Adenosina Trifosfato (ATP-α, β, e γ), Fosfocreatina (PCr) e Dinucleótido de Nicotinamida e Adenina (NADH). Variações na concentração e rácios de PDE, PME, Pi e ATP foram previamente referenciadas como possíveis indicadores de alterações patológicas na actividade hepática e, como tal, foram atentamente estudadas.

Os resultados indicaram uma variação no rácio PME/(PME+PDE), denominado Anabolic Charge, entre os dois grupos em estudo. Especificamente, o grupo de controlo apresenta valores de AC mais baixos do que o grupo de modelo de doença. Existe também um aparente decréscimo de concentração absoluta de PDE no grupo de modelo de doença, embora a falta de dados comparativos impossibilite uma maior certeza neste parâmetro . Não foram detectadas variações consideradas significativas no rácio de ATP e Pi.

Foi sugerido o aumento da amostra de ambos os grupos (controlo e modelo de doença) de modo a obter resultados que expressem de uma forma mais segura e significativa as diferenças entre os dois grupos, assim como um estudo

longitudinal que incluísse a recolha histológica de daos em simultâneo com o estudo espectroscópico. A utilização de uma Volume Coil em combinação com a Surface Coil utilizada foi considerada como uma das possíveis mais valias a acrescentar no futuro.

Paralelo ao estudo metabólico previamente descrito foi criado um mapa de Flip Angle para a Surface Coil Doty30, utilizada durante o estudo, o qual evidenciou problemas de alcance e baixa homogeneidade de campo, assim como um estudo inicial de quantificação metabólica absoluta.

O mapa de *Flip Angles* da Surface Coil Doty30 foi criado através do método do rácio do ângulo duplo. Para este médodo são adquiridas duas imagens *Gradient Echo,* a primeira com um flip angle arbitrário *x*, e outra com um flip angle *2x*. Através do rácio entre a magnitude de ambas as imagens adquiridas é possível chegar ao flip angle efectivo aplicado na amostra/tecido/etc. Para estas aquisições foi utilizado um pequeno fântoma de plástico com cerca de 50ml de fosfato monosódico, com concentração 1M. Para a produção do mapa de *Flip Angles* foi desenvolvido de raiz um código *Matlab* que gera automaticamente os mapas, tendo como input as imagens de *Gradient Echo* adquiridas com flip angle x e 2x. O estudo mostrou um curto alcance na aquisição de sinal por parte da surface coil, cerca de 2cm de profundidade, e uma fraca homogeneidade de campo, algo esperado com uma coil deste tipo. Para estudos futuros foi sugerida a utilização combinada de uma volume coil para aplicação dos pulsos RF (maior homogeidade de campo), e uma surface coil para a aquisição do sinal (maior próximidade).

Para o estudo de quantificação metabólica absoluta, foi utilizado um método que envolve a troca do espécime após a aquisição in vivo, e a posterior replicação das condições iniciais para nova aquisição, desta vez utilizando um fântoma com uma concentração fosfórica conhecida. Foi utilizado um fântoma cilíndrico de vidro, com Ácido Fenil Fosfórico, 50mM. Este método foi apenas aplicado a um dos ratos do grupo de modelo de doença, servindo assim como prova de conceito para quantificação absoluta, não tendo havido comparação entre os dois grupos. Os resultados mostraram-se promissores, sendo um dos objectivos futuros a aplicação deste método em todos os estudos em que a quantificação absoluta possa ser benéfica. Como desvantagem, o método descrito implica a repetição das sequências utilizadas in vivo, elevando para o dobro o tempo total de aquisição.

Concluiu-se que a Espectroscopia por Ressonância Magnética se apresenta como uma técnica viável a nível de quantificação metabólica não invasiva.

Palavras-chave: espectroscopia em ressonância magnética com fósforo 31, *saturated single pulse sequence*, *chemical shift imaging*, fibrose hepática, cirrose, biomarcadores de patologia hepática.

Abstract

The overall aim of the project is to evaluate the role of ^{31}P Magnetic Resonance Spectroscopy in preclinical models of liver fibrosis and cirrhosis and to determine the utility of ^{31}P MRS as a non-invasive test for biomarkers. Specifically, two main problems are to be addressed: the possibility of MRS providing reliable information on liver functional status in preclinical models, to the point of rendering multiple time point sampling (biopsy) obsolete; and identifying novel biomarkers that distinguish control and disease model groups. This study includes both In Vitro (with a specific designed liver phantom) and In Vivo data (Sprague-Dawley rats, control group n = 2, disease model group n =2). Several pulse sequences were tested, with more relevance given to CSI (Chemical Shift Imaging) and SATSP (Saturated Single Pulse, a newly made combination of single pulse acquisition with prior use of saturation pulses) sequences. Results show some degree of variation in metabolite ratio between control and disease model groups, specifically with PME and PDE ratios. A bigger sample size for both control and disease model groups is proposed to further verify these claims.

Keywords: 31P magnetic resonance spectroscopy, saturated single pulse sequence, chemical shift imaging, liver fibrosis, cirrhosis, biomarkers of liver disease.

Acknowledgements

A huge thank you to Dr. Maurits Jansen, for teaching me almost everything I know about this subject. For everyone else at the University of Edinburgh, Ross Lennon, Gavin Merrifield, Gregorio Naredo and Ian Marshall.

Thank you Hugo Ferreira, for helping me with my bachelor's dissertation, and once again with this one.

To Marta Ribeiro, designer extraordinaire, who helped me go from a rough sketch of a 2 compartment phantom to a perfectly beautiful (and printable) 3D model, a massive thank you.

Special thanks to Salomé Matos for inviting me to her home and letting me sleep on her couch during the first few weeks of my internship. Edinburgh is a very cold city in February, your heater was nothing short of life-saving.

Thank you Natalia Equihua, José Macena and Dominik Brucher for all the nights we spent having dinner and listening to jazz music. Extra thanks to Natalia for the rainy weekends and homemade Pesto.

To all my friends in London at the time, Ana Figueira, Débora Salvado, João Monteiro, Jo-Anne Tan, and a few others I can't remember right now, thanks for all the technical help, conversations, fun times and general stupidity.

To my very lovely and Indonesian best friend Nabila Wibowo, thank you for keeping in touch almost every day.

To Catarina Freitas, for putting up with me.

And last but never least, I would like to thank my parents, for all the help through the years.

Table of Contents

Abbreviations and Symbols

AMARES	Advanced Method for Accurate, Robust and Efficient Spectral fitting of MRS data with use of prior knowledge
AMP	Adenosine monophosphate
ADP	Adenosine diphosphate
ATP	Adenosine Triphosphate
B0	Main Magnetic Field (in Tesla)
B1	Magnetic radiofrequency field of the transmitter (in Tesla)
CCl4	Carbon tetrachloride
CSI	Chemical Shift Imaging
DP	Disodium Phosphate
EP	Excitation Pulse
EPI	Edinburgh Preclinical Imaging
FID	Free induction decay
FFT	Fast Fourier transform
FOV	Field of View
GUI	Graphic User Interface
IP	Inversion Pulse
ISIS	Image Selected in vivo spectroscopy
MRI	Magnetic Resonance Imaging
MRS	Magnetic Resonance Spectroscopy
NMR	Nuclear Magnetic Resonance
OVS	Outer Volume Suppression
PCr	Phosphocreatine
PPA	Phenylphosphonic Acid
PPM	Parts per Million
PRESS	Point Resolved Spectroscopy
ROI	Region Of Interest
RF	Radiofrequency
SNR	Signal to Noise ratio
SP	Saturation Pulse
SPULS	Single Pulse and 1D acquire
SPECIAL	SPin ECho, full Intensity Acquired Localized spectroscopy
STEAM	Stimulated Echo Acquisition Mode
SVD	Singular Value decomposition
T1	Longitudinal relaxation time constant (in seconds)
T2	Transverse relaxation time constant (in seconds)
TE	Echo Time (in seconds)
TMS	Tetramethylsilane
TR	Repetition Time (in seconds)

List of Figures

List of Tables

1. Introduction

1.1 Aim of the work

Cirrhosis is a diffuse condition, characterized by extensive fibrosis and nodule formation, vascular distortion and liver cell dysfunction [1]. As a result of alterations in the liver microcirculation mediated by myofibroblast-induced sinusoidal constriction, vascular distortion and shunt formation related to scar deposition, portal hypertension (or PHT) develops in the diseased liver and is responsible for the major clinical sequelae associated with cirrhosis such as ascites, variceal hemorrhage, encephalopathy and renal failure [1][2][3].

In human subjects, and regardless of the cause, patients with chronic liver disease may develop liver fibrosis, which can then progress to cirrhosis. In early stages there are no palpable or clear clinical manifestations of liver fibrosis, a fact that becomes even more complicated if we consider that the clinical manifestations of cirrhosis vary from no symptoms at all to liver failure [4].

Death rates from cirrhosis are increasing rapidly worldwide but, to date, no anti-fibrotic therapies have been approved for use in humans and the standard pharmacological therapy for PHT (non-selective beta blockade) remains unsuccessful in around 60% of patients [2]. While there is an urgent need to develop novel therapies for this problem, it is also required to improve diagnose techniques used to monitor the progression of liver fibrosis and development of PHT (which are highly variable in patients), as well as assess the response and progression related to any interventional approach.

Liver biopsy and hepatic venous portal gradient measurement are still the most used techniques for assessing histology and PHT, respectively, but both are relatively complicated invasive procedures and consequently unsuitable for recurrent analysis of disease parameters in case of a lasting, unpredictable condition. The same limitations apply to animal models, where optimal tests for fibrosis and portal pressure require the killing of animals at serial time points to assess disease progression and severity, instead of allowing a longitudinal assessment in the same animal. As a result of these problems associated with biopsy and other invasive techniques, there has been a steady initiative to find effective non-invasive approaches to evaluate liver damage, including serological tests and several imaging modalities [3]. Still, none of these methods have been universally adopted as of yet and the search for reliable and repeatable biomarkers of disease activity and response to treatment continues. One of these techniques relies on the use of Nuclear Magnetic Resonance (NMR). Two distinct modalities of NMR, Magnetic Resonance Imaging (MRI) and Magnetic Resonance Spectroscopy (MRS), can be used to assess different parameters.

In terms of imaging, In Vivo MRI scanning allows the application of this technique to monitor liver injury in-vivo in clinically relevant animal models [4].

However, there is still minimal data regarding the utility of MRI in animal models of liver fibrosis [4]. The major potential advantage of MRI is that repeated measurements can be made in the same rodent, without killing the animal, thus allowing for a longitudinal assessment of the same animal. The anatomical condition of the affected structures can be evaluated using contrast agents, like gadolinium, or assessing visco-elastic parameters [5], evaluating structural and perfusional abnormalities in the diseased liver in a longitudinal manner (as in human disease). Other indicators of PHT such as splenomegaly, varices and ascites may also be detectable using contrast agents.

When it comes to understanding liver disease in a physiological sense, Phosphorous-31 magnetic resonance spectroscopy (^{31}P MRS) can be used as a non-invasive technique that provides information on hepatic phospholipid metabolism (Adenosine triphosphate, ATP) and hepatocyte energy state (several groups have already tested its use in patients with liver disease and in animal models [6][4]).

Previous studies have shown specific changes in metabolite ratios that are indicative of liver dysfunction, as these pathways are switched into a 'regeneration mode' in an attempt to repair the failing liver [4][7]. However, ^{31}P MR Spectroscopy needs further evaluation in animal models of cirrhosis in a strategic search for novel biomarkers.

The use of ^{31}P MR Spectroscopy has several key elements to be considered in order to get consistent, reliable results, ranging from choosing and optimizing the best possible spectroscopy sequence, improving said techniques for both phantom and In Vivo use, and picking the most appropriate method for data analysis. Inside each one of these there's an infinite amount of possibilities. What kind of phantom should be used? Would it be better to design it from scratch, and if so, what materials can be utilized, what form factor is the most appropriate? Will a standard pulse sequence fulfill our purpose; does it need to be slightly altered? Or does one need to program a totally new one? These are but a few questions intrinsic to the issue at hand.

With all this in mind, one main bullet point to retain is that this body of work will not be focused in one specific part of this process. While most essays tend to center around one particular area of study, be it MR spectroscopy data acquisition, sequence programming or data analysis, it is my intention to go through every step in a manner as meticulous as possible, thoroughly explaining every phase along the way.

1.2 Dissertation Outline

Without getting too much into the basics of magnetic resonance, there is a need for some important concepts to be assimilated before venturing into the actual study. And so, this report will start by describing concepts such as relaxation,

chemical shift or spin-spin coupling.

The next chapter, entitled "Animal models of liver fibrosis" serves both as an explanation of how the condition can be represented and how it translates from the human perspective to the animal model. A specific method to induce liver fibrosis, the CCl4 method, will be detailed.

Then, the MR setup used throughout this study will be carefully described, the various hardware components and combinations documented. Experimental protocols for both in vivo and in vitro follow. In terms of methods of data analysis, both the data preparation, ranging from phasing and apodization to zero filling, and data quantification, which algorithm to use and what parameters were chosen, will be addressed. AMARES, a spectral fitting algorithm with the use of prior knowledge, was used as the primary method of data analysis.

Afterward, all the relevant pulse sequences used during the course of this study are going to be described and detailed. Among this sequences is a custom made Saturated SPULS pulse sequence.

Next, I shall carry on by detailing all the phantoms used during the experiments, putting more emphasis in the creation of a 2 compartment phantom for ^{31}P MR Spectroscopy use, labeled Liver Phantom, from its conceptual stages to its final form and purpose. While not the only phantom used throughout the course of this study, it was by far the most utilized and, as so, deserves a more detailed overview. Two other (more simple) phantoms were used and both their form factors and characteristics will be shortly described as well.

Results are divided into two main sets, Phantom and In Vivo data, with each set split into several sub categories, depending on number of pulse sequences, parameters or subjects/groups in each set. In Vivo and Phantom results are presented separately as a way to address their conclusions, problems and solutions as separate entities. A general discussion is presented afterwards, as a way to compile the general deductions of this study. Some additional results, for absolute quantification and B1 mapping are shown as well, along with specific inferences made from the acquired results.

Finally, a small conclusion will bring this dissertation to an end.

2. Background in Magnetic Resonance Imaging

Nuclear Magnetic Resonance (or simply NMR) techniques involve the manipulation and observation of nuclear magnetic moments intrinsic to matter for generation of an image describing the structural properties of that matter, Magnetic Resonance imaging (MRI), or a spectrum depicting specific compounds present in the scanned sample, Magnetic Resonance Spectroscopy (MRS).

In this section, the physics underlying magnetic resonance techniques is explored. For more information on the topic, a rigorous reference on the subject is provided in *Magnetic Resonance Imaging: Physical Principles and Sequence Design* [8], whilst a more accessible, intuitive discussion may be found in *MRI in Practice* [9].

2.1 Nuclear Magnetic Resonance

Nuclear Magnetic Resonance operates most fundamentally by manipulating spin states of individual nuclei. While it is possible to have an in-depth quantum mechanical description dealing with the statistical distribution of spin states in the material, for the purposes of this report it is sufficient to begin with a classical description describing the net nuclear magnetic moment of the material, as presented in Webb, 1988 [10] and Kuperman and Kuperman, 2000 [11].

As per the classical description, an isolated proton with a charge +e and angular momentum I is initially considered. And so, as described by Maxwell's equations (presented by Maxwell in 1865 [12]), an electronic charge circulating in a conducting loop produces a magnetic field normal to the plane of current rotation. Considering the proton charge to be distributed and rotating along a central axis as a result of the angular momentum, a magnetic dipole moment *mp* antiparallel to the angular momentum vector (and hence, normal to the plane of charge circulation) results, ie, mp = I describes the gyromagnetic ratio, which for the simplified classic model is given by:

$$\gamma = \frac{e}{2m}$$

where m is the proton mass.

An external magnetic flux density B0 will exert a torque T on a magnetic dipole moment, causing the angular momentum to change at a rate equal to the torque, i.e.

$$T = m_p \times B_0$$

$$= \frac{d\mathbf{I}}{dt}$$

And hence,

$$\frac{dm_p}{dt} = \gamma m_p \times B_0$$

The result above is the Larmor equation, which describes the precession of the magnetic dipole moment *mp* about B0 with angular velocity

$$\omega_0 = -\gamma B_0$$

or

$$v_0 = \left(\frac{\omega_0}{2\pi}\right) = \left(\frac{\gamma}{2\pi}\right) B_0$$

In MRI applications, the static, homogeneous B0 field described here is presented by the main field magnet.

2.2 Relaxation Processes and the Bloch Equations

Whereas useful for understanding the MR phenomenon, the classical model presented here cannot explain many features relating to the interactions between nuclei. To overcome some such limitations, a set of phenomenological equations describing the dynamics of nuclear magnetization were proposed in [13].

These Bloch equations describe processes of relaxation of the net magnetization. Various such relaxation processes arise which lead to a fading of the MR signal after the initial excitation; these are largely dependent on the material and structure being observed, and as such their measurement allows characterization of the materials.

2.2.1 Longitudinal Relaxation (T1)

Longitudinal relaxation, also known as spin-lattice relaxation and represented as T1 relaxation, describes the transfer of energy from the spin system, primarily through interactions with adjacent spins in the lattice. This is largely related to mobility and tumbling of molecules in the material – therefore, the physical structure of the material and surrounding surfaces. The T1 relaxation is defined by the Bloch equation

$$\frac{dM_z}{dt} = \frac{M_0 - M_z}{T_1}$$

2.2.2 Transverse Relaxation (T2)

Transverse relaxation, also known as spin-spin relaxation and represented as T2 is loss of net magnetization from the *xy* plane. This is a result of loss of phase coherence due to small variations in the B0 field (and hence, the local

precessional frequency) due to the relationship between the nucleus and the molecular magnetic field, or exchange of spin state between two nuclei. In biological tissue, this process is significantly faster than longitudinal relaxation. Transverse relaxation is described by the remaining Bloch equations,

$$\frac{dM_{xz}}{dt} = -\frac{M_x}{T_2} + \gamma M_y B_0$$
$$\frac{dM_x}{dt} = -\frac{M_y}{T_2} - \gamma M_x B_0$$

In practice, the envelope of the FID is observed to decay at the effective T2 relaxation time T2*, which is always faster than T2. This has the added factor of phase loss due to macroscopic fluctuations due to magnetic field inhomogeneities.

$$\frac{1}{T_2^*} = \frac{1}{T_2} + \frac{\gamma \Delta B_0}{2}$$

When a spin system which has been allowed to dephase for a short period is inverted (perhaps by way of a 180° pulse), the direction of rotation relative to the rotating frame of reference is reversed and the dephased spins begin to rephase. Effects from relatively static macroscopic inhomogeneities (defining T2) are cancelled and an echo signal may be seen from the rephased spin system, attenuated at a rate determined by the T2 component. It is generally this echo signal which is used to produce an image.

2.3 Chemical Shift

Whenever we assume a macroscopic sample containing only one type of nuclear spin, its resonance frequency is solely given by v_0. If this were to be the case MR spectroscopy would be of minor importance in fields such as chemistry or medicine, as you would only be able to identify and quantify each specific chemical element and not distinct compounds with that particular element in it. Nuclei of the same element (or isotope) would resonate at the same frequency because of their identical gyromagnetic ratio. Luckily, however, the resonance frequency ω not only depends on the gyromagnetic ration γ and the external magnetic field *B0,* but it is highly sensitive to chemical environment of the nucleus under investigation [15][16]. This effect is commonly referred to as the chemical shift. This phenomenon is directly caused by shielding (also called screening) of nuclei from the external magnetic field by electrons surrounding them. When placed in an external magnetic field, electrons will rotate about *B0* in an opposite sense to the proton spin precession. Since this precession of electrons involves motion of charge, there will be an associated magnetic moment μ_e, in analogy to the existence to a nuclear magnetic moment. The electron magnetic moment opposes the primary applied magnetic field *B0.*

Therefore, the electrons will reduce the magnetic field that is sensed by the nucleus. This effect can be described in terms of an effective magnetic field B at the nucleus as:

$$B = B_0(1 - \sigma)$$

where σ is the shielding constant. σ is a dimension (normally expressed in parts per million (ppm)), which depends on the chemical environment of the nucleus. And so, the resonance condition can be modified to:

$$v = \left(\frac{\gamma}{2\pi}\right) B_0(1 - \sigma)$$

Chemical shifts are most often not represented in units of Hertz (Hz), as this would make chemical shift value dependent on magnetic field strength. Instead, chemical shifts are expressed in terms of parts per million (ppm). By convention, chemical shift δ is defined as:

$$\delta = \frac{v_{inv} - v_{ref}}{v_{ref}} \times 10^6$$

where V_{inv} and V_{ref} are the frequencies of the compound under investigation and of a reference compound, respectively. The reference compound should ideally be chemically inert and its chemical shift should be independent of external variables (temperature, ionic strength, etc) and more importantly, should produce a strong single resonance signal well separated from all other resonances. Two widely accepted reference compounds for 1H NMR are tetramethylsilane (TMS) and 2,2-dimethyl-2-silapentane-5-sulfonate to which the chemical shift δ = 0 is attributed. Unfortunately, these compounds are nowhere to be found in vivo, making those impossible to use as internal references. In the specific case of in-vivo ^{31}P MR Spectroscopy Phosphocreatine (PCr) tends to be used as an internal reference (0.00 ppm), due to both its widespread presence in the body and relative stability [14].

2.4 Spin–Spin Coupling

The MR resonance frequencies, or chemical shifts, give direct information about the chemical environment of nuclei, thereby greatly aiding in the unambiguous detection and assignment of compounds. The integrated resonance area under each peak is, in principle, directly proportional to the concentration of the compounds, thus making NMR a quantitative technique. An additional feature that can be observed in high-resolution NMR spectra is the splitting of resonances into several smaller lines, a phenomenon often referred to as scalar coupling, J coupling or spin-spin coupling [17]. Scalar coupling originates from the fact that nuclei with magnetic moments can influence each other, besides

directly through space (dipolar coupling) also through electrons in chemical bonds (scalar coupling).

Even though dipolar interactions are the main mechanism for relaxation in a liquid, there is no net interaction between nuclei since rapid molecular tumbling averages the dipolar interactions to zero. However, interactions through chemical bonds do not average to zero and give rise to the phenomenon of scalar coupling.

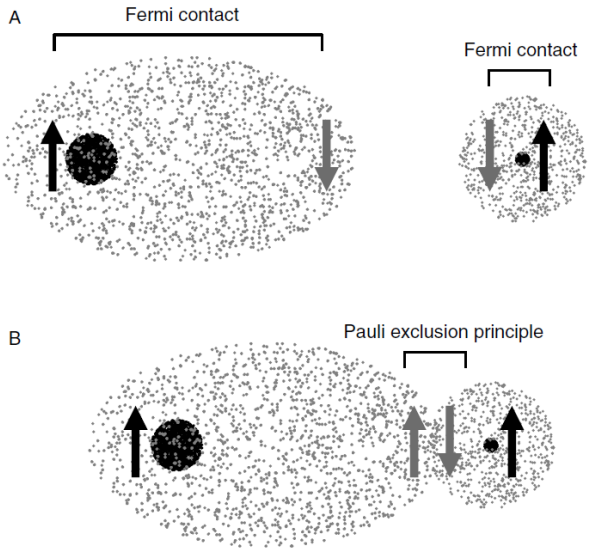

Fig 1 *Spin-spin interactions involved with scalar coupling. (A) In isolated atoms, the Fermi contact energetically favors an antiparallel orientation between nuclear and electronic spins. (B) In chemical bonds, the Pauli Exclusion Principle demands that the electron spins are in an antiparallel orientation thereby potentially forcing nuclear and electron spins in an energetically higher parallel orientation, depending on the nuclear spin state [14].*

As seen below on Fig 2, illustrating the 1,1,2 trichloromethane example, the H_a and H_b protons are spin-coupled to each other. Starting with the Ha signal, in addition to being shielded by nearby valence electrons, each of the H_a protons is also influenced by the small magnetic field generated by H_b next to it. The magnetic moment of H_b will be aligned with B0 in (slightly more than) half of the molecules in the sample, while in the remaining half of the molecules it will be opposed to B0.

The effective manetic field B 'felt' by H_a is a slightly weaker if H_b is aligned against B0, or slightly stronger if H_b is aligned with B0. In other words, in half of the molecules H_a is shielded by H_b (hence the NMR signal is shifted slightly upfield) and in the other half H_a is deshielded by H_b (and the NMR signal shifted slightly downfield). What would otherwise be a single H_a peak has been split into two sub-peaks (a doublet), one upfield and one downfield of the original signal.

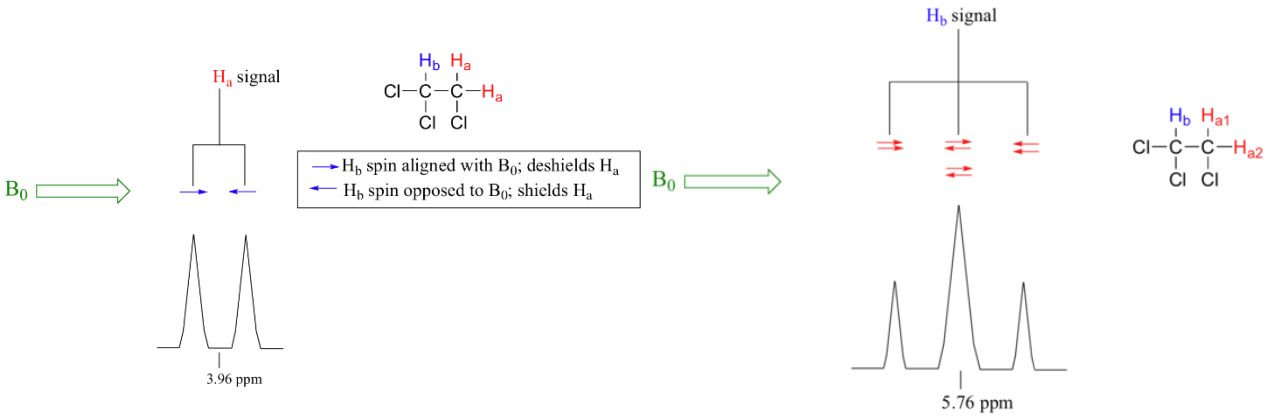

Fig 2 Spin Spin coupling in ,1,2-trichloroethane during 1H MR Spectroscopy [24].

Now let's focus on the H_b signal. The magnetic environment experienced by H_b is influenced by the fields of both neighboring H_a protons, which we will call H_{a1} and H_{a2}. There are four possibilities here, each of which is equally probable. First, the magnetic fields of both H_{a1} and H_{a2} could be aligned with B_0, which would deshield H_b, shifting its NMR signal slightly downfield. Second, both the H_{a1} and H_{a2} magnetic fields could be aligned opposed to B_0, which would shield H_b, shifting its resonance signal slightly upfield. Third and fourth, H_{a1} could be with B_0 and H_{a2} opposed, or H_{a1}opposed to B_0 and H_{a2} with B_0. In each of the last two cases, the shielding effect of one H_a proton would cancel the deshielding effect of the other, and the chemical shift of H_b would be unchanged.

2.5 B1 Inhomogeneity and Mapping B1 transmit fields

It is intuitive that B1 inhomogeneity is a major cause of artifacts in MR imaging modalities. B1 excitation fields are not uniform, particularly with surface coils, multi-coil geometries or high field systems, with one of the direct consequences being degraded SNR. [18].

The signal-to-noise performance of a coil can be improved by reducing the noise volume, which is made possible by placing the coil much closer to the object being imaged; this is one of the basic premises behind the use of surface coils. The reduction in noise volume generally comes at the price of an inhomogeneous B1 field, and hence non-uniformity in the image intensity. In high-field (3T) abdominal, cardiac, and neuro-imaging, *B*1 inhomogeneity on the order of 30–

50% has been predicted and observed [19][20]. This factor can be of extreme importance when considering the use of magnetic resonance spectroscopy.

Directly imaging the flip angle can be hard because there are unknowns such as receive sensitivity and proton density. There are several existing *B*1 mapping methods based on measurements at progressively increasing flip angles [21], stimulated echoes [22], or signal ratios [23]. Still, probably the most simple and straightforward of all these is the double-angle method, which involves acquiring images with two flip angles α and 2α, where TR *T*1 such that image signal is proportional to sin(α) and sin(2α), respectively. The *B*1 field is then derived from the ratio of signal magnitudes [8].

1.6.1 Double Angle (ratio method)

By acquiring two gradient echo images with flip angles α and 2α, with all other signal affecting sequence parameters kept constant, two different images are produced with signal intensity defined by:

$$M_{xy1} = M_0 \sin(\alpha)$$

$$M_{xy2} = M_0 \sin(2\alpha)$$

Taking the ratio removes the M0 dependence. Using sin (2α) = 2cos (α) sin (α),

$$\frac{M_{xy2}}{M_{xy1}} = \frac{2\cos(\alpha)\sin(\alpha)}{\sin(\alpha)}$$

$$\alpha = \cos^{-1}\left(\frac{M_{xy2}}{2\,M_{xy1}}\right)$$

One problem with the double angle method is that the longitudinal magnetization must recover nearly to equilibrium or there will be T1 weighting from the leftover longitudinal magnetization. A long repetition time is typically used with the double-angle methods to ensure that there is no *T*1 dependence in either M_{xy1} or M_{xy2} [9]. To circumvent this issue a magnetization reset sequence after each data acquisition can be applied (with the goal of putting the spin population in the same state regardless of whether α or 2α excitation was used)[8].

GE (Gradient Echo), an echo signal generated from free induction decay by means of a bipolar switched magnetic gradient. The echo is produced by reversing the direction of a magnetic field gradient or by applying balanced pulses of magnetic field gradient before and after a refocusing RF pulse so as to cancel out the position dependent phase shifts that have accumulated due to the gradient.

In the latter case, the gradient echo is generally adjusted to be coincident with the RF spin echo. When the RF and gradient echoes are not coincident, the time of the gradient echo is denoted echo time (TE) and the difference in time between the echoes is denoted time difference.

Gradient echo does not refocus the effects of main field inhomogeneity and therefore is generally used with a short echo time. Disadvantages of gradient echo imaging are compromised anatomic details and artifacts in regions with varying susceptibility e.g. between the air-containing sinuses and brain and especially between hemorrhages and normal tissue.

2.6 Alternative Nuclei

The simplest most widely used nucleus to be considered is the single proton, ^{1}H. Nevertheless, similar principles may be applied to imaging or spectroscopy using various other, more complicated, nuclei, such as Carbon (^{13}C), Phosphorous (^{31}P), Fluor (^{19}F) or Sodium (^{23}Na).

While the quantum mechanical behavior may be more complicated, the behavior of the net magnetic moment in these cases works in a similar fashion, where only the change in Larmor frequency (usually lower than for ^{1}H) needs to be considered. Whereas ^{1}H imaging typically gives the strongest signal (being the most sensitive and abundant nuclei in biological tissue due to the large proportion of water), other isotopes may provide more useful measurements for particular tissue types in certain applications, for either imaging or spectroscopy purposes.

2.6.1 Phosphorous 31

The successful use of proton MR spectroscopy in clinical settings is only matched by ^{31}P MRS [14]. Both its relatively high sensitivity (about 7% of protons') and a 100% natural abundance allow the acquisition of high-quality spectra without the need for long scanning sessions.

The chemical shift dispersion of the phosphates found in vivo is relatively large (around 30 ppm), which means an excellent spectral resolution even when using low (clinical) magnetic field strengths.

2.6.2 Identification of Resonances

Phosphorous NMR spectra from tissues in-vivo typically hold a limited number of resonances. The exact chemical shift position of almost all resonances is sensitive to physiological parameters like intracellular pH and ionic strength. By convention, the PCr (phosphocreatine) resonance is used as an internal chemical shift reference and has been assigned a chemical shift of 0.00 ppm (just as Tetramethylsilane, TMS, in conventional 1H MRS).

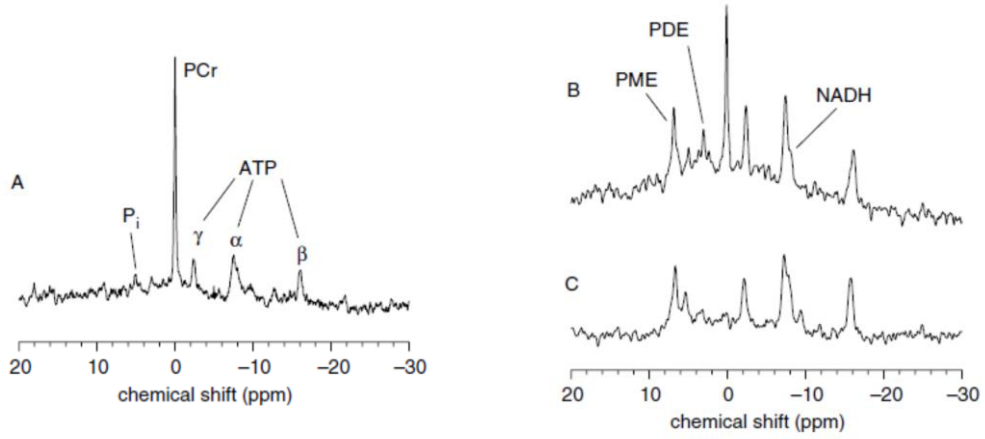

Fig 3 Typical localized in vivo ^{31}P NMR spectra from (A) rat skeletal muscle, (B) brain and (C) liver. Note the complete absence of PCr in the liver [14].

Probably the most important phosphorous based metabolite for gathering information on hepatic phospholipid metabolism is Adenosine Triphosphate. ATP consists of adenosine - composed of an adenine ring and a ribose sugar - and three phosphate groups (triphosphate). The phosphoryl groups, starting with the group closest to the ribose, are referred to as the alpha (α), beta (β), and gamma (γ) phosphates. ATP is highly soluble in water and is quite stable in solutions between pH 6.8–7.4, but is rapidly hydrolysed at extreme pH. At a pH of 7.2, the resonances of ATP appear at -7.52 ppm (α), -16.26 ppm (β) and -2.48 ppm (γ) [14]. Other phosphorous based metabolites are also very well documented.

Below, Table 1 below summarizes the most common metabolites found in ^{31}P MR spectra, as well as its correspondent chemical shifts (referenced relative to Phosphocreatine at 0.00ppm).

Metabolite		**Chemical Shift (ppm)**
Adenosine monophosphate (AMP)		6.33
Adenosine diphosphate (ADP)	α	-7.05
	β	-3.09
Adenosine triphosphate (ATP)	α	-7.52
	β	-16.26

	γ	-2.48
Dihydroxyacetone phosphate		7.56
Fructuose-6-phosphate		6.64
Glucose-1-phosphate		5.15
Glucose-6-phosphate		7.20
Glycerol-1-phosphate		7.02
Glycerol-3-phosphorylcoline		2.76
Glycerol-3-phosphorylcethanolamine		3.20
Phosphomonoester (PME)		6.90
Phosphodiester (PDE)		2.20
Inorganic Phosphate		5.02
Phosphocreatine		0.00
Phosphoenolpyruvate		2.06
Phosphorylcoline		5.88
Phosphorylethanolamine		6.78
Nicotinamide adenine dinucleotide (NADH)		-8.30

Table 1 Chemical shifts of biologically relevant 31P-containing metabolites in no specific order [4][14][42][43].

3. Animal Models of Liver Fibrosis

Animal models of hepatic fibrosis provide a means to study liver degradation and recovery, as seen in numerous studies [25][26][27] . For this to be possible, several approaches to induction of fibrosis have been described [28][29][30], out of which CCl4 (or Carbon tetrachloride) intoxication in rats and mice is probably the most widely studied. In addition, the CCl4 model is the best characterized with respect to histological, biochemical, cell and molecular changes associated with the development of fibrosis [31].

CCl4 can be given IP (Intra Peritoneal) or by oral gavage and it induces zone III necrosis and hepatocyte apoptosis with associated hepatic stellate cell activation and tissue fibrosis [28]. With repetitive dosing, CCl4 can be used to induce bridging hepatic fibrosis (4 weeks of 2 x weekly dosing), cirrhosis (8 weeks of 2 x weekly dosing) and advanced micro-nodular cirrhosis (12 weeks of 2 x weekly dosing). In addition, for each of these models spontaneous recovery from fibrosis can be studied after cessation of dosing [31].

Animal models are essential to the investigation of liver fibrosis and other fibrotic diseases because they provide the only model in which the serial sampling of tissue can be made which facilitate the dissection of the cell and molecular processes that underlie fibrosis. Still, the importance of studying human models of disease cannot be stressed enough. Nevertheless, at best they can only provide a momentary snapshot of a disease process which may develop over weeks or months. In addition, the morbidity, potential mortality and ethical issues associated with liver biopsy in humans, significantly limits the use of biopsy material for research. It's ethically impossible to manipulate the pathogenic process of liver fibrosis experimentally and in vivo in human beings. For all these reasons, animal models of liver fibrosis remain a vital experimental instrument. Many experimental models of hepatic fibrosis have been described, including those associated with toxic damage [28], immunological damage [32], biliary fibrosis [33], and alcoholic liver disease [34].

In a simple way, carbon tetrachloride is a halokane activated by oxidases to yield a trichloromethyl radical, which initiates lipid peroxidation (a process of degradation) and can react with the sulphydrol group of proteins [31]. CCl4 has been administered to rodents by inhalation, gastric gavage and by subcutaneous and intraperitoneal injections [28]. Because of the necessity for bioactivation, the severity of CCl4 injury will be strongly influenced by the type of diet and the presence of other xenobiotics. Consequently, specific diet or drugs can enhance CCl4 toxicity and the speed of development of fibrosis.

Carbon tetrachloride induced fibrosis and cirrhosis is one of the oldest and is probably the most widely used toxin-based experimental model for the induction of fibrosis. It has the advantages that it has been clearly characterized and, in many respects, mirrors the pattern of disease seen in human fibrosis and cirrhosis associated with toxic damage [31]. In addition, there is extensive experience with this model with respect to the characterization of histological, biochemical changes and changes associated with injury, inflammation and fibrosis [28][31]. Finally, in experienced hands, even using outbred rats or mice, this model elicits a reproducible and predictable fibrotic response, making it a valuable basis for study. For these reasons, there is a fairly extensive experience and growing literature in which CCl4 induced fibrosis is used as a basis for mechanistic study.

The CCl4 model also has disadvantages. In comparison, as a model, while mimicking the before mentioned disease pattern it has no direct human disease equivalent. Additionally, unlike human liver fibrosis, there is more pronounced cholangiolar cell hyperplasia in advanced CCl4 fibrosis and in rats in the presence of CCl4 induced cirrhosis there is failure to progress to the development of hepatocellular carcinoma [35][36].

Some groups at the University of Edinburgh have previously used CCl4 in a series of experimental models of liver injury and fibrosis. These include using CCl4: To induce acute injury characterized by self-limiting hepatic stellate cell activation and hepatocellular regeneration; to develop early and established fibrosis (4 to 6 weeks of CCl4), to develop early reversible cirrhosis (8 weeks of CCl4 intoxication) and to develop cirrhosis that demonstrates only partial reversibility (12 weeks CCl4 intoxication) [37][38][39][40].

3.1 In-Vivo Study

For this study, 2 groups of rats were used (control and disease model), all of the Sprague Dawley stock, like the one on Fig 4 . The Sprague Dawley rat is an outbred (bred from distantly related or unrelated individuals, often producing a hybrid of considered superior quality) multipurpose breed of albino rat used extensively in medical research [4][5][31][38]. Its main advantage is its calmness and ease of handling. This breed of rat was first produced by the Sprague Dawley farms (later to become the Sprague Dawley Animal Company) in Madison, Wisconsin in 1925. The average litter size of the Sprague Dawley rat is 11. Each group (control and disesase model) consisted of 2 rats (meaning 4 in total).

Fig 4 A typical Sprague-Dawley albino laboratory rat [41]

Our disease model group was subjected to 8 weeks of twice-weekly intraperitoneal CCl4 which usually induces advanced liver fibrosis or early cirrhosis.

Phosphorous MRS offers a non-invasive technique for studying metabolic processes in the liver. There are mainly six resonances of interest in in vivo liver spectroscopy, namely phosphomonoesters (PME), inorganic phosphate (Pi), phosphodiesters (PDE), and adenosinetriphosphate (alpha, beta, gamma ATP). Resonances from PME and PDE are thought to reflect the cell turnover of the hepatocytes whereas the alpha, beta and gamma groups of ATP reflect the energy state in the cells [42].

In a typical ^{31}P MR spectrum from normal liver tissue low concentrations of PMEs and high concentrations of PDEs have been observed, whereas in fibrotic/necrotic/tumorous tissue elevated levels of PMEs and decreased levels of PDEs have been shown [4][43]. A ratio between these two metabolites has been suggested as a natural biomarker for these conditions, and as such it's going to be one of the focus of the analysis later on.

Other studies [4][7], involving partial hepatectomies, advocate changes in the Inorganic Phosphate/ATP ratios, suggesting an increasing consumption of ATP while the liver tries to compensate by adjusting the liver function. While not directly comparable, it's still worth mentioning.

4. MR Setup

The MRI instrument has evolved into one of the most complex and expensive devices used in imaging practice. Advances in the instrumentation have been the single most important factor in the progress of clinical MRI. This progress can be seen in every hardware field, from advances in magnetic field strength or gradient coil technology, to RF electronics and computer systems.

In principle, the component requirements for an MRI instrument are quite simple. The hardware comprises a magnet to generate a static magnetic field, gradient coils for spatial encoding, RF electronics for irradiation and reception, and computers for data processing and manipulation.

4.1 The MRI apparatus

According to the manufacturer Agilent, the 7T animal MRI system is a flexible and adaptable magnetic resonance imaging scanner for pre-clinical imaging and research. The system has an intuitive user interface (vNMRj), and a flexible programming environment which can carry out a wide range of pre-clinical imaging functions. It was designed with preclinical use in mind.

The high magnetic field provides structural and functional images with higher resolution in comparison with clinical MRI. It is recommended for abdominal, cardiovascular, muscular and articular use, as well as dynamic molecular imaging.

4.2 Magnet and Gradient

The magnetic resonance effect requires the application of a strong homogeneous static magnetic field, which, nowadays, is usually achieved with the use of a superconducting magnet, cooled to cryogenic temperatures during operation. In its superconducting state the wire can conduct much larger electric currents than ordinary wire, creating intense magnetic fields, in our case 7 Tesla.

The gradient used during all experiments was Varian's 205_12_HD. It is described by the manufacturer as a fully self-shielded gradient system designed to suit ≥ 210mm room temperature bore superconducting magnets and gradient systems. The design incorporates fully optimized X, Y and Z coil configurations. The X and Y coils are made from copper plates. The Z coil is wound from heavy duty copper strip. The gradient has been optimized to allow for high duty cycle experiments while the room temperature shim set has been specially designed to minimize coupling between gradients and shims during pulsing. Finally, the gradient set is fully vacuum impregnated to minimize mechanical vibration and noise.

4.3 RF Coil

Radiofrequency (RF) coils are an essential component of what makes up a

complete NMR system. While the magnet creates the spin population difference and therefore the longitudinal magnetization, it is the transverse magnetic field oscillating in the RF range that rotates the longitudinal magnetization into the transverse plane, where it can be detected as an induced signal by a receiver coil. The many different possibilities for RF coil design can partially be explained by the fact that each coil is often a compromise between its desirable and undesirable features, with a general single coil optimal for all applications being no more than a distant utopia. While a volume coil provides a homogeneous B1 magnetic field, such that spin excitation is uniform across the sample, its large size and often poor filling factor compromises their sensitivity. On the other hand, surface coils are very sensitive due to their high filling factor and their optimal size relative to the subject under investigation. However, surface coils have their downsides, in that the generated B1 field is extremely inhomogeneous which will lead to signal loss when an RF pulse is transmitted. Surface coils become advantageous for MR when sample losses are dominant and/or the region of interest is quite close to the surface. A small surface coil will be superior to a well optimized birdcage type-coil when used for features within a few millimeters of the surface. At greater depths, the small birdcage has higher SNR in addition to its strong advantage in RF homogeneity. Here, *coil* (not sample) losses are dominant for both the surface coil and the birdcage, but the surface coil achieves higher SNR over a small region near the surface because of its higher filling factor. The specific coil used in this project is of the $^{1}H/^{31}P$ transmitter/receiver surface coil variety.

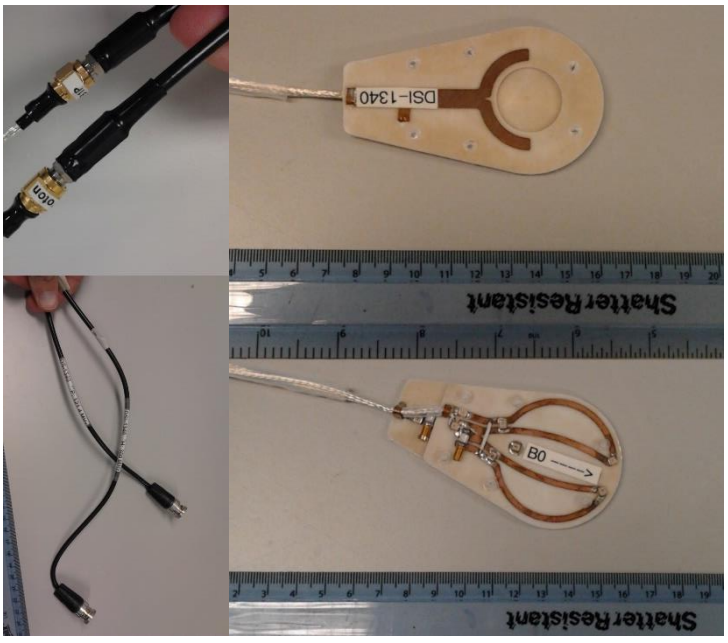

Fig 5 Doty Scientific Doty30

Throughout this study, the coil used was a Doty Scientific *Doty30*, a 30mm diameter $^{1}H/^{31}P$ Double-tuned loop/butterfly surface coil for 7T (Tuned to 1H at 300 MHz, ^{31}P at 122 MHz).

A pair of back-to-back D coils (also called a butterfly coil) can be used to generate an RF magnetic field just below their surface that is orthogonal to that of the loop surface coil and, for proper orientation of the D coils, is also orthogonal to B0 [19, 31]. Hence, the combination of the loop and pair of D coils, as shown in Fig 5, can be used for circular polarization, which may improve SNR [43]. The loop/D combination is also often used for double resonance (e.g., $^{1}H/^{31}P$, or $^{1}H/^{19}F$). In many cases, it permits higher S/N at both frequencies than the alternative of double-tuning a single loop. Alongside the combined $^{1}H/^{31}P$

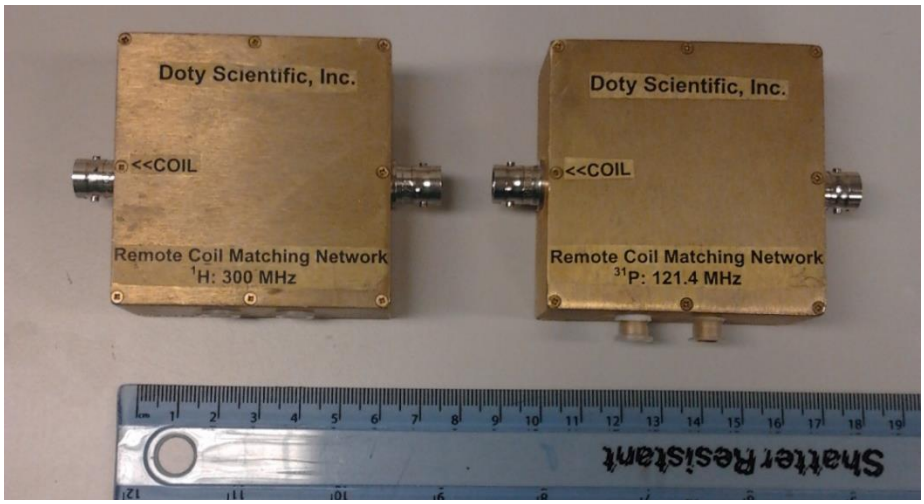

Fig 6 Remote Coil Matching Units, for both Proton and Phosphorous, from left to right. These units were used to manually adjust both matching and tuning on each coil, without the need to access it directly.

surface coil, two remote coil matching networks were used, one for each channel. These boxes allow for remote impedance matching and limited (2%) frequency tuning of the respective surface coils.

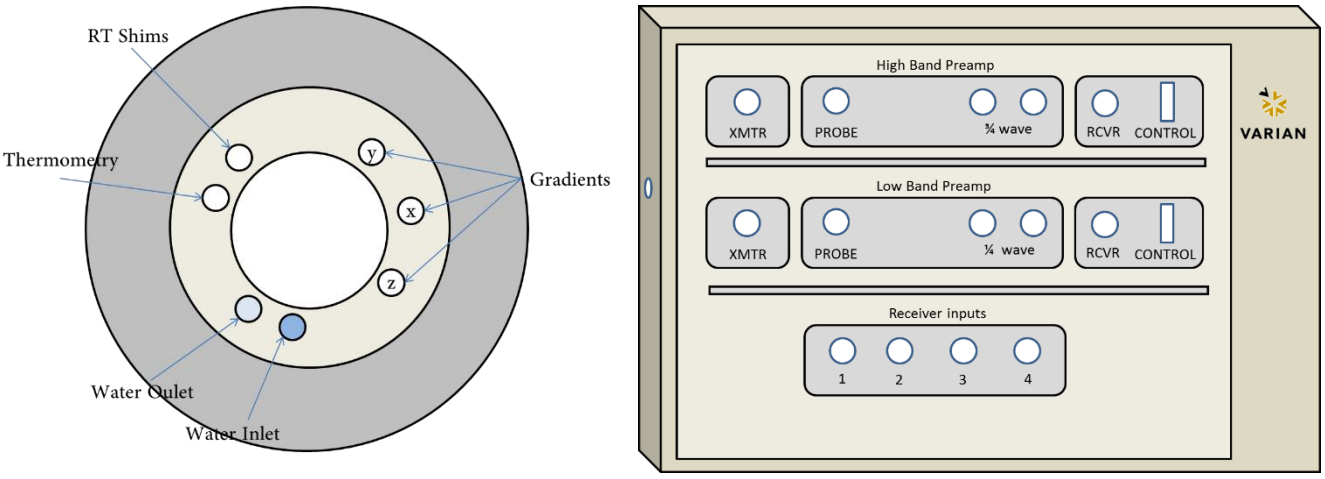

Fig 7 Rearside view of the magnet hole and a schematic of Varian's High Band RF pre amplifier.

4.3.1 Tuning and Matching

In order to be effective for both imaging and spectroscopy, the RF coil must be tuned to resonate at the Larmor frequency f0 of the nucleus to be detected (which in turn will depend on the magnetic field strength [44]). This is usually achieved by adding capacitive or inductive elements across or along the coil structure. Also of great significance is the interface between the coil and the RF hardware of the MRI machine. In order to further minimize losses, optimize power transfer to the coil and suppress reflected signals which may degrade the acquired image or spectra, it is necessary that the impedance of the RF power amplifier, the receiver preamplifier, the cable connecting the coil, and the load presented at the end of the cable are all matched. This tuning and matching is done on a case by case basis, as it depends on the size, shape and composition of the subject being scanned. Connected to the MRI Preamplifier is a tune interface, which can be

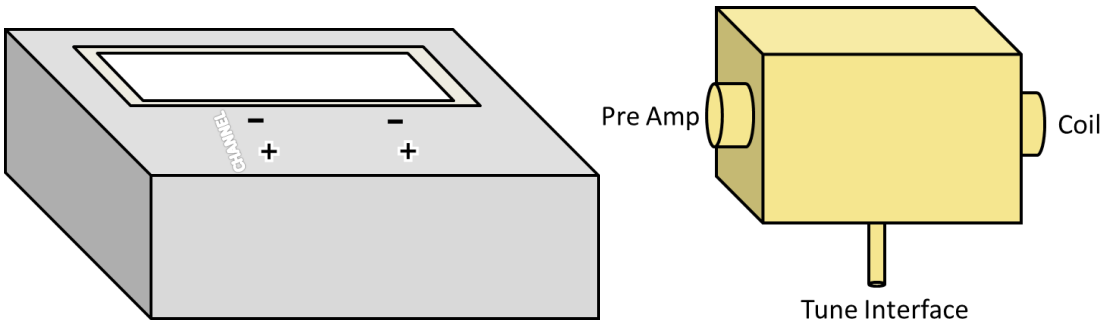

Fig 8 Tune Interface Box and Re-Routing Unit representations, from left to right. The Tune Interface Box was used to check the tuning for each nuclei, the lower the value on the display, the better. The Re-Routing Unit was used to link the coil to the Preamplifier while connecting it to the Tuner.

used by means of re-routing the cables that connect the RF Coil to the pre amplifier (*Fig 7*). This is done using the small apparatus depicted in *Fig 8*.

After the cables are re-routed, the user can tune the coil through the remote coil matching networks (one for each channel). Now, there two approaches as to how the user can monitor if matching/tuning is improving while it's being adjusted. One way to do it relies on the tune interface, which displays a specific value for each channel. The idea is to get this value as low as possible. Another method relies on the software's built-in Probe Tuning mechanism (accessed by typing *mtune* in vNMRj's command window).

When the probe is properly tuned and matched, the tune signal is collinear with the vertical green line and its tip is as close to the baseline (horizontal axis) as possible. Either way, this process had to be done for both the 1H and 31P channels , as both act individually and have different characteristics altogether.

4.4 In Vivo specific hardware

As stated before, this study includes MR scanning sessions done both with phantoms and In-Vivo subjects, and while the basic setup is mostly the same in these two cases, the are some small additions to the hardware department in the In-Vivo case. With the inclusion of a living subject a lot more variables come into play, such as temperature, anesthesia delivery, heart/respiratory rate, as well as the respective gating, meaning the experimental setup is not as straightforward as the one typically used for phantoms.

Animal physiologic monitoring and gating control is provided through a SA Instruments Inc. (SAII) Model 1025 MR-compatible monitoring and gating system. The system can simultaneously monitor and record ECG, respiration, temperature, and blood pressure, depending on the desired parameters and sequences being used.

Fig 9 *SA Instruments Inc. (SAII) Model 1025 MR-compatible monitoring and gating system.*

According to its manufacturer, this system was designed specifically to meet the physiological monitoring and gating needs for anesthetized mice, rats and larger animals in the MR environment. It consists of an ERT Module located near the animal and an ERT Control/Gating Module connected to a PC located near the operator console. The PC displays multiple waveforms, measured values, trends and gating pulses. The ERT Module measures ECG using three leads with needle or surface electrodes, respiratory rate from a small pneumatic pillow sensor and/or from the movement of one ECG lead and temperature with a small rectal thermister probe. Power is supplied by an external, rechargeable battery. The ERT Control/Gating Module receives data from the ERT Module and any of several optional acquisition modules. The ERT Control/Gating Module sends data to the PC for display and receives user instructions from the PC to control measurement and gating functions. Gates from ECG, respiration and any of the available options are generated by the ERT Control/Gating Module

microprocessor and sent to the MR system. The delay from the R-wave peak to the MR system gate is user selectable as is the expiration gate delay and width.

To achieve good results during in-vivo experiments, be it structural, spectroscopic or some other modality, it is absolutely necessary for the animal to be as still as possible inside the scanner. For this to happen, the subject (in this specific case, a rat) is put in a special structure (to put it more precisely, an MR compatible animal holder) and kept under anesthesia.

Regarding the animal holder, a standard RAPID biomedical animal holder was used. RAPID Biomedical offers a variety of animal holders for MRI on both mice and rats. All holders are equipped with nose cones and anesthesia gas delivery. The standard RAPID Animal Holder is also equipped with integrated stereotactic head fixation system, indispensable for things such as high resolution brain imaging. The holders have a length of 870 mm and are prepared to fit standard Tx coils.

The MRI anesthetic apparatus used throughout this study was the Pneupac880. As described by the manufacturer, it comprises a compact, mobile unit specifically designed to be compatible within strong magnetic fields, such as the ones present in a MRI suite, suitable for use in cases of difficult access to the subject (it is designed to work within one meter of the ISO center of the magnet). As a matter of curiosity, this specific device has CE Mark (MDD, Medical Devices Directive) clearance but is has not been approved by the FDA, meaning that it can't be sold or used in the USA.

Another part of the experimental In-Vivo setup is the heater/fan modules. According to the manufacturer's brochure, the SA Instruments, Inc. MR-compatible, small rodent Heater System controls the temperature of small animals undergoing imaging procedures. As referenced above, animal temperature is measured with either a MR-compatible thermister probe. Dedicated software continuously processes the temperature measurements and sends an optical control signal to the Heater Module. This way, the rate of change of temperature is monitored and heater control is adjusted to minimize overshoot and generate a closed loop control system. Mouse temperature variations of less than 0.1°C can typically be obtained during MR examination, providing a great degree of control. This is a very important factor, as the subject's heart rate is dependent on its body temperature [47].

All laboratory work was executed while wearing clean gown and shoes, as well as a disposable mask, mob cap and gloves when required.

5. MR Spectroscopy Sequences

Data acquisition is essentially the be-all and end-all part of the process. Without a good acquired dataset it is impossible to do a reliable analysis and subsequent investigation. Choosing the correct pulse sequence and its parameters is no easy task, as the possible combinations are as numerous as they are complex. There are plenty of factors that come in to play, each with its own advantages and disadvantages, making the process of optimization often difficult and time consuming.

In a very broad general sense there are two fundamentally distinct ways one can approach this subject: localized spectroscopy and non-localized spectroscopy, both with its advantages and disadvantages. Pulse sequence names (and occasionally even specific characteristics) tend to vary between different NMR manufacturer brands, which may cause some confusion to people used to one specific brand and its set of sequences. Keeping in mind that the whole study went down in a Varian/Agilent environment, I'll continue by detailing all pulse sequences considered during the course of this study.

In regards to the Non-Localized Spectroscopy side of things, the very simple SPULS (single pulse and 1D acquire) sequence was put into consideration. Later on this sequence was slightly modified and evolved into a custom made sequence labeled SATSP (SATurated Single Pulse) to fit a saturation pulse prior to excitation, as it will be discussed shortly.

A description of each pulse sequence along with its characteristics follows.

5.1 Image Selected In Vivo Spectroscopy (ISIS)

ISIS is a localization technique that achieves full 3D localization in eight scans, and its basic sequence structure is as shown below in Fig 10.

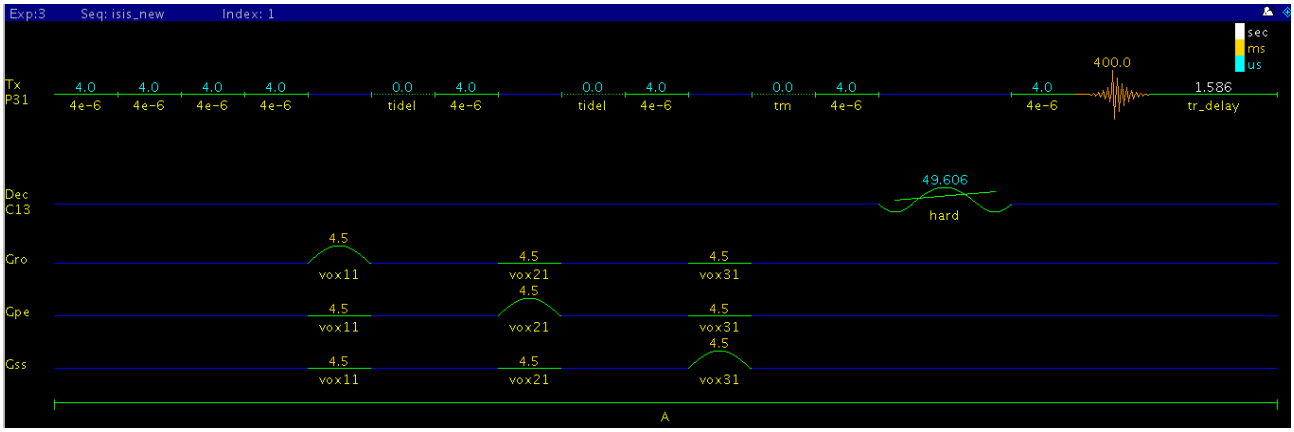

Fig 10 ISIS pulse program, as seen in vNMRj

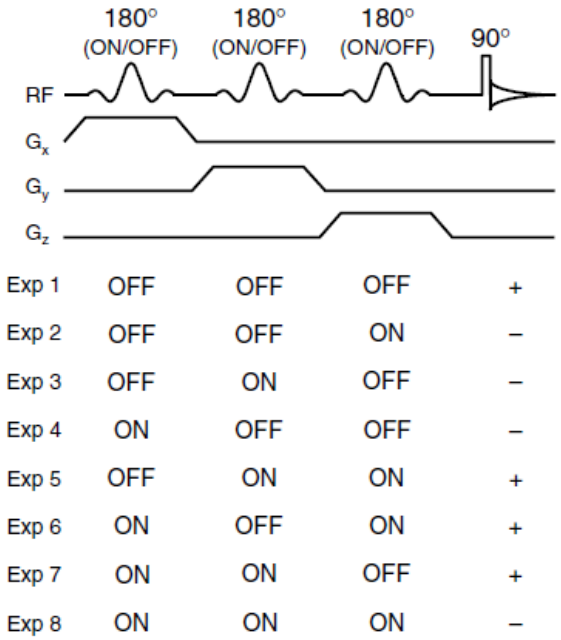

Fig 11 Pulse sequence for ISIS localization. For 1D ISIS localization, two experiments are required, one with and one without a spatially selective inversion pulse prior to excitation. Subtraction of the two datasets will only give signal from the localized volume. For 3D localization, eight experiments (2 × 2 × 2) are required as shown, whereby the right column indicates the relative receiver phase (+ = 0◦, − = 180°) [14]

ISIS uses three frequency-selective inversion pulses in the presence of three orthogonal magnetic field gradients.

These inversion pulses are turned on and off according to an encoding scheme depicted in the above figure. When zero or an even number of 180° pulses are executed, the desired magnetization of the cross-section of the three selected slices ends up along the positive longitudinal axis and following a 90° -x excitation pulse will end up along the positive y axis. During a scan with an odd number of 180° pulses, the desired magnetization ends up along the negative longitudinal axis an is excited to the negative y axis by a 90° -x pulse. Adding and subtracting the individual stored scans with even and odd number of 180° pulses, respectively, will constructively accumulate signal from the desired location while destructively cancelling signal from all other locations, as shown in

Fig 12. In each scan, signal from the entire sample is excited, and the ISIS inversion pulses change the phase of the excited signal. In this case, the scan with two 180° magnetic pulses, the magnetization in the cross section experiences a double inversion and therefore ends up with a positive phase. Then, the localized volume is obtained by subtracting images B and C from images A and D (meaning, final image (F) is obtained by F=A-B-C+D).

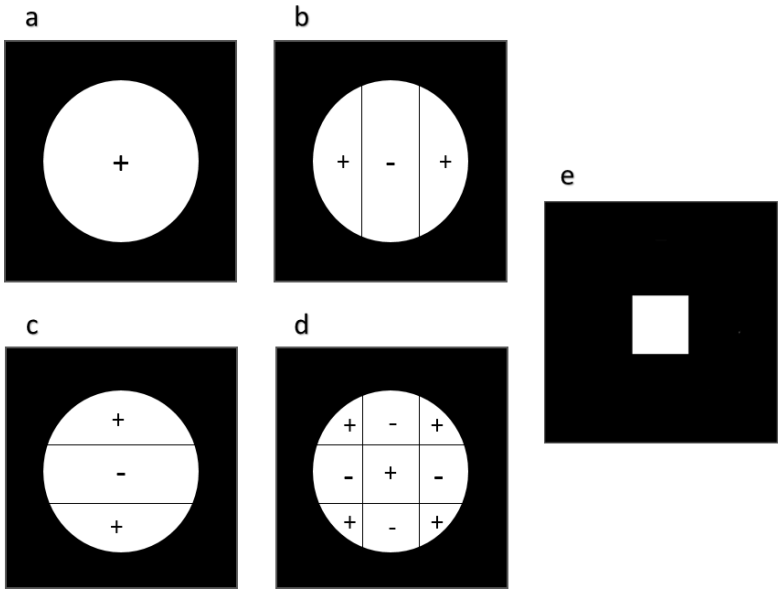

Fig 12 Experimental evaluation of 2D ISIS localization by MRI. (A) Image representation of a water-filled sphere. No spatially selective (in-plane) inversion pulses were executed. (B and C) Images (in absolute value) in which one spatially selective inversion pulse has been executed. The + and− signs correspond to noninverted and inverted areas, respectively. (D) Image of the sphere after the execution of two spatially orthogonal selective inversion pulses. Due to the double inversion in the middle of the sphere, the magnetization resides along the positive longitudinal axis. (E) The localized volume is obtained according to the following add–subtract scheme : (E) = (A) − (B) − (C) + (D).

Because of the way it is sequenced, ISIS leads to the possibility of using very short TE times [14], which greatly benefits the identification of short T2 species (such as ATP with 31P MRS).

The practice of Outer Volume Supression (OVS) is consistently used in combination with the ISIS sequence, giving birth to (Connelly et al [15]) a new sequence named OSIRIS (outer volume suppressed image related in vivo spectroscopy). The frequency domain excitation profile of a noise pulse consists of a selective null band in which magnetization is not perturbed outside this null band. This combination leads to a significant suppression of magnetization outside the VOI, such that the receiver gain and motion problems are minimized. Even though noise pulses are most commonly used for this effect [15], any kind of OVS can be used [14].

Even so, ISIS comes with problems of its own. In vivo MR Spectroscopy scans (and particularly in 31P spectroscopy even more so) are often executed using surface coils for increased sensitivity, but that comes with a cost. B1 magnetic field inhomogeneity can degrade the performance (slice profile) of the inversion and excitation pulses, leading to greatly reduced sensitivity (complete opposite to the initial intention of using surface coils), and increased contamination from unwanted signals [45].

5.2 Single Pulse and 1D acquire (SPULS)

Regarding non-localized spectroscopy, SPULS is probably one of the simplest methods one can use. Although it's almost exclusively recommended by Agilent as a test sequence to check the NMR signal during calibration [46] (possibly because of its reduced flexibility in tinkering with parameters), its speed and high SNR are rather positive aspects to be considered.

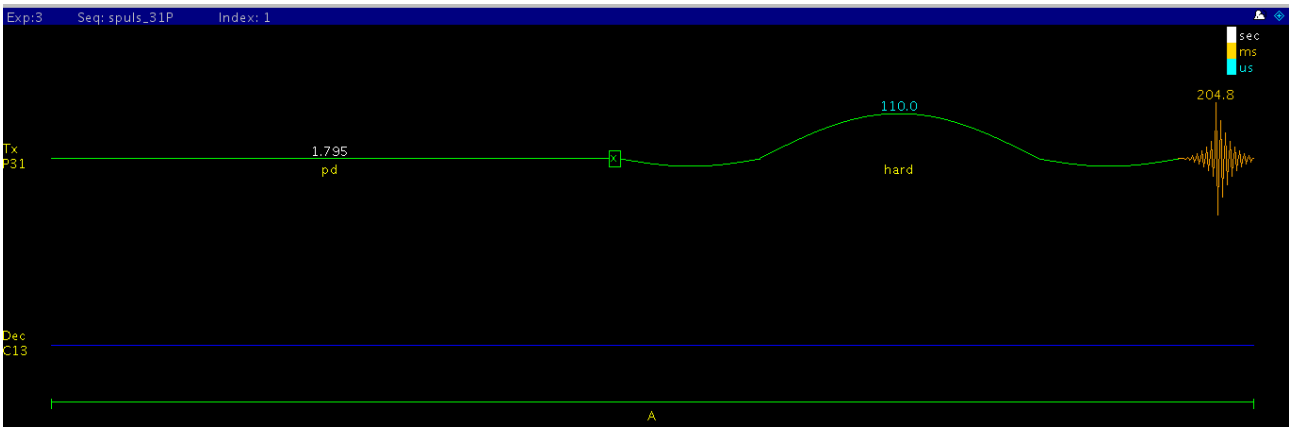

Fig 13 SPULS pulse program, as seen in vNMRj

Measurement of regular 1D NMR experiment is extremely simple and usually carried out in three stages: The sample/subject reaches equilibrium; An rf signal of sufficient power is transmitted and for a sufficient period of time (only a few microseconds, as localization is not needed), in order to move the magnetization vector from the z-axis to the x,y-plane (a pulse of up to 90°).

The signal that evolves due to precession of the magnetization vector is measured after the pulse and at the end of the process, the vector returns to equilibrium on the z-axis (process known as FID).

Possibly the biggest problem one comes across when using the SPULS sequence aimed at actually gathering valuable spectroscopy information in an in vivo setting is the intrinsic inhomogeneity in living structures. Due to the lack of localization, all acquired information is referent to the sample/body as a whole, with no information whatsoever on where the signal is coming from.

Without the use of localization, scan speed times increase and signal loss becomes minimal, meaning an improvement for SNR. Still, as of now this technique is apparently useless for this matter, since without localization there's no way of knowing where the signal originates from, and the observed sample/subject is not a homogenous structure. Luckily, this problem can be circumvented using OVS. By saturating the unwanted structures (skin, muscle, fat) prior to the actual SPULS sequence, signal from outside our region of interest can be theoretically avoided, with the remaining signal coming from the desired structure.

Alas, use of outer volume suppression with this sequence is not supported out of the box, meaning it had to be hard coded into a new sequence (SATSP), compiled and only then it is ready to run.

Each new modification in the desired parameters, albeit small, requires the user to go back and forth different sequence layouts, namely SPULS and PRESS, in order to access all parameters that need changing. In retrospective, it would have been wiser to build a proper GUI for this specific sequence, which would streamline the process, making it faster and easier to use.

5.3 Saturated Single Pulse (SATSP)

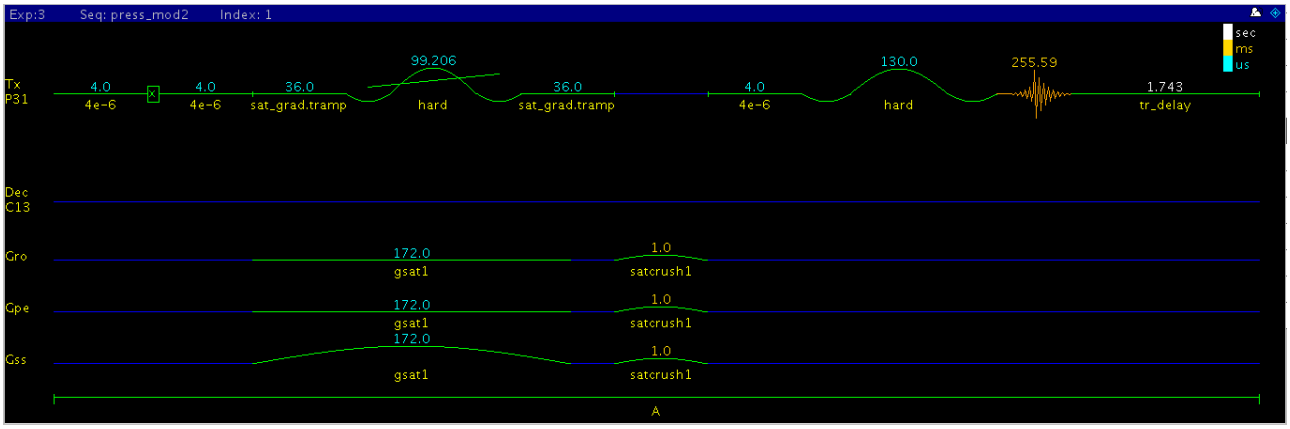

Fig 14 SATSP pulse program, as seen in vNMRj

Essentially, this sequence consists on the SPULS sequence program preceded by a saturation pulse, of whatever nature we may choose. The basic idea is to saturate the unwanted region prior to the excitation pulse and acquisition, so that we only acquire signal coming from the non-saturated region, ie. our region of interest. The main advantage would be the simplicity and fast acquisition times. As a main disadvantage, this sequence only provides 1D localization.

This sequence was achieved by combining existent Varian code used in both SPULS (for the excitation pulse) and PRESS (for the saturation pulses) pulse sequences, with some modifications. The complete pulse sequence code can be found at the end of this dissertation, with the code properly commented and described.

5.4 Chemical Shift Imaging (CSI)

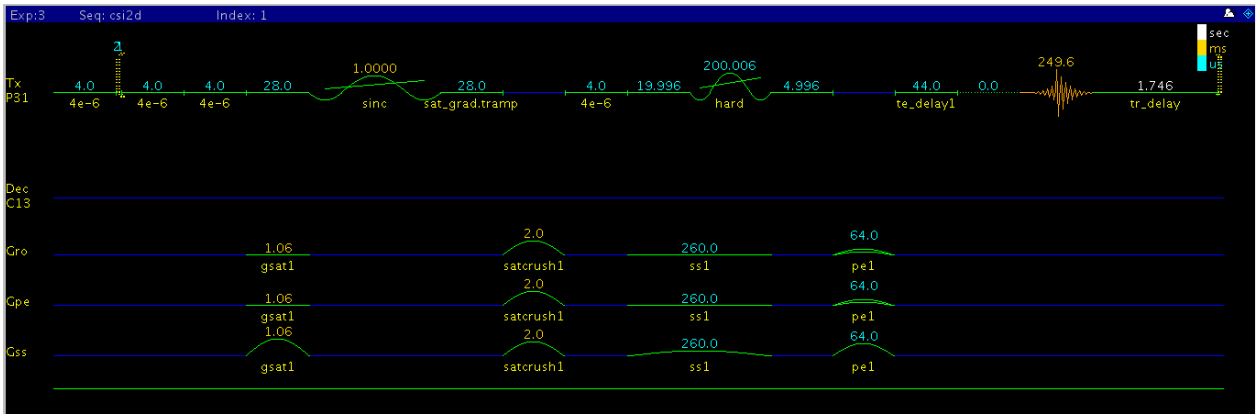

Fig 15 CSI pulse program, as seen in vNMRj

Also referred to as Metabolic Imaging, CSI consists in recording the spectroscopic data for a group of voxels, in slice(s) (2D) or by volume (3D). It is based on a repetition of PRESS type sequences to which is added spatial phase encoding. The number and direction of phase encodings depend on the number of dimensions explored (be it 1D, 2D or 3D), adding on to acquisition time. Signal processing calls on Fourier transforms (1 for each phase-encoded dimension phase + 1 for spectral analysis) and requires data correction (correction of the baseline, phase, etc).

The results appear in the form of parametric images (metabolic maps) or a matrix of the spectra of the regions to be studied.

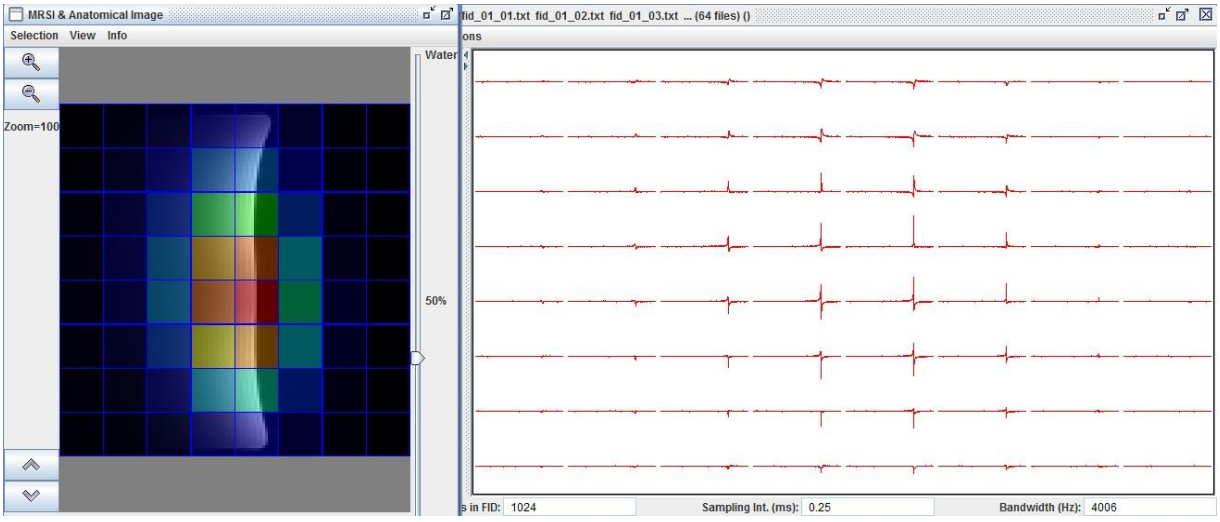

Fig 16 CSI map and relative anatomical representation. Each voxel represented on the figure (PPA phantom SCOUT acquired image) on the left has a correspondent spectrum on the right, creating a metabolic matrix.

The PRESS localization method [14] is a so-called double spin-echo method, in which slice-selective excitation is combined with two slice-selective refocusing pulses. When the first 180° pulse is executed after a time t1 following the

excitation pulse, a spin-echo is formed at time 2t1. The second 180◦ pulse refocuses this spin-echo during a delay 2t2, such that the final spin-echo is formed at time 2T1 + 2T2 (which equals the echo-time of PRESS, i.e. TE = 2T1 + 2T2). The first echo contains signal from a column which is the intersection between the two orthogonal slices selected by the 90◦ pulse and the first 180◦ pulse. The second spin-echo only contains signal from the intersection of the three planes selected by the three pulses resulting in the desired volume. Signal outside the VOI is either not excited or not refocused, leading to rapid dephasing of signal by the 'TE crusher' magnetic field gradients.

5.5 Gradient Echo (GEMS)

GEMS (Gradient Echo Multi Slice), the gradient echo sequence illustrated in Fig 17 operates in a similar way to the spin echo sequence, although uses bipolar gradients rather than an inversion pulse to achieve refocussing and echo generation [48]. Generally, smaller flip angles (for example, 30°) are used than in a spin echo sequence; this means that less signal will be available for image generation, but allows residual z magnetization to be consumed in subsequent excitations – thereby allowing sorter repetition times and faster image acquisition. Although z magnetization does not fully recover due to the short repetition time, equilibrium is established after the first few excitations. Gradient echo imaging generally allows faster acquisition with lower SAR than spin echo sequences, albeit somewhat more vulnerable to certain artifacts (including those due to field inhomogeneities). Variations on the sequence allow improvements in terms of signal strength, artifact reduction, imaging time and measurement of flow.

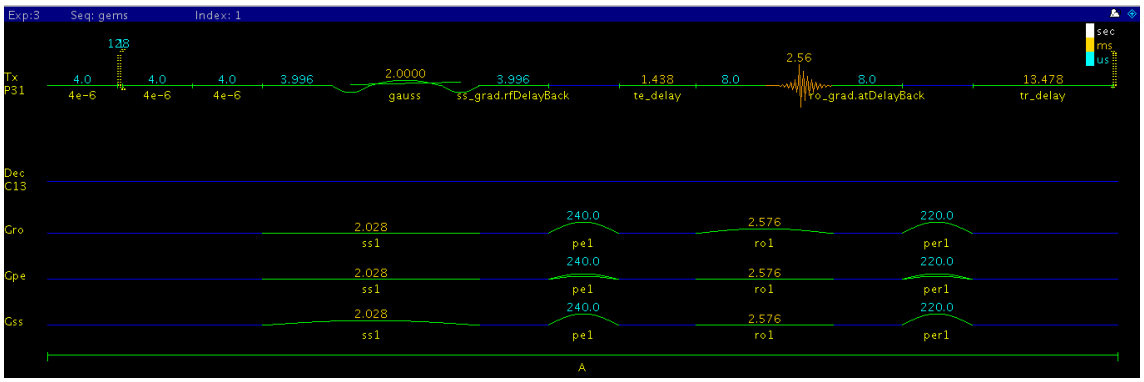

Fig 17 GEMS pulse program, as seen in vNMRj

GEMS is a default pulse sequence present in Varian scanners that uses a changeable flip angle instead of a 90° pulse and a gradient instead of a RF pulse to rephase the FID. T2*, T1 weighted and proton density images can also be acquired using this specific sequence. The flip angle in combination with the TR determines the T1 weighting and the TE controls the amount of dephasing.

6. Experimental Protocols

Several Experimental protocols, each for a specific purpose, were followed throughout the course of this study. Here you can find protocols for both phantom and in vivo use that more or less acted as guidelines for each experiment. The required preparation and handling of every animal used during this study was performed by an experienced member of the Edinburgh Preclinical Imaging Centre, diligently following every normative guideline.

6.1 Phantom Protocol

1) Starting with positioning, the combined Doty 1H/31P coil should be centered relative to the phantom (if the Liver Phantom is being used, the small compartment should face the surface coil). It should be ensured that the phantom is leakproof so that no damage may occur to both the coil and the machine.

2) Perform coil tuning and matching. Register values for future reference.

3) SCOUT images should be acquired to verify the correct position of the phantom. If the correct position is not achieved at first, adjust it accordingly, repeat SCOUT image acquisition and coil tuning/matching if necessary until the desired position is achieved.

4) Proceed to 1H power calibration and register the values for further reference.

5) When using the Liver Phantom, acquire SCOUT images with progressively higher flip angles. Obtained images where the second compartment appears brighter mean that a 90 degree flip angle (or close to it) is most likely affecting that area. Register those values.

6) In order to achieve the best possible shimming, a few different methods can be applied:

   a) Automated Shimming

      i) Global shim techniques, such as quickshim can be used. While using the Liver phantom, it should be very important to choose a FA value that works in our favour, with more signal coming from our region of interest.

      ii) Localized shim techniques, such as ge3d, can also be used. Shim gradient values will be chosen in accordance to the user defined voxel.

   b) Manual Shimming

      i) Global shimming can be done by loading a regular SPULS sequence. Again, carefully choosing a favorable FA is vital to achieve a good result. Signal should

be, as much as possible, coming from our area of interest, and not any surrounding areas.

ii) Localized shimming can be done by loading a PRESS sequence, selecting a voxel of interest and varying the shim gradient values until the desired result is achieved.

7) Using the Liver Phantom, 31P power calibration should be done in accordance to the Phenylphosphonic Acid peak, originating from the second compartment, further away from the coil. For single compound/peak phantoms, power calibration is straightforward, as only that peak can be considered. Register values for further reference.

8) The phantom is now ready to be scanned. Choose the adequate sequences and parameters that fit your purpose in the experiment.

6.2 In Vivo Protocol

1) Animal must be anesthetized before being put in the scanner. A rectal thermometer is used to check the subject's temperature and a surface electrode placed directly below the subject's chest to monitor the heart rate.

2) Concerning positioning, the animal is placed on the animal holder and the combined Doty 1H/31P coil should be centered relative to the liver of the animal. Tape can be used to maintain it still and minimize the effects of respiratory movements.

3) After the subject is Coil tuning and matching.

4) SCOUT images should be acquired to verify the correct position of the subject. If the correct position is not achieved at first, adjust the subject accordingly, repeat SCOUT image acquisition and coil tuning/matching if necessary.

5) 1H power calibration.

6) SCOUT images with progressively higher flip angles should be acquired. Obtained images where the liver is brighter mean that a 90 degree flip angle is most likely affecting that area.

7) In order to achieve the best possible shimming, a few different methods can be applied:

    a. Automated Shimming

i. Global shim techniques, such as quickshim can be used. In this case, it should be very important to choose a FA value that works in our favour, with more signal coming from our region of interest, the liver.

ii. Localized shim techniques, such as ge3d, can also be used. Shim gradient values will be chosen in accordance to the user defined voxel.

b. Manual Shimming

i. Global shimming can be done by loading a regular SPULS sequence. Again, carefully choosing a favorable FA is vital to achieve a good result. Signal should be, as much as possible, coming from our area of interest, the liver, and not the muscle or any surrounding areas.

ii. Localized shimming can be done by loading a PRESS sequence, selecting a voxel of interest and varying the shim gradient values until the desired result is achieved.

8) 31P power calibration should be done in accordance to the Phosphocreatine peak (PCr), with this signal coming from the muscle region, closer to the coil.

9) The animal is now ready to be scanned. Choose the adequate sequences and parameters for your specific purpose.

7. Methods of Data Analysis

While there are several options on the market for MR Spectroscopy analysis, namely LCmodel or even Matlab, jMRUI was chosen. jMRUI (short for Java-based Magnetic Resonance User Interface) is a software package used for processing of MRS and MRSI data. It includes algorithms for frequency selective filtering of signals, correction of eddy current artifacts, Cadzow signal-to-noise enhancement, linear prediction, non-linear fitting, etc. It is mainly developed as part of Marie Curie Framework by the D. Graveron-Demilly group at the Claude Bernard University Lyon 1 in France. The software is not open-source, but licenses are free for academia, on the condition that they register on the website.

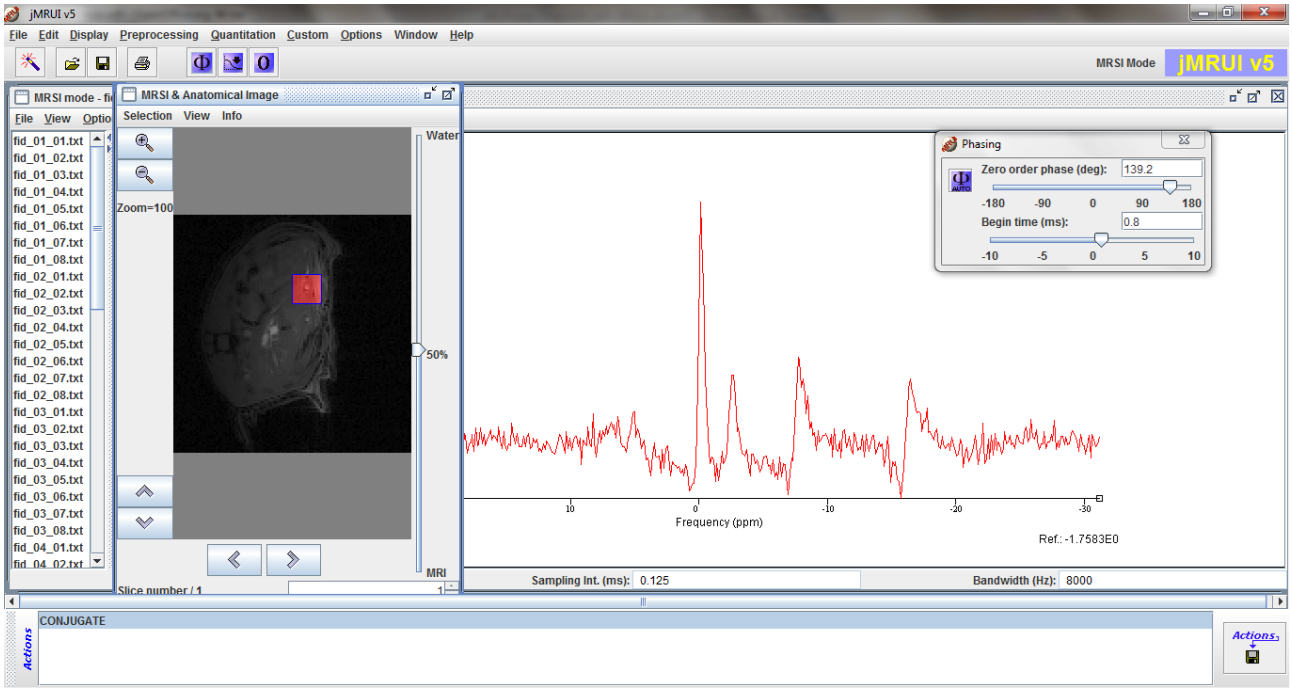

Fig 18 General view of jMRUI. A CSI sequence is displayed, where we can see the anatomical image and the selected voxel, the correspondent spectrum as well as a Phase Parameters toolbox

7.1 Preparation

Before starting to quantify the metabolites present in the spectra, one has to prepare the data for analysis. This procedure includes several steps, detailed below.

The first thing to do is reversing the spectrum (conjugate signal). Raw MR Spectroscopy data acquired in Varian scanners is not automatically presented according to the MR Spectroscopy standard. To fit this standard, one has to reverse the spectra in order to fit the metabolites in the expected frequency range when displayed as PPM.

Next up, comes Apodization, literally meaning "removing the foot", is the technical term for changing the shape of a mathematical function, an electrical

signal, or anything equivalent. It is commonly used in signal processing, usually by means of applying the Hann window in the Fast Fourier transform in order to smooth the discontinuities at the beginning and end of the sampled time record. In purely aesthetic terms, it makes the spectrum appear to be smoother, reducing (or even removing completely. Depending on the degree of apodization) the sharp angles present in each peak. This tends to erase the visual noise usually present in MR Spectroscopy spectra

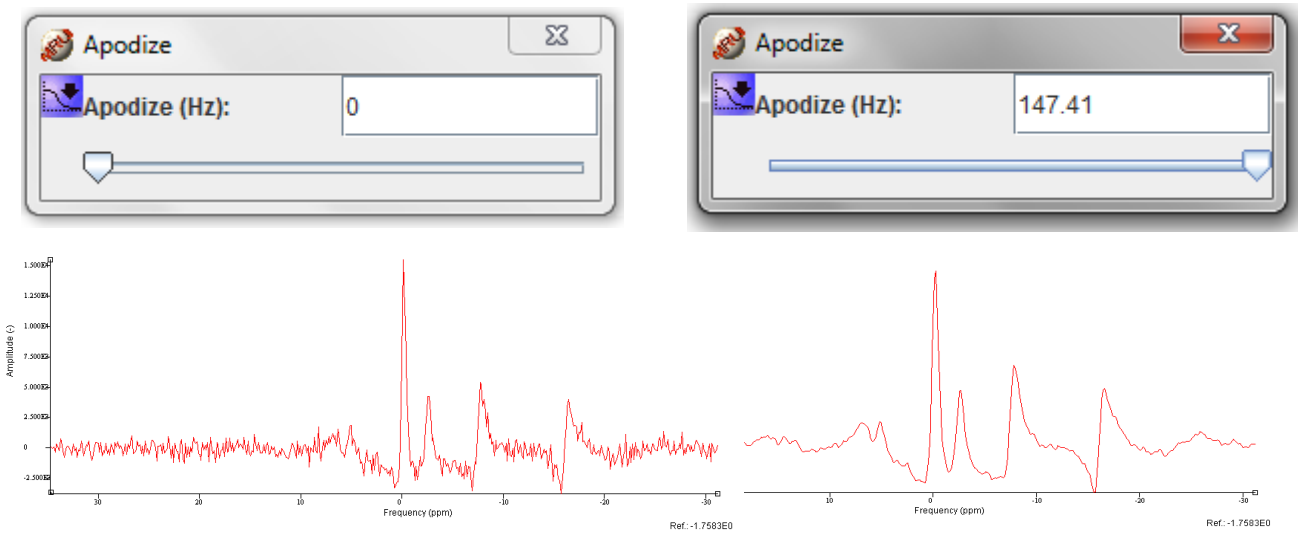

Fig 19 *Apodization Toolbox and its effect on the visual representation of a spectrum. No apodization was used on the left spectrum, as evidenced by the apparently erratic variations, and extreme apodization was used on the spectrum on the left, now displaying very smooth lines*

While the visual effect of apodization is easy on the eyes, it also means one can lose information if used in a careless manner. Luckily, jMRUI presents the option of looking at the apodized data while the analysis is done using the unedited data instead of the apodized one.

The Zero Order Phase parameter is pretty much self-explanatory, as it allows for user to adjust the phase of the signal to better fit the desired interest (pretty much common ground on any signal processing tool available). Due to the intrinsic nature of surface coils (B1 inhomogeneity), this parameter needs to be constantly adjusted to avoid phase issues, as different voxels are affected by different Flip Angles.

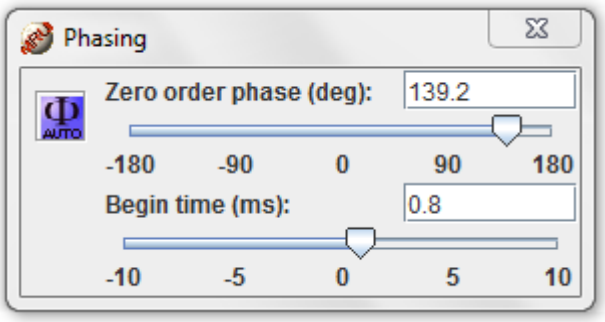

Fig 20 Phasing Toolbox, showing both Zero Order Phase and Begin Time as flexible parameters.

In regards to the Begin Time parameter, its benefits may not be as easy to see. Essentially what it does is it cuts out a determined amount of points at the beginning of the data set. This helps solving some major phasing issues.

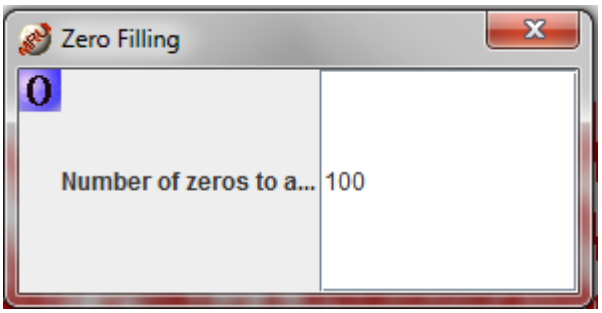

Fig 21 Zero Filling Toolbox, with the number of points to add to the spectrum.

Zero filling is another tool to take into account. It allows one to use a longer FFT, which will produce a longer FFT result vector. A longer FFT result has more frequency bins that are more closely spaced in frequency. This might result in a smoother looking spectrum when plotted without further interpolation.

Although this interpolation won't help with resolving or the resolution of and/or between adjacent or nearby frequencies, it might make it easier to visually resolve the peak of a single isolated frequency that does not have any significant adjacent signals or noise in the spectrum. But, essentially, zero padding/filling before a DFT/FFT is a computationally efficient method of interpolating a large number of points.

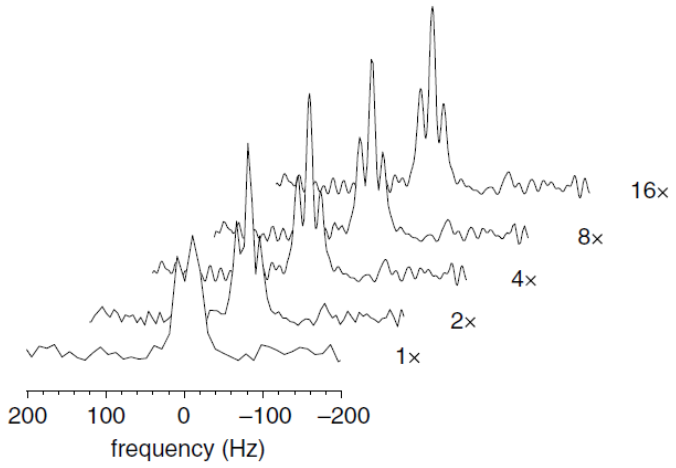

Fig 22 Effect of zero filling on spectral resolution. The triplet resonance Beta-atp is not well resolved after a FT of the acquired data points. Zero filling the original data (by a power of 2), completely resolves the triplet resonance. After four times zero filling no further improvement in spectral resolution is observed (this, of course, on a case by case basis) [14]

7.2 Quantification

And then comes the actual data quantification. For medical diagnosis or biochemical analysis accurate and efficient quantification of magnetic resonance spectroscopy signals is of the utmost importance. However, these signals are often characterized by a low SNR and overlapping peaks, which means that simple signal processing methods such as numerical integration, are all but useless in this field. Starting in the mid-90's, a number of more advanced time domain techniques based on a mathematical model function have been developed [49].

Non interactive methods exist that are computationally efficient and fully automatic. Among these are the very popular SVD (singular value decomposition) and LP (linear prediction) methods, as well as all their variants. Still, a serious drawback is the fact that only very limited prior knowledge can be incorporated in these algorithms and that the model function is restricted to a sum of complex exponentially damped sinusoids. On the other hand, interactive methods exist that provide more user involvement, and do allow the inclusion of a robust amount of prior knowledge, even if they are computationally less efficient.

7.2.1 AMARES

AMARES (Advanced Method for Accurate, Robust and Efficient Spectral fitting), is one of these methods. As defined by its creators, AMARES is an improved interactive time domain method for accurate and efficient parameter estimation of MR Spectroscopy signals with use of prior knowledge. It uses a version of NL2SOL, a sophisticates nonlinear least-squares, which can be adjusted based on prior assumed knowledge. AMARES was first brought up as an alternative to VARPRO, which uses a simple Levenberg-Marquardt algorithm to minimize the variable projection functional. Its performance was confirmed to be superior to VARPRO in terms of accuracy, robustness, and flexibility, in both in-vivo and simulated experiments [49][50]. AMARES is, by definition, dependent on user interaction, which means that the more information the user itself has when analyzing the data, the better. With this in mind, as a way to aid in spectra visualization, every acquired spectrum was apodized.

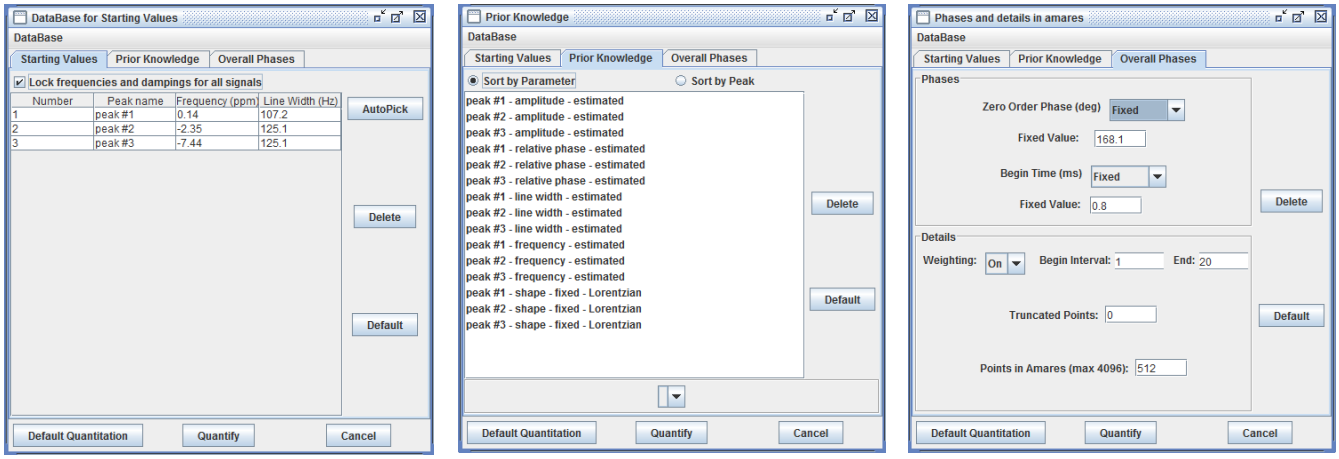

Fig 23 A three way view of the AMARES toolbox as presented in jMRUI, displaying the three main parameter categories at our disposal, "Starting Values", Prior Knowledge" and "Overall Phases", from left to right

Weighting is the multiplication of the first points of the signal, the FID, with a quarter-sine wave. This operation is useful in the quantitation of a signal with a large background signal, or if the FFT of the signal has a bulgy baseline (both usually happen in 31P MR Spectroscopy). For the same reasons, the first points of the FID could be truncated. Truncation of points does not imply physical truncation of the original signal. The quantitation will be performed without the number of points indicated in this field. According to jMRUI's manual, weighting can change the estimated amplitudes for components to about 20% for an interval from the 1st to the 20th point and that truncation can throw away valuable information in the signal, and is meant to be used carefully. In the details field, the number of points used in AMARES can be chosen also.

Prior Knowledge					Phases		Details		
Amplitude	Line width	Relative phase	Frequency	Shape	Zero Order Phase	Begin Time	Weighting	Truncated points	Number of Points
Estimated	Estimated or bound by soft constraints	Estimated	Estimated or bound by soft constraints	Usually Lorentzian	Fixed during the analysis of each voxel. Variable between voxels.	Fixed	On	Usually 2	Maximum, dependent on the acquire data set.

Table 2 Typical values/settings used in each of the AMARES required parameters

The parameters described above are merely representative of the typical settings used within AMARES, and can be altered and improved in relation to specific cases. Luckily, AMARES provides visual aid for this case, displaying both the original and estimated signal side by side for an easy comparison. This way, it is possible to quickly assess if the analysis is working as intended (even if on a purely visual perspective only) and decide whether to move forward with the analysis or to go back and modify some of these parameters to better suit the acquired data.

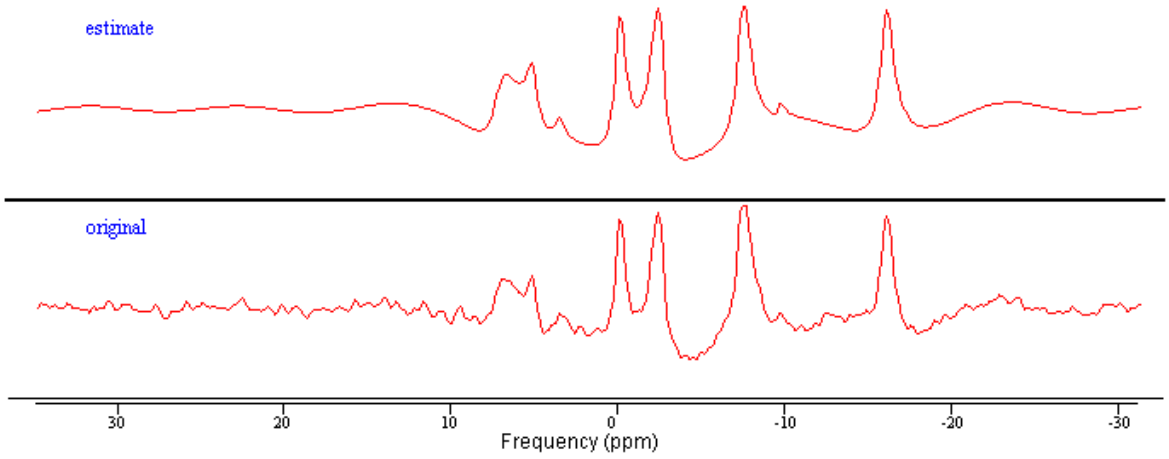

Fig 24 Example of good data fitting using Amares. Estimated spectrum looks similar to the original one.

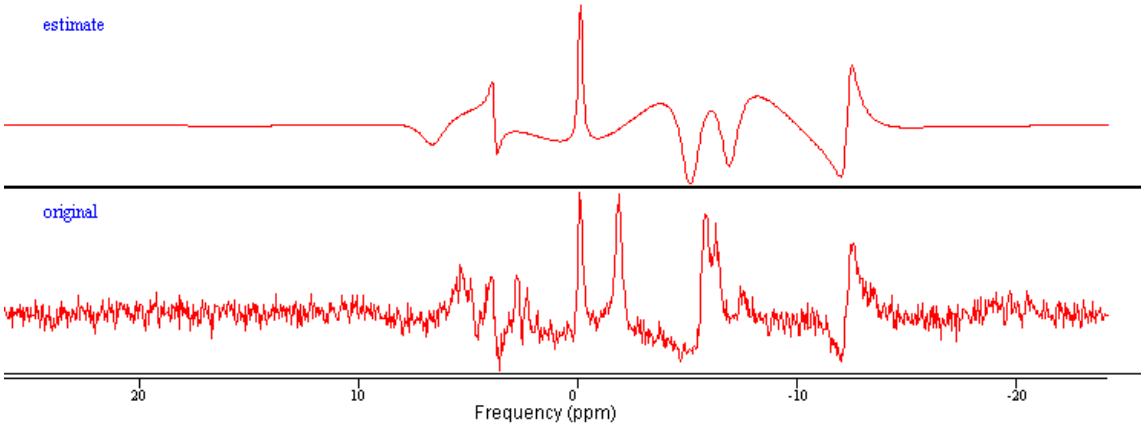

Fig 25 Example of bad data fitting using Amares. Estimated spectrum barely resembles the original.

In the first case, the estimated signal almost precisely matches the one from the

original acquisition. This is the preferred case, as the quantified data will resemble actual acquisitions more closely (residue will be minimized). On the second figure, we are presented with a much noisier spectrum. There are now large discrepancies between the original and estimated spectra, such as unusually wide peaks, mysterious slopes around the -5 ppm area, and general phase issues. This means that AMARES is not doing its jobs properly, and estimation needs to be redone using a different approach within AMARES itself. The estimated components are shown in a much smoother display due to the lack of noise.

Note: There were a number of recurrent bugs found within jMRUI.

The first one relates to the AMARES analysis itself. If the AMARES dialog window is closed during a work session, several problems might occur. These problems range from the inability to select peak line width or automatically selecting several peaks at once, downright to displaying seemingly wrong values during data analysis. Once these problems start to appear they remain present until a new session is initiated. This can be circumvented by not closing the AMARES parameter box between the analysis of different voxels, and merely putting it in the background while the user changes the rest of the parameters.

Another has to do with some data sets that were acquired using the CSI pulse sequence. Jmrui is supposed to automatically detect several parameters inherent to the acquired data, such as the Sampling Interval, Bandwidth, Transmitter Frequency and Main Magnetic Field. While most times these parameters are rightfully displayed, data acquired using CSI has this problem. The correct values need to be manually inserted, otherwise data analysis is meaningless, as the results will take into consideration wrong prior knowledge.

8. Phantom Design

8.1 Liver Phantom

Before the actual in-vivo scanning takes place, MR Spectroscopy sequences need to be chosen, tested and optimized to prevent the use and subsequently needless killing of rodents for academic only purposes. Among the more common alternatives are both the use of already deceased animals (ex-vivo studies), or the use of replacement phantoms.

8.1.1 Concept and early draft

So, the creation and subsequent MRS scanning of a rodent phantom that comprises a "skin/muscle/fat" + liver slice came to fruition. This phantom would be primarily used to test and assess the viability of a number of MRS sequences, optimize its parameters and a get a better perception of the maximum viable scanning "depth". This way, the chosen sequence(s), and its parameters will hopefully have little left to be optimized during the in vivo scan time (relatively speaking), leading to a faster and trouble free experimentation. Still, not all parameters can be fully optimized using a phantom. The schematic in Fig 26 seen here is to be a visual representation of said “skin/muscle/fat” + “liver” phantom, as well as the relative positioning of the surface coil.

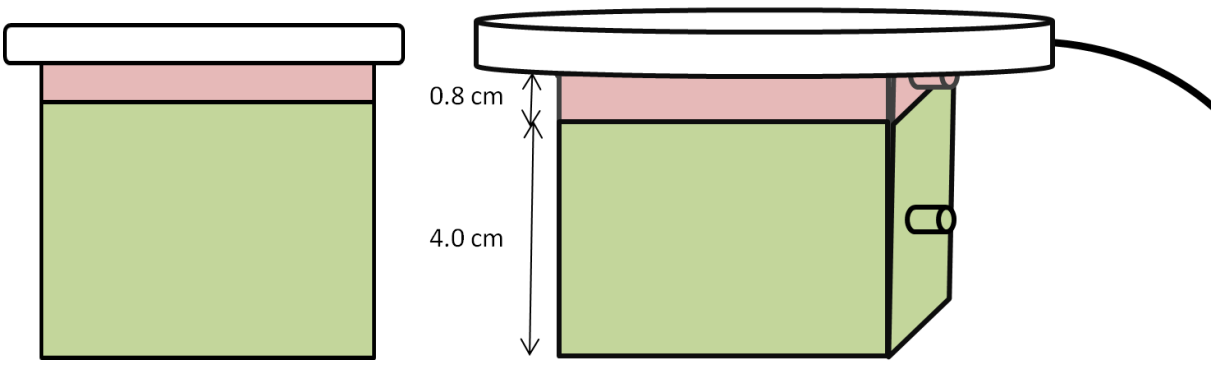

Fig 26 Early draft of the Liver Phantom. On the left, a sideway cut of both compartments and the surface coil on top. On the right, isometric perspective of the Liver Phantom with the surface coil on top.

The two compartments that this phantom depicts have significant differences, both anatomically (in this case, regarding the thickness/depth of each layer), and physiologically (regarding the content of each compartment, in terms of specific metabolite presence and ratio).

Starting by the most outward layer, skin thickness in rats varies a lot with age but remains mostly within small consistent boundaries when oldness is not an issue (Changes in Electrophysiological Properties of Rat Skin with Age). In this sense, if a greater attention to detail is required, the skin compartment’s thickness could be depicted in accordance to the average age of the rats that will be used later in

the in-vivo experiments. In terms of muscle and fat layers, their average thickness tends to vary a lot with various outside factors such as food intake, exercise or even stress [51]. Taking into account several MR scans of common Sprague Dawley rats, an average thickness of 0.8 cm was decided for the first compartment of the liver phantom. In terms of metabolite concentration, studies consistently show that low ratios of phosphocreatine (PCr) to adenosine triphosphate (ATP), high levels of phosphomonoester (PME), Pi, and phosphodiester (PDE) relative to PCr, are present in rat skin [51]. When it comes to muscle composition, Phosphocreatine (PCr) is the most characteristic and easily identifiable metabolite, being present in high concentrations in the muscle and almost totally absent from both the skin and liver [4], quite useful for voxel bleed localization. The second and final layer of the phantom corresponds to the "liver" compartment. In this layer, thickness is not particularly relevant as long as it's guaranteed to exceed the maximum viable range of the phosphorous surface coil (it is a prior assumption that the average liver thickness, combined with the previous layer above will largely exceed it, so it is not a problem here). Even so, to ensure some consistency, the thickness of this layer should be in accordance to the average liver thickness of a rat of similar age to the ones that will be used in the *in-vivo* MRS. Liver phosphorous metabolite composition is fairly simple, and usually consists of 6 (relevant) different components ranging 4 distinct metabolites: PME, phosphomonoesters; Pi, inorganic phosphate; PDE, phosphodiesters; and ATP (alpha, beta and gamma peaks).

8.1.2 Phantom Design and Production

Now that the general idea of what the Liver Phantom should be like was set, there was the need to actually design it and build it. Although the phantom design was quite simple in nature, it was also very specific. It was absolutely necessary for it to have two separate compartments, be easy to fill with a liquid substance and as leak-proof as possible. The desired features, while somewhat flexible, were not so common that you could simply find a container with more or less those characteristics in your everyday life. For this reason, 3D printing was thought of as the most suitable approach.

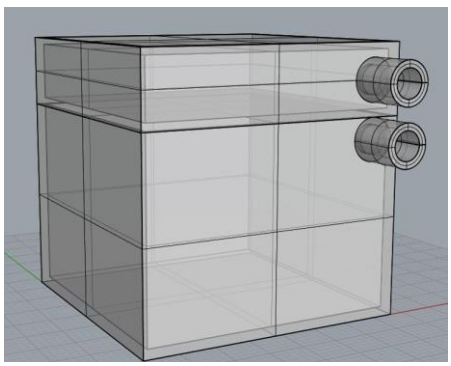

Fig 27 First tridimensional draft of the Liver Phantom. Both compartments are already in place, design is not final

There was now the need for a virtual 3D prototype. And so, a rough draft was made, which included all the chosen characteristics for the Liver Phantom, both in terms of shape and measurements. Taking this rough draft as guidance, a first 3D modeled prototype was conceived (credit to Marta Ribeiro, for her industrial design expertise which proved to be extremely helpful). This first of these models can be seen in Fig 27. After a few tweaks, it evolved into a more precise model, with definitive measurements and proportions. In Fig 28, the final phantom design can be seen, with the two compartments displayed in different colors for easier identification.

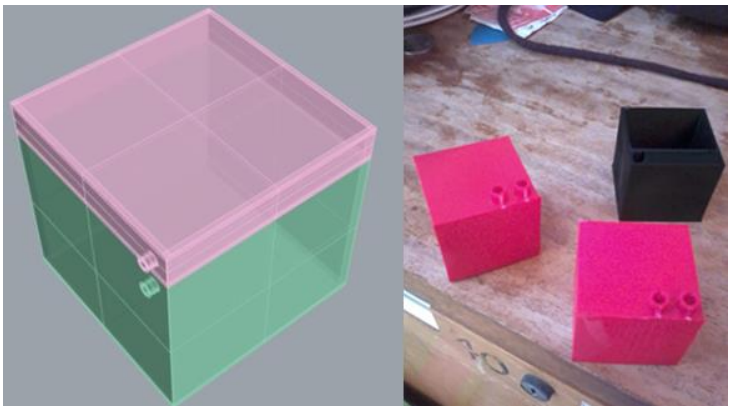

Fig 28 Left: Tridimensional model of the Liver Phantom. The two compartments are depicted in different colors for an easier interpretation. Right: Final, printed version of the Liver Phantom. The two pink duplicates are complete. The black phantom is missing its front side, making it possible to see the two separate compartments.

Now that the final design had been picked, another important topic on this subject is the assembling material itself. Previous studies have used a number of materials to build rodent phantoms, including agarose, latex, slicicone or PVA Cryogel [16][17][18]. In this specific case the chosen material for the phantom structure was ABS plastic, a cheap, relatively strong and supposedly leak-proof material used in, among other applications, Lego bricks.

ABS plastic, or Acrylonitrile Butadiene Styrene plastic (chemical formula $(C_8H_8)_x \cdot (C_4H_6)_y \cdot (C_3H_3N)_z$) is a terpolymer made by polymerizing styrene and acrylonitrile in the presence of polybutadiene. The proportions can vary from 15 to 35% acrylonitrile, 5 to 30% butadiene and 40 to 60% styrene (exact percentages for this phantom in specific are unknown). The styrene gives the plastic a shiny, impervious surface. For the majority of applications, ABS should only be used between −20 and 80 °C as its mechanical properties vary with temperature [52]. Even so, this parameter is well within bounds for this particular application, as the temperature within the MR suite and scanner will definitely fall in that range.

After the final printed phantoms were tested, it was found that the compartments were not fully leak-proof as initially thought. This meant they could not be used in their current form for two reasons: liquid from one compartment could

infiltrate the other one, which would invalidate the existence of two compartments, as they would share the same phosphorous components; also, fluid from either compartment could leak and therefore damage the surface coil, scanner or any equipment nearby. As a redesign and reprint of the phantom was not an option at the time, a more unorthodox approach had to be considered.

And so, there were two problems to undertake: the compartments needed to be leak-proof and the hollow tubes needed to be sealed. The main difference between these two problems is that the hollow tubes cannot be permanently sealed, as they are required to gain access to the interior of each respective compartment.

Looking at the general leak-proof problem, the solution came in the form of a small layer of epoxy resin on the outer side of each compartment, creating a shiny impervious layer to prevent any leakage from the inside. Epoxy is the cured end product of epoxy resins (informal name for the epoxide functional group). Epoxy is also a common name for a type of strong adhesive used for sticking things together and covering surfaces, typically two resins that need to be mixed together before use (which is the case in our situation). Problem is, one the phantom walls in shared between the two compartments, making it impossible to cover with a layer of epoxy, as it would require easy access inside one of the compartments. As there were two fully printed phantoms, it was possible to take the small compartment from one and the large compartment from the other, applying the epoxy resin to each compartment separately.

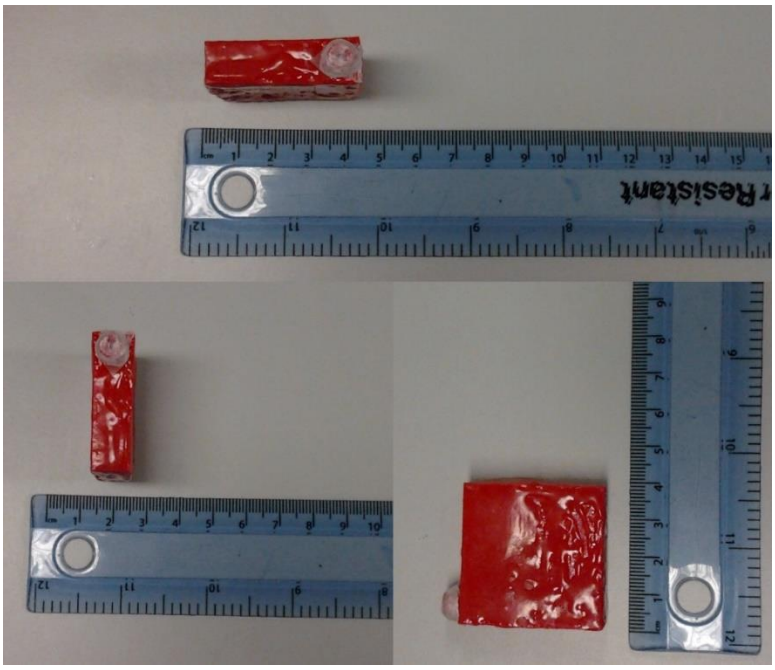

Fig 29 Three-way perspective of the separated small mpartment, after the epoxy resin had been applied.

After the layer of epoxy resin was applied, each compartment was filled with distilled water and left on top of a piece of paper for approximately one hour.

Regular checks on a 5 minute interval confirmed that the compartments were now independently leak-proof.

Next up, the hollow tubes through which the compartments are filled were wrapped in several layers of Parafilm laboratory film to prevent any further leakage.

Parafilm is a plastic paraffin film with a paper backing produced by Pechiney Plastic Packaging Company, primarily used in laboratories. It is commonly used for sealing or protecting vessels (such as flasks or cuvettes). It is ductile, malleable, waterproof, odorless, thermoplastic, semi-transparent and cohesive. It is also used to further seal a lidded container against moisture and air contamination for long term storage. However, Parafilm breaks down over time on exposure to air and light and so, it does not serve as a long-term sealant. Still, considering the overall time frame of each experiment, this fact did not pose any concern.

To finish the phantom assembly, both compartments were taped together using regular plastic tape.

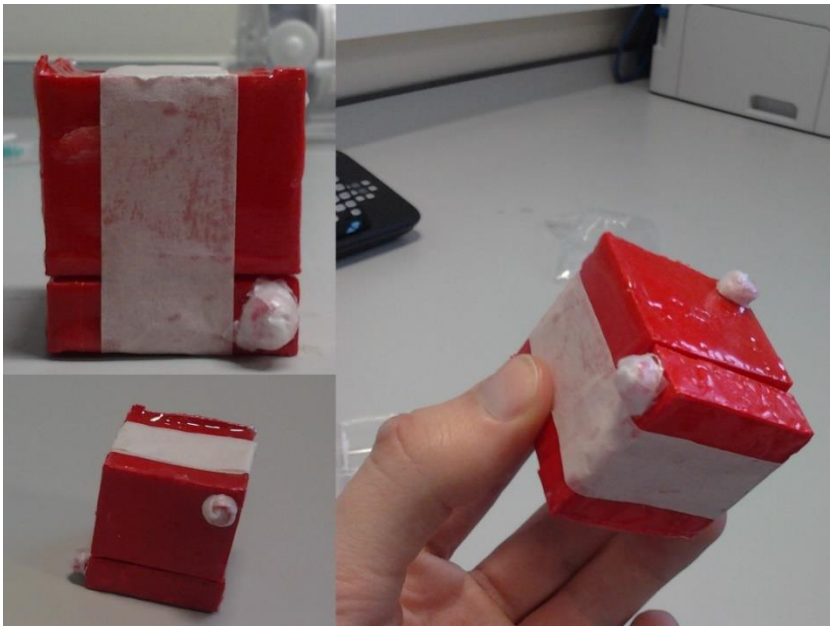

Fig 30 Three-way view of the combined large and small compartment.

Outside of the phantom itself, and even considering all the previously discussed precautions, a final safeguard was put in place. While inside the scanner, the Liver Phantom would be kept inside another container, which would prevent any damage to the surface coil in case there was still a leak. However, having this safeguard meant setting a greater distance (about 1mm more) between the coil and the phantom. Even so, it was considered an important measure.

Fig 31 Final, developed form of the Liver Phantom, next to and positioned inside the small protective plastic container. The container's cap was itself wrapped in parafilm to supplementary prevent any leaks.

Finally there was the need to choose two different phosphorous compounds to fill each compartment of the Liver Phantom. Consensus determined that these compounds should be in liquid form, cheap and easily available, as stable as possible at room temperature and would produce a single peak each in the spectra, separated enough from each other so that they could be easily identified without overlapping. The chosen compounds were Disodium Hydrogen Phosphate for the small compartment and Phenylphosphonic Acid (PPA) for the large compartment. Concentration of each compound should resemble the actual concentration of specific phosphorous metabolites present in the structures we're trying to emulate. For the small compartment (the equivalent to the skin/fat/muscle layer), the Disodium Hydrogen Phosphate solution had a concentration of 40 mM, similar to how Phosphocreatine is present in muscle. As for the large compartment, or liver, so to speak, a Phenylphosphonic Acid solution of 10 mM was picked, like ATP present in the liver. Next, some details on these two phosphorous compounds follow

8.1.3 Phosphorous Components

a. Small Compartment (Disodium phosphate)

Molecular formula	Na_2HPO_4
Molar mass	141.96 g/mol
Appearance	White crystalline solid
Odor	Odorless
Density	1.7 g/cm³
Melting point	250 °C
Solubility in water	7.7 g/100 ml (20 ºC)
Acidity (pKa)	6.83

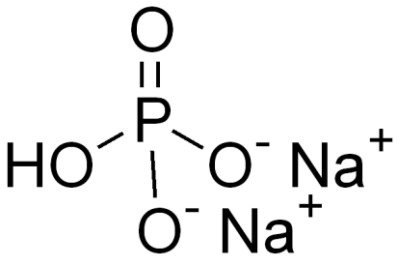

Table 3 Disodium phosphate characteristics and chemical representation [53].

Disodium hydrogen phosphate (or simply Disodium Phosphate) is the inorganic compound with the chemical formula Na2HPO4. It is one of several sodium phosphates. The salt is known in anhydrous form as well as forms with 2, 7, 8, and 12 hydrates. All are water-soluble white powders [54].

It is used as an in conjunction with trisodium phosphate in foods and water treatment. In foods, it's used to adjust pH. Its presence prevents coagulation in the preparation of condensed milk. Similarly, it is used as an anti-caking additive in powdered products. It is used in desserts and puddings, e.g. Cream of Wheat to quicken cook time, and Jell-O Instant Pudding for thickening. In water treatment it retards calcium scale formation. It is also found in some detergents and cleaning agents [55].

For use inside the Liver Phantom:

- Concentration: 40 mM;
- Volume: about 10ml.

b. *Large Compartment (Phenylphosphonic Acid)*

Molecular formula	C_6HO_3P
Molar mass	158.09 g/mol
Appearance	Beige crystalline solid
Odor	Odorless
Density	1.422 g/cm^3
Melting point	163 °C
Solubility in water	Very soluble
Acidity (pKa)	1.85

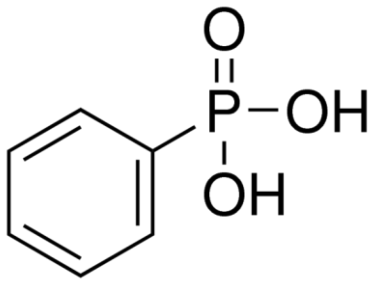

Table 4 Phenylphosphonic acid characteristics and chemical representation [53].

There isn't really much in the way of relevant information about Phenylphosphonic Acid, other than it was recommended for use in MR Spectroscopy because of its stability and ability to produce a single, differentiable peak.

For use inside the Liver Phantom:

- Concentration: 10 mM;
- Volume: about 35ml.

Both solutions were prepared at the University's facilities, using distilled water, regular laboratory glassware and all the standard manual techniques. Scale had a

sensitivity of 0.01g.

8.1.4 Problems and possible solutions

The Liver Phantom was designed with a simple purpose of roughly simulating a transversal cut of a rat, in which both the muscle/skin and liver would be represented by two different compartments. There was no need for it to be a close replica, meaning a lot of the precise details concerning both anatomical and physiological structure were overlooked. With this in mind, it is with no surprise that some shortcomings can be detected on this phantom model.

Without a doubt, the most relevant flaw in the Liver Phantom has to do with fluid evaporation. While both compartments were leakproof, they were not completely air tight, which caused both of them to become less and less filled over time. This can be seen in the figure below on Fig 32.

Fig 32 SCOUT images of a transversal cut of the Liver Phantom with (right) and without (left) the air bubble (absence of signal in the small compartment),

On the left side, a simple SCOUT sequence gives us a 3-axis view of the Liver Phantom, both compartments perfectly filled as far as we can tell. These images were obtained less than 5 minutes after the phantom was put in the correct and final position inside the scanner for one of the experimental sessions. The image on the right was acquired using the same exact sequence and parameters as the first one, only 16 hours later. What we see is an air bubble present in the small compartment of the Liver phantom, as suggested by the darker region in that very same area. As it was previously assessed that both compartments were leakproof, evaporation is the only possible cause for the difference. While not critically important, this is a topic of concern and some possible solutions for this problem will be discussed later on.

The air bubble present in the first compartment grows larger as time goes by, demonstrating the effects of evaporation. These effects seem to have consequences in a short term sense, as the rate of evaporation is quite high, making the phantom practically unusable a day or so after being filled. This issue presents complications in two distinct ways. First, the Liver Phantom needs to be refilled every time a new experiment/scan takes place. Besides being a bit time

consuming, it requires the constant use of the phosphorous components, which may prove expensive in the long run. Secondly, it may prevent the Liver Phantom from being part of long scanning sessions, over the course of a weekend for example, without being taken out of the scanner, refilled and repositioned. As for the reasons of this apparent high evaporation rate, it was suggested that the temperature inside the phantom should be monitored to rule out excessive heating due to the MR scanning. In hindsight, designing the Liver Phantom as two separate units would have simplified the whole process. There's also the possibility that thicker (maybe 2mm) walls could have reduced the evaporation problem without the need for the epoxy layer. The original idea was to get the walls to be as thin as possible, so that the compartments would be closer together, but with that came the leakage problem.

Regarding the second compartment specifically, as the effective coil FOV (specifically in terms of received signal), does not reach a region that can be "seen" by the coil (as the liquid inside tends to stay in the bottom of the compartment due to gravity itself), this can essentially be seen as a non-problem. In fact, we can only assume that this happens in the second compartment as well, as the top of the compartment (where the air bubbles are assumed to be) is not visible in the SCOUT images. One way to verify this would require a different 1H coil, probably a bigger volume coil, to acquire images from the phantom as a whole. As it wasn't deemed important, such task was not performed.

Besides being prone to evaporation and thus the appearance of air bubbles, the Liver Phantom is also difficult to top up. Both compartments had to be carefully and slowly filled with a syringe and needle, to prevent the phantom from having small air bubbles inside. As the This occurrence was quite prevalent in the first uses of the Liver Phantom, sometimes requiring multiple tries until the air bubble either disappeared or was considered small enough for it not to be of importance. Eventually, with some practice, this became less of a nuisance. Still, for a future phantom design it would be wise to consider different possibilities of accessing/filling both compartments.

The overall design should have included some sort of cap to effortlessly seal each compartment after being filled. While it would probably not solve the evaporation problem, it would definitely facilitate it being refilled.

In terms of building materials, previous studies have used a number of materials to construct rat phantoms, including agarose [6], latex [14], silicone [7,11,15] and PVA Cryogel [10]. The latter material is a gel, which has been previously used in the construction of ultrasound and MRI-compatible phantoms [16–19]. The gel is converted into an elastic solid by undergoing a number of freeze–thaw cycles, while the elastic modulus and relaxation times T1 and T2 are controlled by the number of cycles, typically ranging between 2 and 10. PVA Cryogel was previously used by in the development of a rodent cardiac phantom at the

University of Edinburgh's Centre for Cardiovascular Science [56] because of its the ability to readily control the characteristics of the material. High cost, in comparison to ABS plastic made it an impracticable option. Still, the suggestion remains for future applications.

As an end note, one of the original ideas for the Liver Phantom (not previously described in this report) included a third compartment, separating Skin/Fat from Muscle and Liver, and even a variable sized compartment. The first idea was put aside as the differentiation between skin, fat and muscle was not considered to be of major importance. As the relevant structure (the liver) lied beyond that point, the first compartment main purpose was simply to create a big enough barrier between the surface coil and the structure of interest. And so, the idea of having an intermediary compartment was discarded. Now, the concept of a variable sized compartment is a different view altogether. While at first this idea was only thought of as a way to assess the viability of using the surface coil with animals of different sizes (hence the variable size compartment), it would have been very useful for quite a few other experiments.

8.2 PPA Phantom

The third and last phantom (used for absolute quantification purposes) was given the name of PPA phantom. In this case, there was no specific design, material or even shape in mind. The general idea was to have a phantom that was roughly the same size as our structure of interest, MR compatible, cheap and easy to use. Several options were considered, and we can take a look at the actual phantom below.

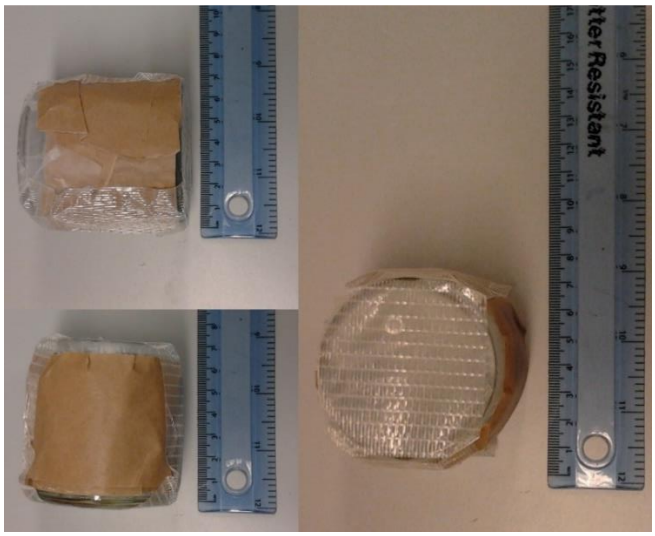

Fig 33 PPA Phantom in three different perspectives.

The PPA phantom is made of clear glass, cylindrical in shape with a single compartment, 7cm height and a 3,5cm diameter, leading to a volume of 269cm^3 (or 269ml). It was covered in several layers of Parafilm laboratory film, as well as

regular plastic tape, to prevent any leakages once filled. Glass, with its non-ferromagnetic nature, low cost and high availability is a very common choice for MRI practice.

As one can guess just by looking at the pictures above, it's a very simple phantom in design, made with materials that can be found in a common laboratory environment. This comes with both advantages and disadvantages, as to be expected. The glass container had already been used as a phantom on previous studies, and can continue to do so after it has been properly cleaned. On the other hand, the container didn't have a proper cover, meaning one had to be improvised. While the same thing had already happened with the Liver Phantom, this time we're looking at an area of 38cm^2 that is totally exposed.

8.2.1 Phosphorous Components

The only phosphorous component present in this phantom Phenylphosphonic Acid, described earlier, this time at 50mM.

Once again, the solution was prepared at the University's facilities, using distilled water, regular glassware and all the standard manual techniques. Scale had a sensitivity of 0,01g.

8.3 FlipMap Phantom

Another phantom used during the course of this study (for B1 mapping purposes to be more precise, as will be discussed later on) was appropriately named FlipMap Phantom. In this case a small plastic container with a bottle cap was used. Cylindrical in shape, with a 1,5cm radius and 5cm height, making for a total volume of 35 cm^3 (or 35 ml).

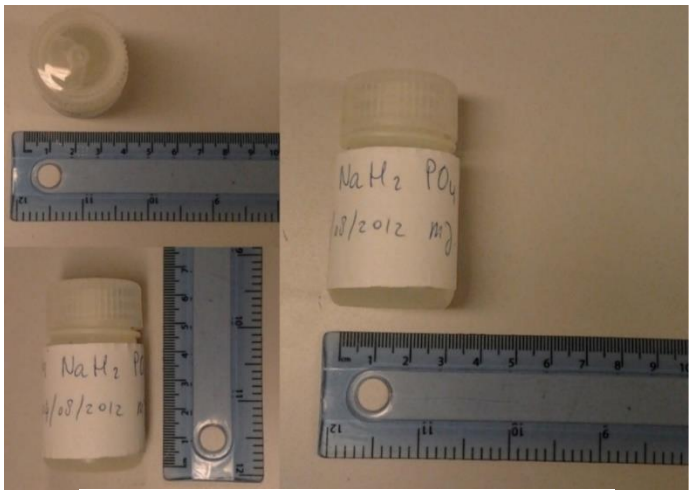

Fig 34 Threeway view of the FlipMap Phantom.

8.3.1 Phosphorous components

Monosodium phosphate

Molecular formula	NaH2PO4
Molar mass	119.98 g/mol
Appearance	White powder or crystals
Odor	odorless
Density	2.36 g/cm3
Melting point	240 °C
Solubility in water	59.9 g/100 mL (0°C)
Acidity (pKa)	4.52

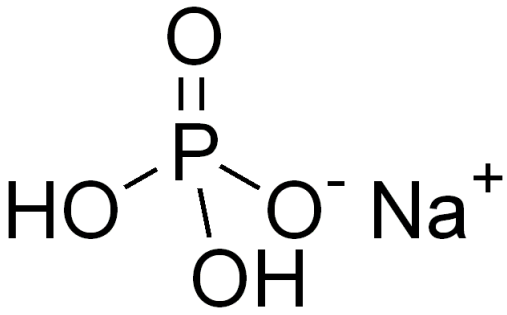

Table 5 *Monosodium Phosphate characteristics and chemical representation[53].*

Monosodium phosphate (NaH2PO4), also known as anhydrous monobasic sodium phosphate and sodium dihydrogen phosphate, is an inorganic compound of sodium with dihydrogen phosphate (H2PO4-) anion. One of many sodium phosphates, it is a common industrial chemical. It exists as an anhydrous salt, as well as mono- and dehydrates [55].

For use inside the FlipMap Phantom:

- Concentration: 1 M;
- Volume: about 50ml.

9. Phantom Data Results

9.1 ISIS

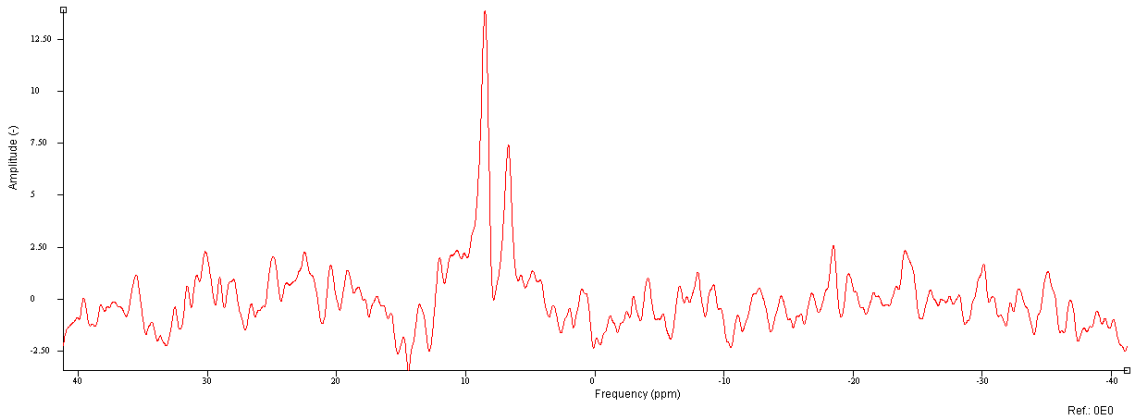

Fig 35 *ISIS pulse sequence | TR 2000 ms | 256 averages | 25x43x5 mm voxel, positioned inside the second compartment | EP [Hard, 90°, 50 µs, 41 dB] | IP [HS-AFP, 270°, 500 µs, 45dB] | Very high apodization*

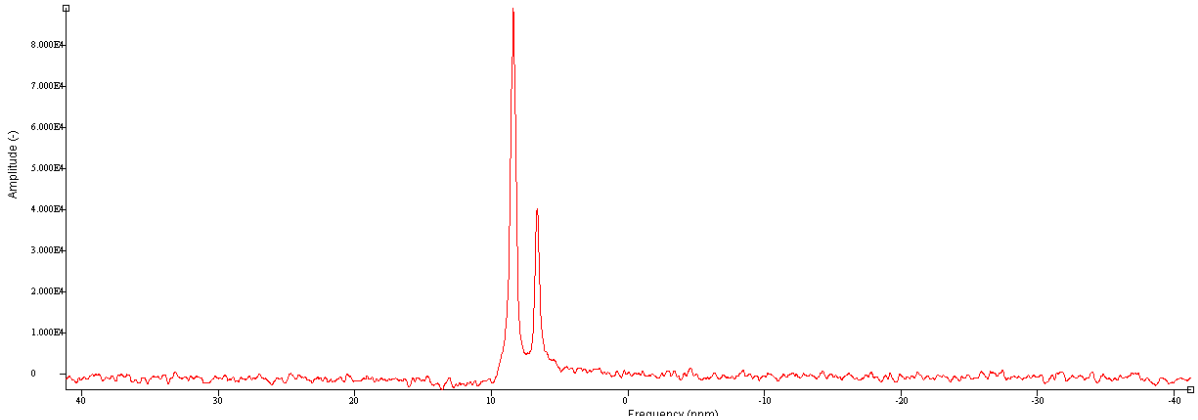

Fig 36 *ISIS pulse sequence | TR 2000 ms | 256 averages | 25x43x5 mm voxel, positioned inside the second compartment | EP [Hard, 135°, 50 µs, 45 dB] | IP [HS-AFP, 270°, 500 µs, 45dB]*

9.2 SPULS

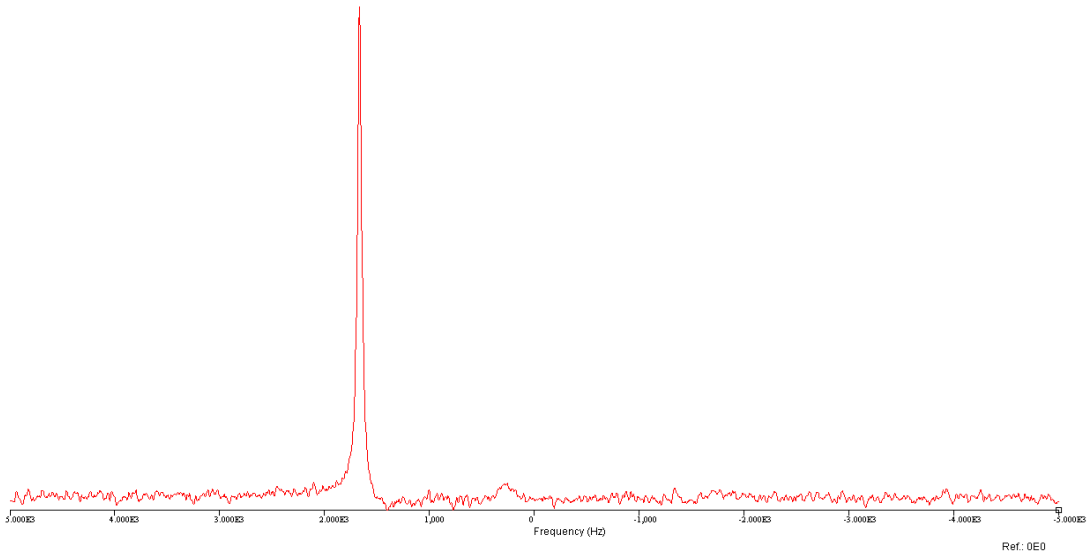

Fig 37 SPULS sequence with a low flip angle, Hard pulse 90° [100 µs, 35 dB] | 16 averages | TR 2000ms |

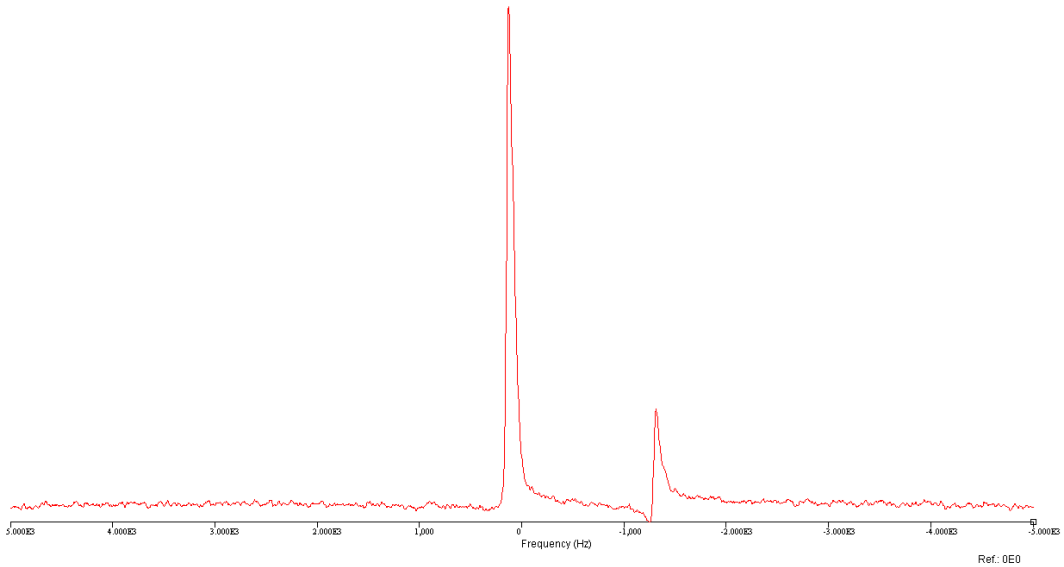

Fig 38 SPULS sequence high flip angle, Hard pulse 350° [100 µs, 44 dB] | 16 averages | TR 2000ms |

9.3 SATSP

Shape	FA	DP/PPA Ratio
hs20	90	7.27

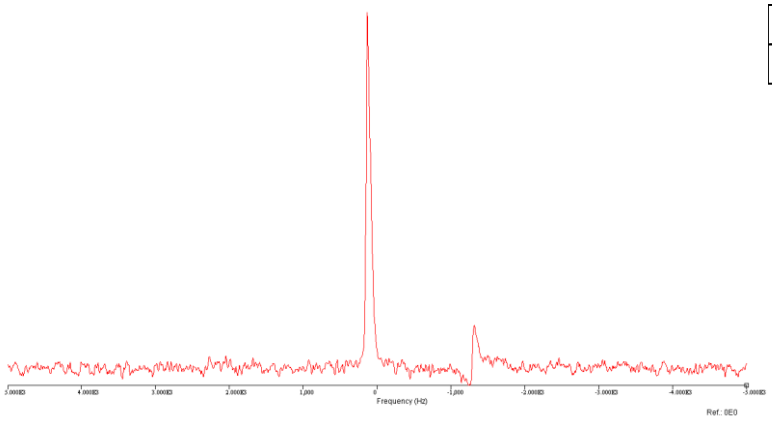

Fig 39 SATSP sequence | EP Hard 350° [100 µs, 45 dB] | SatP hs20 90° [2000 µs, 33dB] | 16 averages | TR 2000ms |

Shape	FA	DP/PPA Ratio
sinc	90	8.54

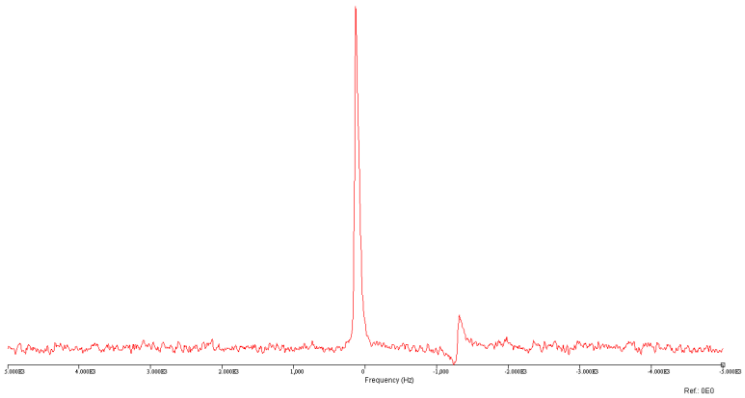

Fig 40 SATSP sequence | EP Hard 350° [100 µs, 45 dB] | SatP sinc 90° [2000 µs, 22dB] | 16 averages | TR 2000ms |

Shape	FA	DP/PPA Ratio
gauss	90	10.99

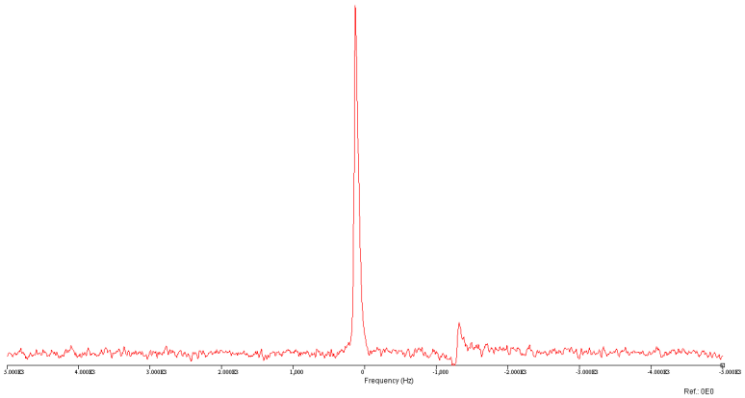

Fig 41 SATSP sequence | EP, Hard 350° [100 µs, 45 dB] | SatP, gauss 90° [2000 µs, 20dB] | 16 averages | TR 2000ms |

Shape	FA	DP/PPA Ratio
hard	350	0.55

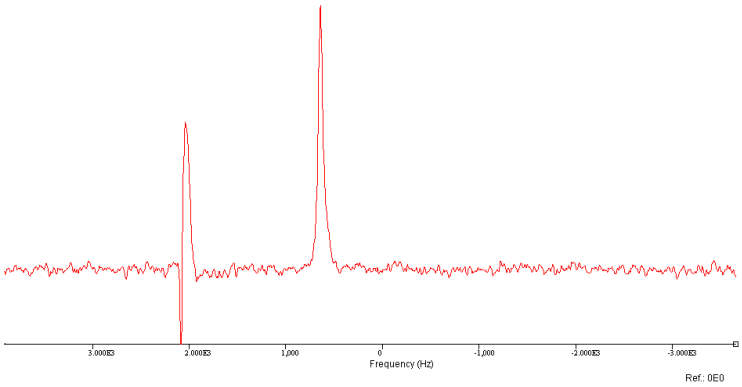

Fig 42 SATSP sequence | EP, Hard 350° [100 µs, 45 dB] | SatP, Hard 360° [110 µs, 44dB] | 16 averages | TR 2000ms |

9.4 Chemical Shift Imaging

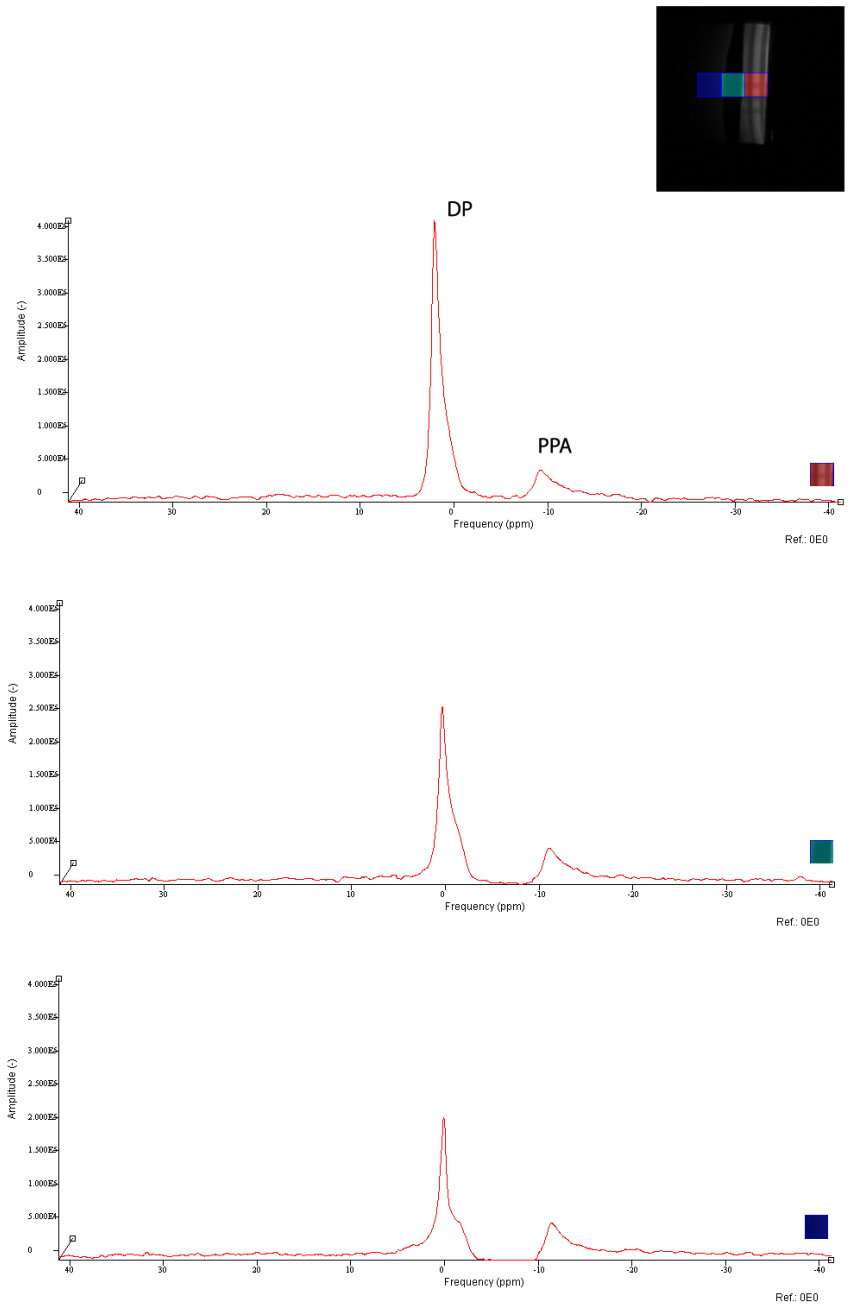

Fig 43 CSI sequence |2 dummy scans | 32 averages | TR 2000ms | Data Matrix 8x8 |Slice orientation – Coronal, Phase 1d 40mm, 2d 40mm, Thickness 40mm |No saturation bands were used

9.5 Phantom Data Analysis

Starting with ISIS, and as stated before, this sequence is very sensitive to slight variations in the acquisition conditions due to its add/subtraction method of voxel calculation. Due to B1 inhomogeneity, a 90° excitation pulse such as the one used in Fig 35 was not giving us the desired results. Due to B1 inhomogeneity, this 90° pulse produces a lower flip angle in regions farther away from the surface coil, such as the second compartment of the Liver Phantom.

Automatic 31P power calibration is done in relation to the higher amplitude peak present in the whole sample, in this case the Disodium Phosphate peak. As this peak is present in the first compartment, closer to the coil, the calculated 90° pulse will primarily affect that area. This is particularly troublesome with ISIS, as this sequence depends greatly on the accuracy of both the excitation and inversion pulses.

A higher powered pulse was needed to ensure that our ROI would be affected by a 90° excitation pulse, thus making the ISIS pulse sequence functional. Fig 36 shows a 135° excitation pulse at work. Both DP and PPA peaks are clearly seen, with SNR being much higher with the same number of averages being acquired (256). This shows that the excitation and inversion pulses are now doing their jobs properly and not cancelling valuable signal information.

There are still a few problems to consider while using this sequence. Because of its nature, ISIS works on an eight acquisition cycle, meaning it can be very time consuming for some valuable results to come through. While increasing the power/flip angle for the excitation pulse does help, it still doesn't solve the issue entirely. If we increase the voxel size so that more signal from the ROI is acquired (thus reducing the need for such high number of acquired averages), it will also increase the flip angle diversity within the voxel, degrading the final results.

Next up is the Single Pulse sequence SPULS. Being a non-localized spectroscopy sequence, it can only give information about whatever metabolites are in the scanned sample as a whole, meaning no voxel-specific spectral information can be acquired. And so, Fig 37 displays the acquired results of a standard SPULS sequence applied to the Liver Phantom, using the usual 90° hard pulse.

As expected, two distinct peaks can be observed, one related to DP and the other to PPA. Also to be expected was the huge difference in their magnitude. Various factors come into play here; the most important two are probably the substance concentration values (40 mM for the DP vs 10 mM for the PPA) and the distance from each compartment to the surface coil (to which the compartment containing DP is closer). Both these factors contribute to the DP amplitude being bigger than the PPA amplitude. Problem is, the compartment of interest is the one containing PPA, which is farther from the surface coil, thus contributing with less signal to the overall results, meaning for a very high

DP/PPA ratio, with an extremely high percentage of the overall signal coming from the first compartment. The plot below details how this metabolite signal ratio can vary by changing the applied pulse flip angle.

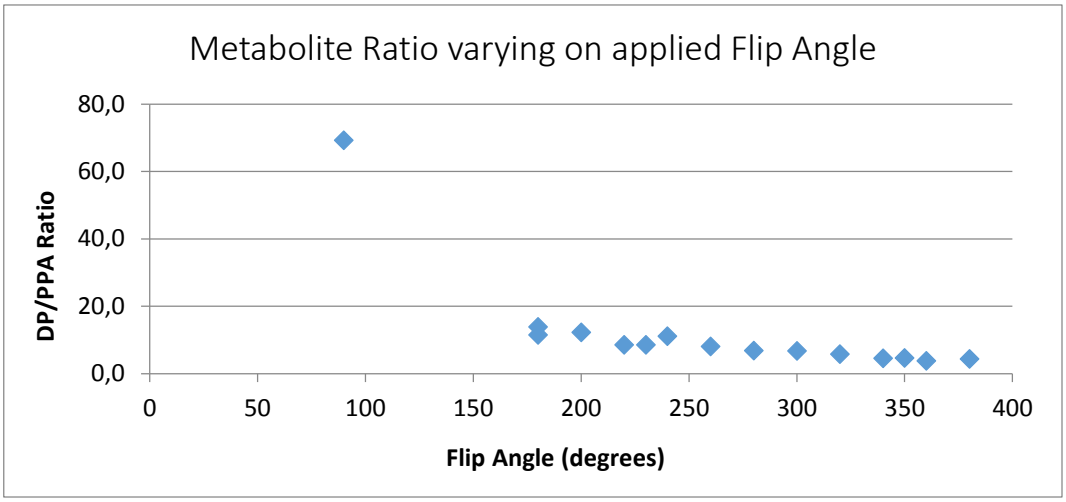

Fig 44 Metabolite Ratio varying on applied Flip Angle

As seen in the plot above, the DP/PPA signal ratio experiences a consistent downward trend as the flip angle (FA) value goes up, even though this sequence is non-localized, and the actual ratio between the two compartments hasn't changed. What this actually means is that it's not the same FA being applied to both compartments simultaneously, making this ratio vary because we're seeing more or less signal coming from one or the other compartment. While the chosen FA might describe somewhat accurately what happens in the first compartment (closer to the surface coil), the same cannot be said about the second compartment (farther away from the surface coil). In this case, more power (in comparison to the calibrated, whole sample, values given by vNMRj itself) is needed to apply a true 90°, 180°, or whatever the desired FA may be, to the second compartment, exactly because of this distance. The next plots should make for a better understanding of this situation.

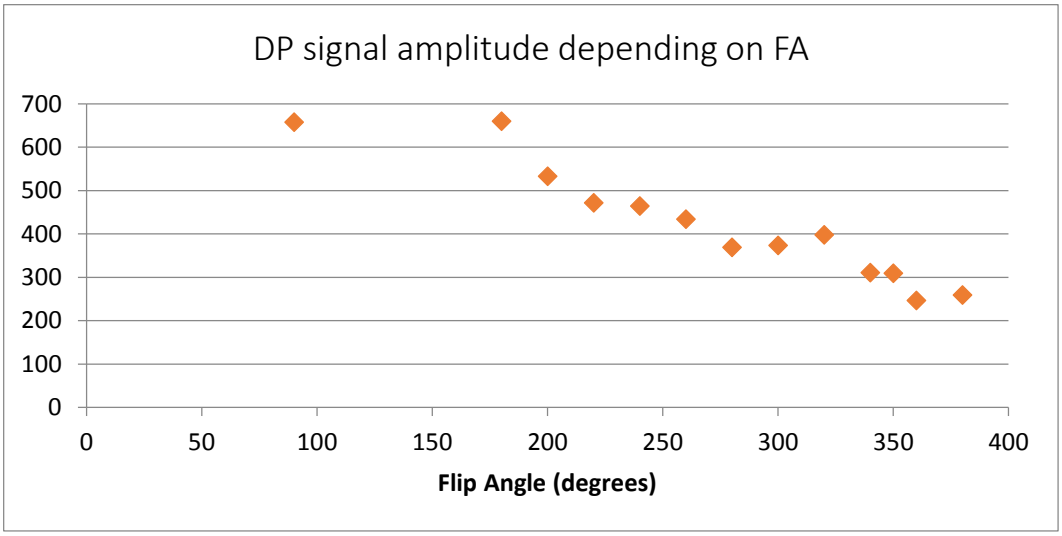

Fig 45 DP signal amplitude depending on FA

Here we can see how the signal amplitude from DP (or first compartment, as preferred, since they act like synonyms in this case) changes by modifying the FA value. Still, both DP and DP/PPA ratio going down (as the FA value goes up) might not be of any interest if the PPA signal goes down as well (just at a slower rate). If this were to happen, the already difficult problem of obtaining a good SNR in-vivo would be even more difficult. Thankfully, that doesn't seem to be the case, as detailed below.

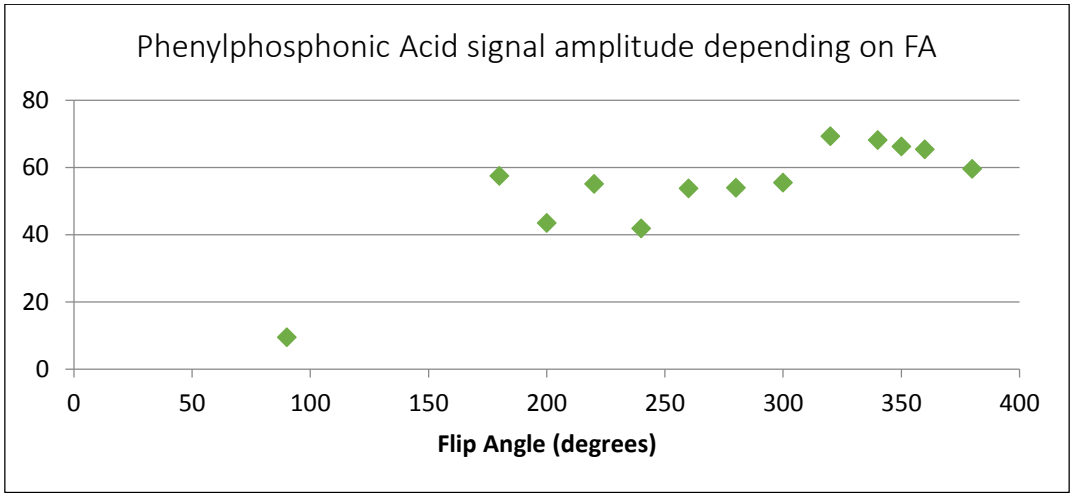

Fig 46 Phenylphosphonic Acid signal amplitude depending on FA

Finally, the plot above (Fig 46) shows how the signal amplitude from PPA (second compartment) varies by modifying the FA value. Even with some noticeable fluctuations, there is a general upwards trend in the amplitude values for the PPA, which shows that a higher FA means higher signal coming from distant (to the coil) regions, in contrast with the decreased signal coming from the first compartment.

Fig 38 displays a typical SPULS spectrum of the phantom, using a high flip angle value (350°), without the use of a saturation pulse. While both peaks are clearly visible, there is still quite a big difference regarding their amplitudes. In the case above mentioned, the DP/PPA ratio is of about 6.3, meaning DP's peak amplitude is about six times bigger than PPA's.

Using a higher flip angle for the excitation, while helpful to the case in question, doesn't completely solve the problem. There is still a lot more signal coming from the first compartment (closer to coil) in comparison to the second compartment of the phantom, and though it may not seem like a big nuisance in this case, as there are only two peaks in the phantom spectra and both have very distinct resonance frequencies, it'll complicate the in-vivo scanning/analysis with its lower SNR and overlapping metabolite resonance frequencies.

So, the SPULS sequence was modified to include the possibility of using saturation pulses prior to the excitation pulse. A number of different approaches to the use of saturation pulses were considered. A saturation band covering the entire first compartment was selected and an array of different pulses shape/characteristics was tested. The usual to use a slice selective 90° pulse before the actual acquisition sequence takes place. In Fig 42, using a hard pulse for saturation purposes, we're not actually saturating the selected region per se, as this specific pulse is not slice selective. So, it's essentially working as a one dimensional saturation pulse, dependent only on the chosen flip angle, and not on the user selected saturation band.

Again, if applying the saturation hard pulse means not only losing signal from the regions closer to the coil, but also from the area of interest, as this type of pulse is not slice selective, then it may not be of much use. Fortunately, this wasn't the case.

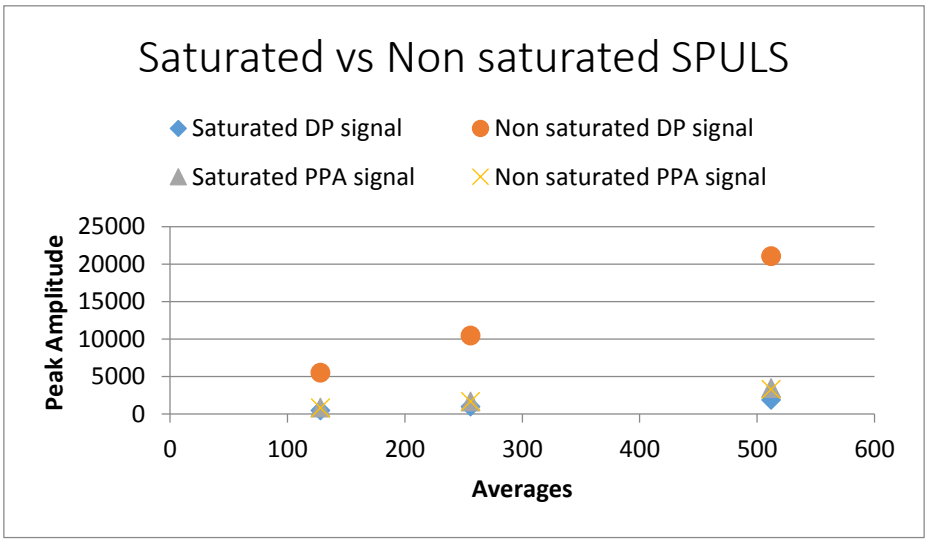

Fig 47 Saturated vs Non saturated SPULS

Peak amplitude for the PPA signal remains independent of the use of a saturation pulse prior to excitation. On the other hand, DP signal (closer to the coil) peak amplitude takes a huge dive when the saturation pulse is used.

This means we get a much better DP/PPA ratio without losing any information regarding the area of interest. These ratios, for the Saturated (SATSP) and Non-saturated (SPULS), can be seen below and they remain constant as SNR goes up.

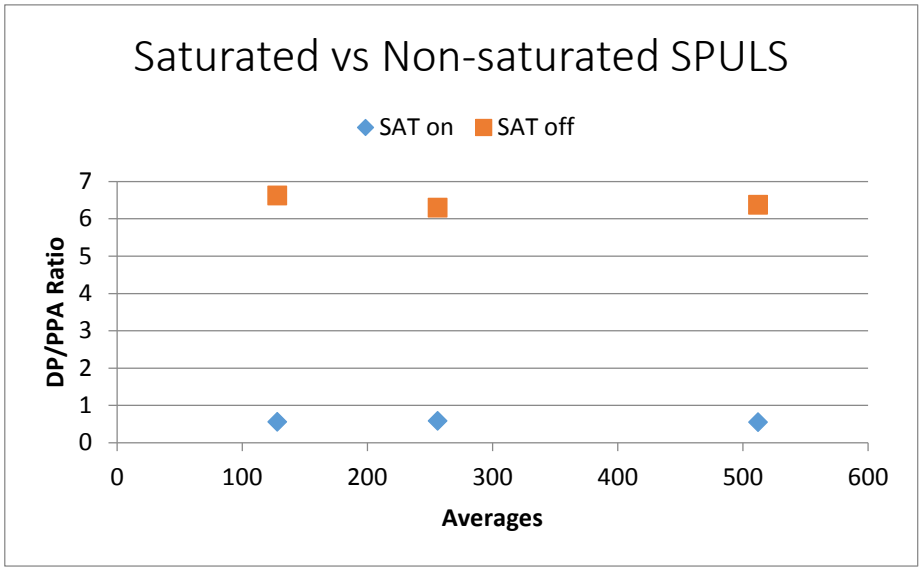

Fig 48 DP/PPA ratio with increasing number of averages

Moving on to the CSI sequence, some promising results were achieved using this pulse sequence with the Liver Phantom. A data matrix of 8x8 was selected meaning that 64 independent voxels can be analyzed and its metabolite composition examined taking into account its location.

As we move further away from the coil and into the second compartment, one can see the decreasing signal amplitude of Disodium Phosphate, while the Phenylphosphonic Acid peak remains more or less constant. Specifically looking at the voxel farther away from the coil, and while there is still some evident signal contamination from the first compartment.

In this case, using the Liver Phantom, a 32 average acquisition was enough to get some good looking results without wasting too much time. The use of saturation bands in conjunction with this sequence was put to use and then quickly discarded, as no suitable results were achieved.

All three sequences (excluding SPULS as it essentially acted as a precursor to the SATSP sequence) managed to produce promising results. While none of them fully satisfied the objective of completely eliminating the signal coming from the first compartment, while retaining the acquired signal from the second compartment, results were consistent enough to move forward to in-vivo testing phase.

10. In Vivo Data Results

10.1 ISIS

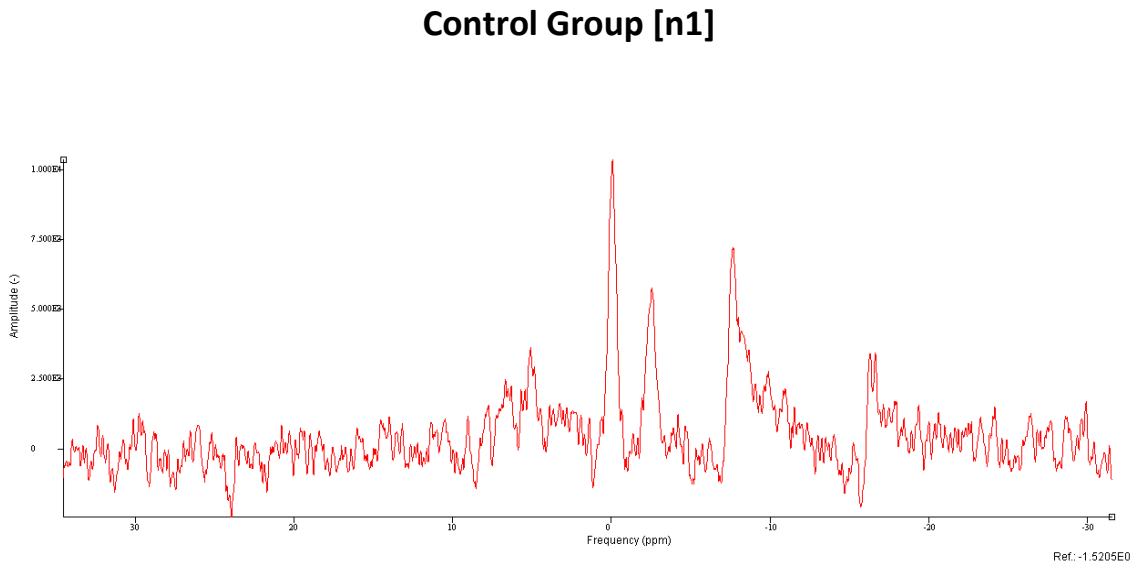

Fig 49 ISIS pulse sequence | TR 2000 ms | 256 averages | 25x31x5 mm voxel, positioned inside the liver | EP [Hard, 200°, 100 µs, 44 dB] | IP [HS-AFP, 260°, 500 µs, 46dB]

10.2 SATSP

Control Group [n1]

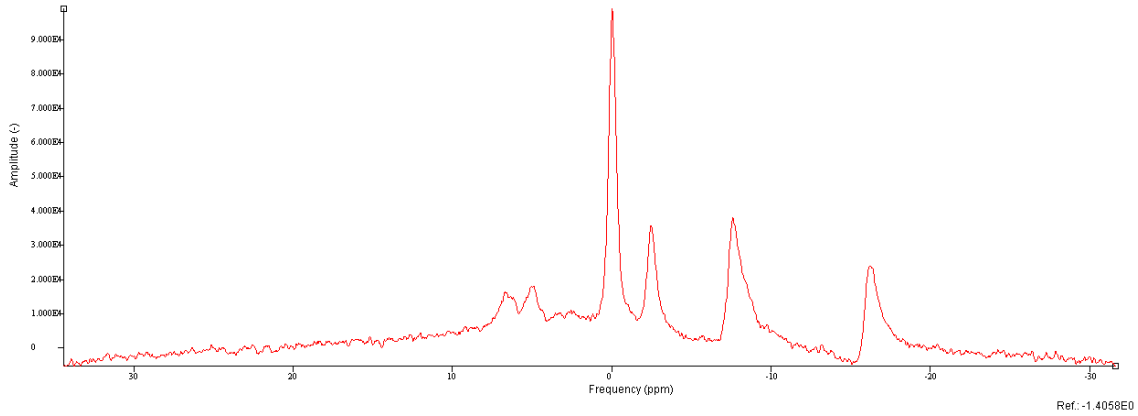

Fig 50 Control Group - subject n1| high flip angle 350° [EP [280 µs, 39dB] | 64 averages | SW 8000 Hz |

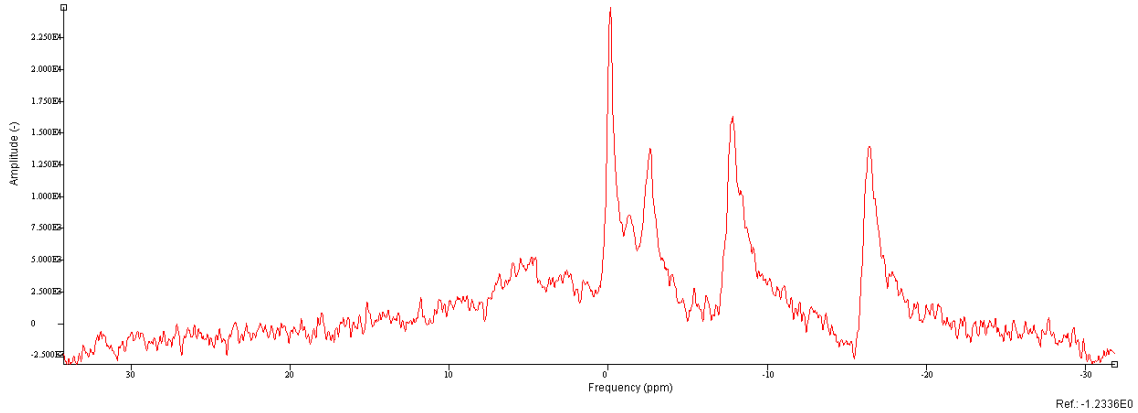

Fig 51 Control Group - subject n1| high flip angle 350° [EP [280 µs, 39dB] | 64 averages | SW 8000 Hz | SP [360° Hard, 140 µs, 45dB]

Control Group [n2]

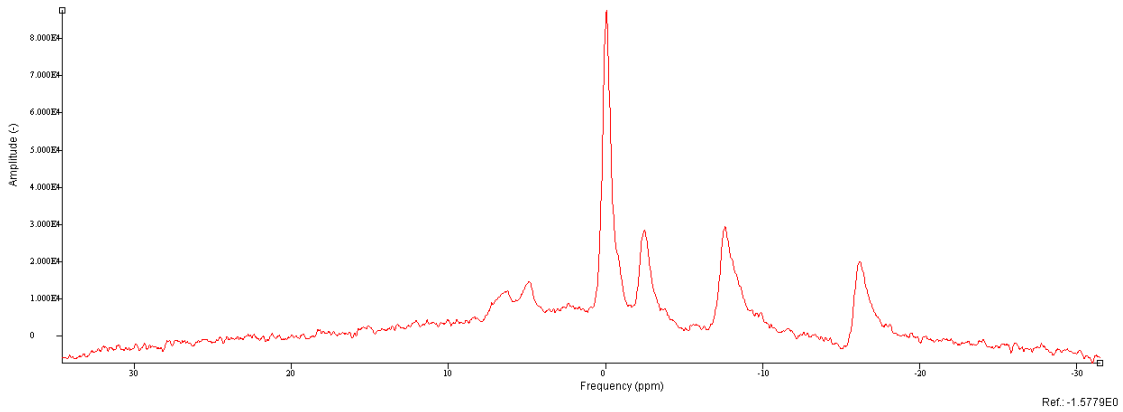

Fig 52 Control Group - subject n2| high flip angle 350° [EP [280 µs, 39dB] | 64 averages | SW 8000 Hz |

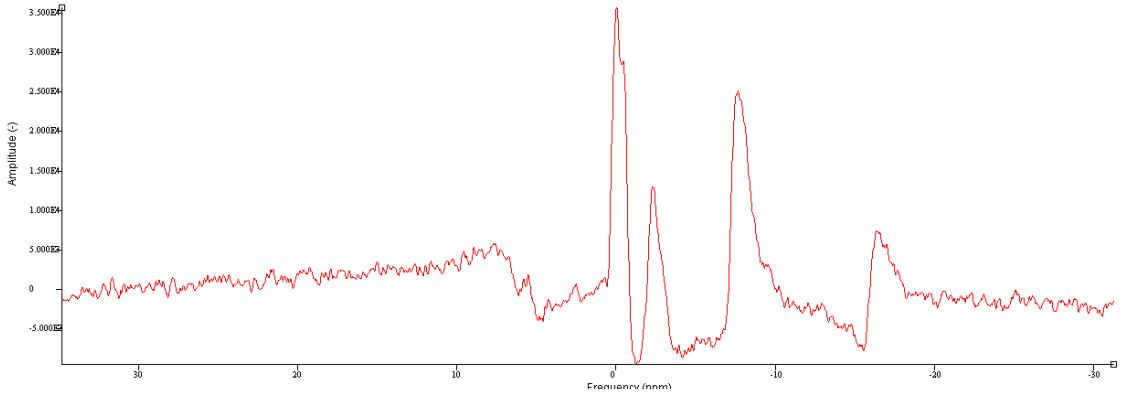

Fig 53 Control Group - subject n2| high flip angle 350° [EP [280 µs, 39dB] | 64 averages | SW 8000 Hz | SP [360° Hard, 140 µs, 45dB]

10.3 Chemical Shift Imaging

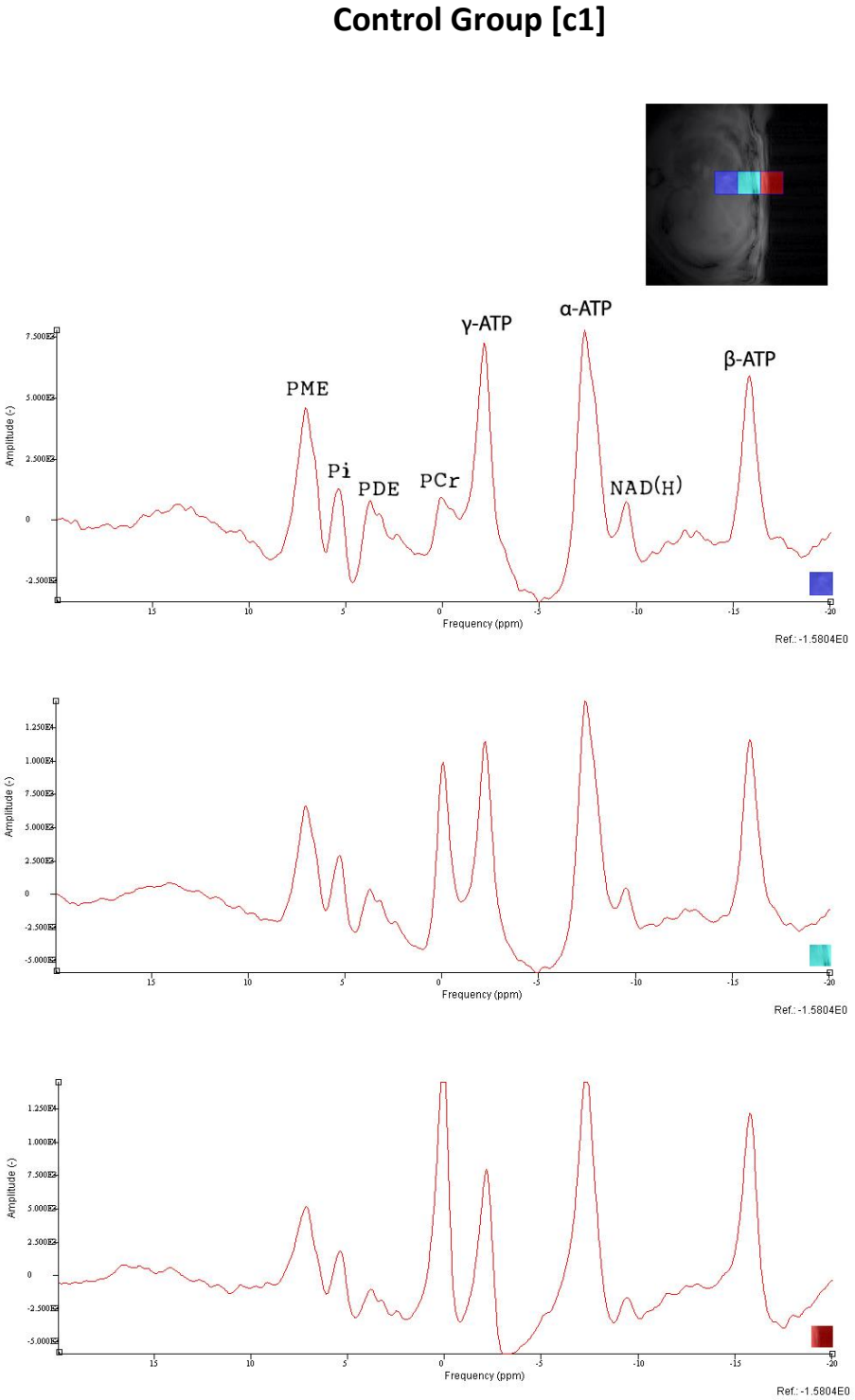

Fig 54 Control Group - subject n1 | CSI sequence |2 dummy scans | 64 averages | TR 2000ms | Data Matrix 8x8 |Slice - Phase 1d 60mm, 2d 60mm, Thickness 10mm |No saturation bands were used

Control Group [c2]

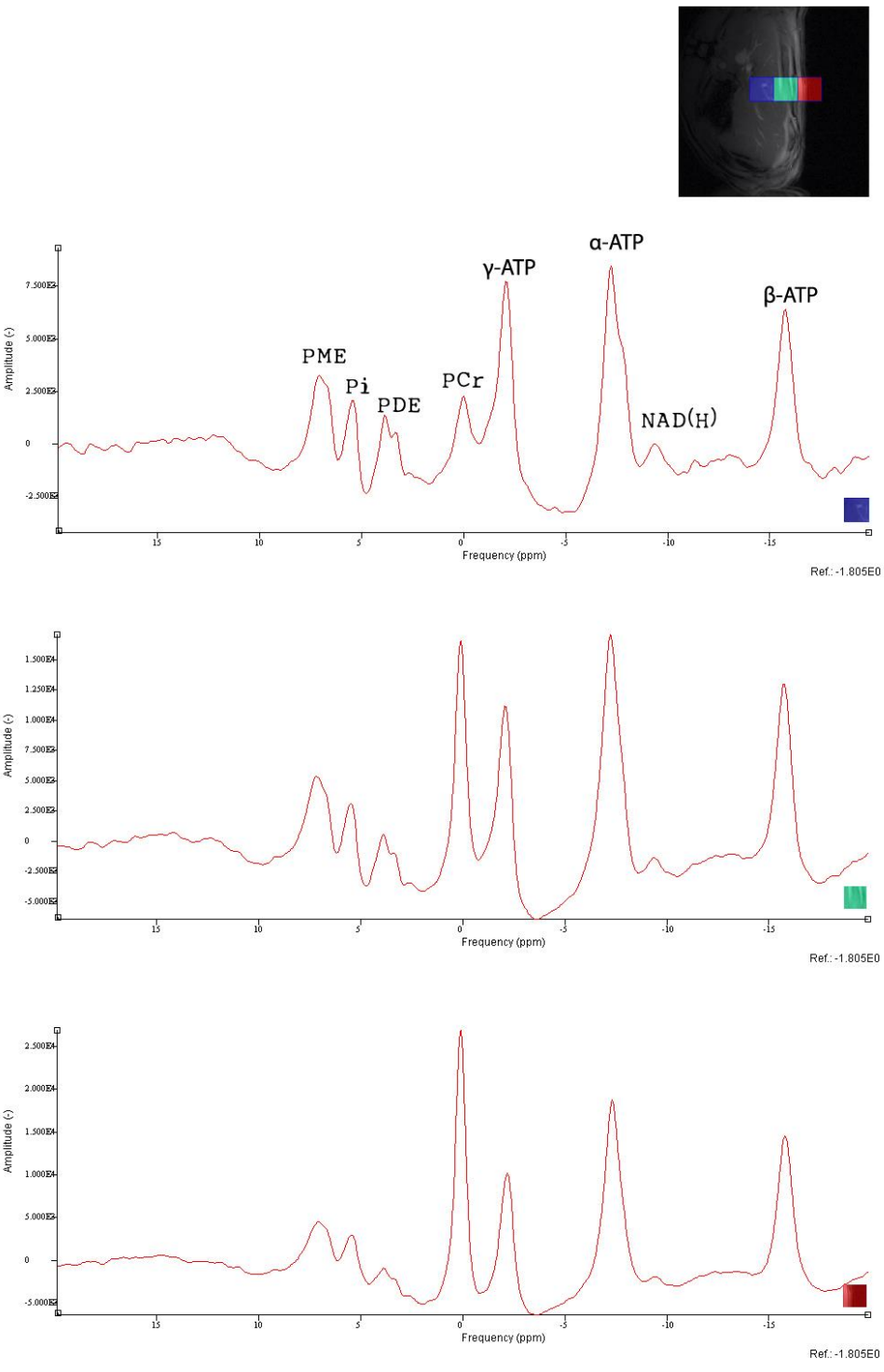

Fig 55 Control Group - subject n2 | CSI sequence |2 dummy scans | 64 averages | TR 2000ms | Data Matrix 8x8 |Slice - Phase 1d 60mm, 2d 60mm, Thickness 10mm |No saturation bands were used

Disease Model [dm1]

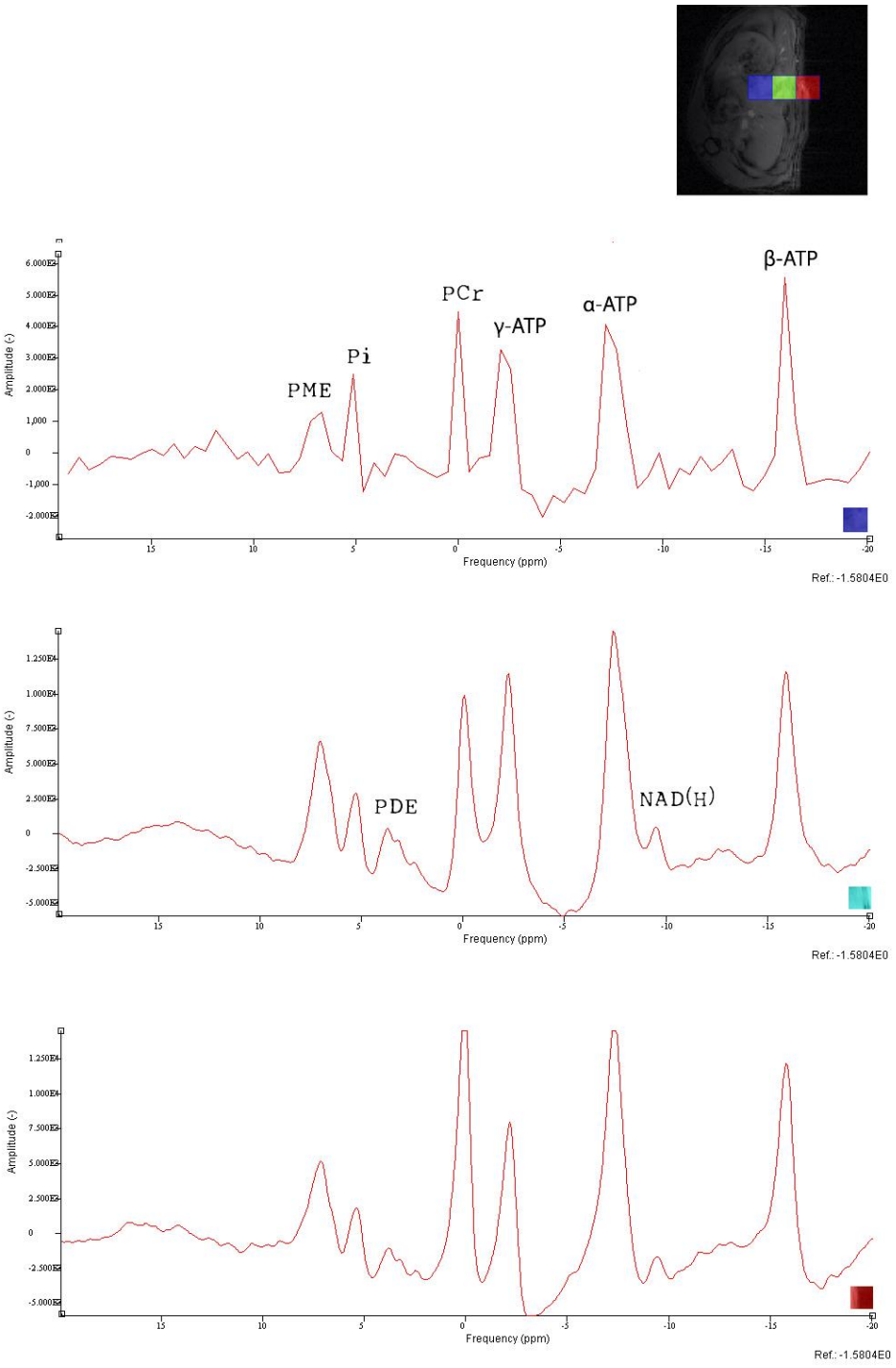

Fig 56 Disease Model group - subject DM1 | CSI sequence |2 dummy scans | 96 averages | TR 2000ms | Data Matrix 8x8 |Slice - Phase 1d 60mm, 2d 60mm, Thickness 15mm |No saturation bands were used

Disease Model [dm2]

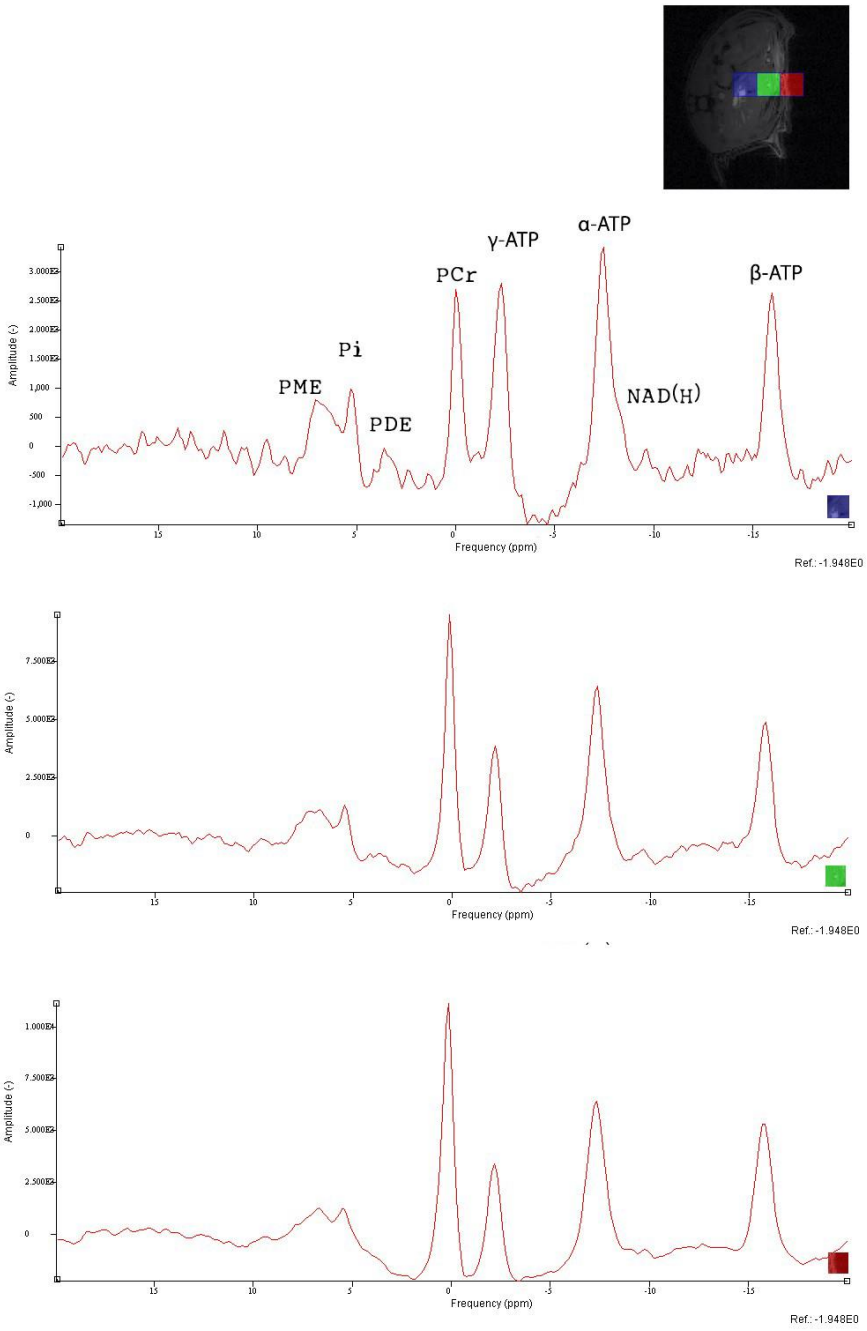

Fig 57 Disease Model group - subject DM1 | CSI sequence |2 dummy scans | 96 averages | TR 2000ms | Data Matrix 8x8 |Slice - Phase 1d 60mm, 2d 60mm, Thickness 15mm |No saturation bands were used

10.4 In Vivo Data Analysis

If we assume that ISIS' biggest problem in this case is the lack of B1 homogeneity, a very troublesome fact for its sum/subtraction localization method.

There are reports of adiabatic pulses being used for excitation in ISIS, with successful results [57], meaning it could be an interesting idea going forward. To put it in context, adiabatic pulses are a class of amplitude and frequency modulated RF-pulses that are relatively insensitive to B1 inhomogeneity and frequency offset effects. They utilize the adiabatic principle where magnetization is manipulated by a slow passage of the B1 field through resonance [58]. With adiabatic pulses spins having different resonant frequencies are inverted or manipulated at different times. This differs from an "ordinary" amplitude modulated rectangular RF-pulse where all spins are affected simultaneously.

One of the ideas that could solve, or at the very least minimize this issue would be to combine the use of a volume coil for RF transmission and the surface coil for receiving, which is a very costly (money-wise speaking) combination. Thus, this option was not considered.

All in all, due to the localization issues and low SNR (comparatively speaking), the ISIS pulse sequence was dropped in favor of the CSI sequence.

In the in vivo environment, SATSP results were not as good as one would hope. Besides the “to be expected” lower SNR, phase problems and peak broadening seem to plague the results, even with some post processing correction mechanisms. While these phase issues were non-existing in a phantom environment, there are some plausible explanations to this occurrence.

In contrast to the phantom experiments, where there are no overlapping metabolites in both compartments, on an in vivo setting we can find, for example, ATP in both muscle and liver. Problem is, muscle ATP and liver ATP don't necessarily have the same initial conditions from our perspective.

To start with, shimming is different in both muscle and liver, as a good global shim is borderline impossible due to the lack of homogeneity between structures, and quite frankly, undesirable, as our structure of interest is the liver and nothing else. This shim inhomogeneity (and B1 inhomogeneity) will result in slightly different resonant frequencies for both muscle ATP and liver ATP, which then results in peak broadening and phase issues.

Secondly, muscle and liver, being at different distances in regards to the surface coil positioning, are affected by different flip angles during this pulse sequence. One way to assess this effect in a more quantitative manner is to create a B1 map,

which was done and will be presented later on. While there are many ways to do this, as previously discussed, the double angle method was picked as the most appropriate.

Also, while the saturation pulse did help quite a bit in reducing the PCr peak as well was decreasing ATP peak width (both presumably because of less muscle signal contribution), it also caused both PDE and PME peaks to vanish almost entirely, and with them valuable information for this study. More so, as the saturation did not cancel muscle/fat/skin contribution completely, all the initial issues are still a factor.

Once again, one of the possible solutions to these issues would be to combine the use of a volume and surface coil, which was not possible during the course of this study. Further use of this sequence was not pursued in order to focus on CSI and its sequence parameter optimization.

In the CSI sequence spectra, six different metabolites could be clearly seen in each spectrum, namely PME, PDE, Pi, ATP (α, β and γ), PCr and NAD(H). As absolute concentration was not considered from the start, we can only look at the results in terms of ratios, relative comparisons between metabolites.

A parameter referred to as Anabolic Charge, AC = {PME/({PME}+{PDE}), was proposed by Noren, et al [42], as a possible tool for evaluating metabolic events in the liver and reflect histopathological changes [59].

In our study, higher values for AC were found in the disease model group, and apparently significant differences were found between the control (AC = 0.85 ± 0.12) and disease model group (AC = 0.61 ± 0.13). These differences corroborate what was said in past studies [42]. Still, due to such a low sample size, standard deviation is considerable.

Looking at all three ATP peaks, ratios between α, β and γ ATP remained more or less constant throughout all subjects, be it control or disease model groups.

Comparatively, higher values for PCr were found in the Disease model group (Phosphocreatine is synthesized in the liver and transported to the muscle cells, via the bloodstream, for storage), though it is uncertain why.

Regarding NAD(H), it is known that ethanol consumption may lead to an increase of NAD(H) in the liver, as NAD(H) inhibits gluconeogenesis by preventing the oxidation of lactate to pyruvate [50]. Our study did not find considerable differences in these values between control and disease model groups.

The biggest constraint here is the very limited number of subjects used in these experiments, preventing any conclusion from being truly validated. A bigger

sample size for both control and disease model groups would greatly benefit this analysis.

Absolute quantification was not taken into account until the later stages of the project (after everything else was working properly), and so, this method was only applied in one subject, from the disease model group. Presented in next chapter are these results. Absolute quantification would be very advantageous, as a direct metabolite comparison between groups would be easily achievable, with no ratio comparison needed.

Later experiments using phantoms have shown that differences in SNR between 64 and 96 average acquisitions may not be very significant (a normalized comparison of results showed very close results). Perhaps a decrease in the number of acquisitions (averages) would be beneficial, without greatly sacrificing SNR. With less averages being acquired, one could use that time to increase data matrix or number of spectral points, for greater accuracy.

11. Additional Results

11.1 Absolute Quantification

While relative quantitation is an important and widely use method of comparison (usually by assessment of ratios between different metabolites), absolute measurements would provide a good complement to the acquired data. For this to happen, we would need a phosphorous source with a specific known concentration to use as reference. One of the most commonly used methods for this application consists in the placement of an external phosphorous source next to the sample that is being scanned. This method doesn't require additional scanning time (as the reference values are acquired simultaneously to the desired data) and proved itself to be quite reliable in past studies [4]. Still, it is not without its problems. For this specific case, complications arrive from the use of a surface coil instead of a volume coil. What happens when a volume coil is used as a transmitter/receiver is that both excitation of the nuclei and signal acquisition will be more or less uniform across the whole sample (or completely uniform if not for shimming issues and other signal degrading effects), meaning that the external phosphorous source could be placed anywhere within the FOV and the results would remain consistent throughout. Sadly, this is not the case with a surface coil. Both excitation and signal acquisition are dependent on the spatial coordinates and how they relate to the position of the coil, meaning that quantitation values acquired from different areas would equate to different absolute values. As the sample and the external source cannot be superimposed or set up symmetrical to the coil, this presents a complicated issue. Also, due to the limited range of the surface coil, placing the external source in the scanner alongside the actual sample would not be considered very wise, as a compromise would most likely have to be made in the positioning of both the sample and the external phosphorous source, benefiting none of them.

And so, another solution had to be considered. The idea was to replicate the exact conditions used during the actual scanning of the sample/subject, from the pulse sequence down to parameters such as the TR, TE, FOV, etc, only now

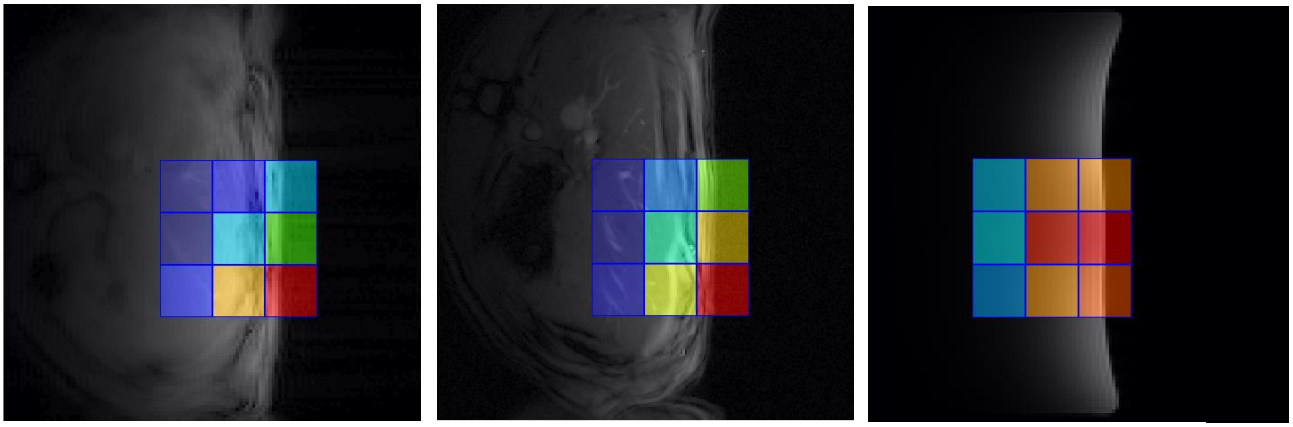

Fig 58 Red squares depicts voxels with higher total combined acquired signal, while blue (all the way to translucent blue) squares represents those with lower acquired signal.

using a specific phantom in the subject's place. For this specific experiment, the PPA Phantom described earlier was used. This PPA Phantom has a known homogenous concentration of 50 mM of PPA. With this information in mind, we can acquire CSI data for this specific phantom and look at it knowing that any voxel that we consider, regardless of the peak amplitude for PPA, will have the same concentration of that compound. From then on, we can essentially do a normalization of these results, take this information we just gathered and apply it to the previously acquired in-vivo data, calculating these absolute concentration values for each metabolite in each correspondent voxel.

The actual process is very simple. For example, if we look at one random voxel for the PPA phantom CSI in Fig 59, let's say voxel *[3,4]*, and the PPA peak amplitude is 1000, we know that this value corresponds to 50 mM in that specific location. If the peak amplitude for PCr in that same voxel, this time on the In Vivo CSI (performed with the exact same conditions as the phantom CSI), is 500 (half of 1000), we can assume that PCr concentration for that specific voxel is going to be 25 mM (half of 50 mM). Each voxel of the PPA Phantom has a unique peak amplitude value and using that value we can calculate absolute concentration values for each metabolite, in each voxel.

Although data was acquired from 32 separate voxels (8x8 matrix), focus remained on 9 voxels roughly located at the center of the FOV, as depicted below on Fig 59, as they included all the structures of interest.

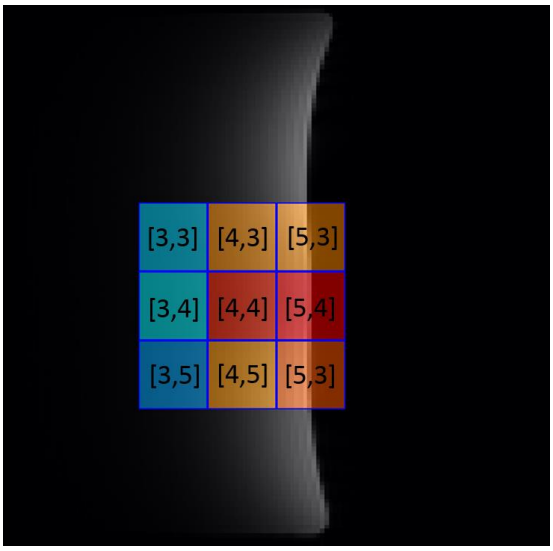

Fig 59 PPA Phantom Voxel label for absolute quantification.

As the idea to acquire absolute concentration data was only considered late during this study, correspondent phantom data was only acquired for the Disease Model group, and not the Control group. *Table 6* displays the absolute concentration values for PME, PDE, PCr, α, β and γ ATP of the DM2 subject.

SUBJECT DM2 - ABSOLUTE METABOLITE CONCENTRATION

PPA Test Data	Voxel	Amplitude	C
	[5,3]	1911	50
	[4,3]	2023	
	[3,3]	1375	

	Voxel	Amplitude	C
	[5,4]	2176	50
	[4,4]	2452	
	[3,4]	1767	

	Voxel	Amplitude	C
	[5,5]	2186	50
	[4,5]	2571	
	[3,5]	1945	

PME	Voxel	Adjusted C
	[5,3]	3.3
	[4,3]	11.8
	[3,3]	21.3

PME	Voxel	Adjusted C
	[5,4]	12.2
	[4,4]	9.4
	[3,4]	22.6

PME	Voxel	Adjusted C
	[5,5]	10.9
	[4,5]	18.9
	[3,5]	19.9

PDE	Voxel	Adjusted C
	[5,3]	2.8
	[4,3]	3.9
	[3,3]	6.3

PDE	Voxel	Adjusted C
	[5,4]	4.0
	[4,4]	4.1
	[3,4]	8.8

PDE	Voxel	Adjusted C
	[5,5]	6.2
	[4,5]	5.1
	[3,5]	6.4

PCr	Voxel	Adjusted C
	[5,3]	29.0
	[4,3]	21.2
	[3,3]	9.6

PCr	Voxel	Adjusted C
	[5,4]	26.1
	[4,4]	16.8
	[3,4]	5.3

PCr	Voxel	Adjusted C
	[5,5]	15.7
	[4,5]	10.4
	[3,5]	2.2

γ-ATP	Voxel	Adjusted C
	[5,3]	12.1
	[4,3]	11.8
	[3,3]	10.6

γ-ATP	Voxel	Adjusted C
	[5,4]	13.6
	[4,4]	12.7
	[3,4]	8.5

γ-ATP	Voxel	Adjusted C
	[5,5]	13.9
	[4,5]	11.5
	[3,5]	8.3

α-ATP	Voxel	Adjusted C
	[5,3]	16.1
	[4,3]	16.6
	[3,3]	22.8

α-ATP	Voxel	Adjusted C
	[5,4]	19.9
	[4,4]	19.6
	[3,4]	16.1

α-ATP	Voxel	Adjusted C
	[5,5]	19.8
	[4,5]	18.7
	[3,5]	13.9

β-ATP	Voxel	Adjusted C
	[5,3]	13.3
	[4,3]	11.5
	[3,3]	11.1

β-ATP	Voxel	Adjusted C
	[5,4]	15.5
	[4,4]	12.6
	[3,4]	7.9

β-ATP	Voxel	Adjusted C
	[5,5]	16.0
	[4,5]	12.5
	[3,5]	8.7

Table 6 Subject DM2 absolute metabolite concentration for each of the 9 considered voxels.

11.1.1 Discussion

Without invasive histological data it is nearly impossible to tell the veracity of these results. Still, if we look at PDE for example, average concentration values stay more or less close to correspondent values found in several articles [4]. Of course, just by looking at one subject, this accounts for nothing more than anecdotal evidence. Also, some studies have shown correlation between spectroscopic parameters and clinical, laboratory and histophatological findings to be very heterogeneous [42].

Although helpful in getting an approximate absolute concentration knowledge, this solution is still not ideal. There are a number of things that can't be properly replicated due to the intrinsic nature/shape/chemical composition of the subject/sample in question. And with this, a few questions arise.

While in a scanning environment, be it with an in-vivo subject or an inanimate sample (either a phantom or an ex vivo subject), the objective is almost always focused on getting the best possible results, through means of choosing the most appropriate pulse sequence, achieving optimal shimming conditions, applying the right TR/TE, etc, this is not necessarily applicable in this situation. One subject's ideal conditions may not directly translate to every case.

Let's focus on shimming for a second. There are two options here: either the shim coil current values are directly copied from the in-vivo setting, which will reproduce the exact in-vivo conditions but not necessarily provide the same results; or one decides to find new values for the shim currents in hope that they will produce results closer to the in-vivo ones. Would it be better to aim for perfect shimming conditions or go for such a setup which will provide results that closely resemble those of the in vivo setting?

Same thing applies to the power calibration settings. Again, there two possible options present: The values for power, pulse width and shape are either directly copied from the in-vivo setting experiments; or the calibration is done all over again, in regards to a specific peak present in the acquired spectra of the phantom. In our case, the calibration was done all over again.

Because almost all systematic errors like B1 inhomogeneity and localization affect the tissue and phantom in similar ways, this calibration method is in principle very robust. The method is only complicated by differences in coil loading between the live tissue and the phantom. Due to logistic constraints and as a way to simplify the procedures, these differences were not considered while making the previous calculations. Still, it is important to identify these issues. Two methods are usually considered to compensate for these differences in coil loading, load adjustment and load correction through the principle of reciprocity.

For load adjustment, it is taken into consideration that the electrical conductivity of the solution in the phantom is slightly lower than that of live tissue (around 0.64 S m–1[14]) such that it allows for fine adjustment of the coil load with a second (smaller) phantom containing, for example, saline. During the procedure of load adjustment, the matching capacitance of the RF coil is left unchanged at the end of the *in vivo* experiment. After removal of the subject and accurate and equivalent positioning of the phantom, the matching is optimized by slowly inserting the saline phantom (i.e. increasing the coil load). When the *in vitro* matching equals the previous *in vivo* matching, the *in vivo* and *in vitro* coil loads should be identical.

For load correction, a phantom should be used with a compound that falls outside the spectral region of interest, such as phenylphosphonic acid (PPA) or hexamethylphosphoroustriamide (HMPT) for 31P MRS. The correction factor for the difference in coil loading is then calculated from the capillary signals obtained from the in vivo and in vitro experiments according to:

$$C_{load} = \frac{S_{in\ vitro}}{S_{in\ vivo}}$$

After which the concentration can be calculated as

$$[m] = \left(\frac{S_m}{S_r}\right)[r]C_n C_{av} C_{load}$$

Alternatively, a load correction term can be obtained by determining the power/voltage to obtain a 90 degree nutation angle in vivo and with the phantom. Through the principle of reciprocity the difference in B1 magnetic field strength is then directly proportional to the difference in acquired field strength.

One of these previously described methods should be taken into account on future acquisitions.

11.2 B1 Mapping

11.2.1 Experimental Setup

While it would have been easier and faster carry out B1 mapping using the 1H coil that would be merely illustrative in a general sense and not accurately representative of the exact effect in question, as all applications in this study are primarily based on 31P MRS.

Due to the inherent conditions of 31P NMR, namely its low sensitivity, imaging is not as simple as with proton requiring a phantom with a much higher (in this case phosphorous) concentration. This way we can increase SNR and, as a consequence, reduce the amount of time necessary to achieve usable results for the before mentioned purpose of constructing B1 maps. For this purpose, a small cylindrical 1 Molar Monosodium Phosphate phantom was used (previously described).

In this case power calibration was done in reference to the lone Monosodium Phosphate peak. Once again, power was fixed, this time at 35 dB, and an array of pulse lengths was used. The 90 degree pulse was then calibrated.

GEMS pulse sequence was used to acquire the much needed images, with a FOV of 100x100 mm, and a 2mm slice thickness. Data matrix was set at 128x128. To avoid relaxation related issues, TR was set at 20000ms and TE at 4ms.

11.2.2 Experimental Data

Several sets of data were acquired for this particular experience. It was known that the number of averages necessary would be higher than usual, due to the phosphorous low sensitivity, we just didn't know by how much. And so, a few different values were tested.

	Flip Angle (degrees)	Averages	TR (s)	TE (ms)	FOV	Slice Thickness (mm)	Data Matrix
GEMS	20	32	10	4	100x100	2	128x128
	20	512	20				
	40	512					
	80	512					
	20	1024					
	80	1024					
	40	1024					

Table 7 Parameters used in several GEMS image acquisitions.

On Fig 60, we can take a look at the visual differences between images acquired with a different number of averages, while maintaining the same flip angle of 20 degrees.

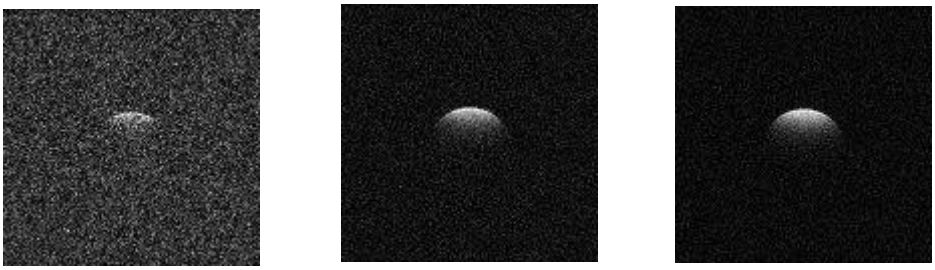

Fig 60 Three FlipMap phantom gradient echo images acquired with different number of averages. From left to right, images were acquired with 32, 512 and 1024 averages, respectively.

As the number of averages climbs, there's a visible difference in the noise level of each image, which is, as expected, showing a downwards trend. The number of averages was settled at 1024, as it was established that the SNR was good enough for the intended purpose at this stage.

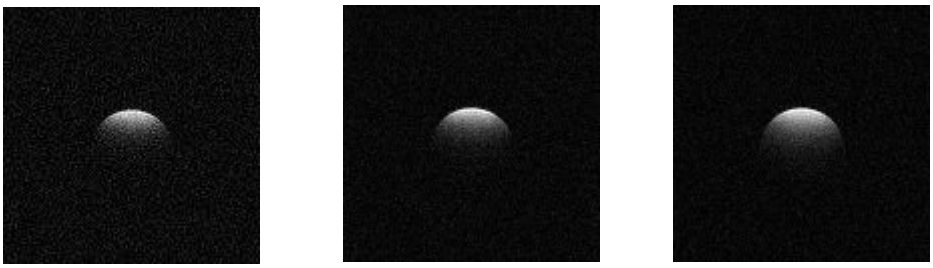

Fig 61 Three FlipMap phantom gradient echo images acquired with different flip angles. From left to right, images were acquired with 20, 40 and 80 degrees, respectively.

The above Fig 61 shows all three acquired images, same sequence parameters with different flip angles (20, 40 and 80 degrees). And while we can make out some differences just by looking at those, its meaning is not obvious at all without it being processed. Still, there is one thing that can easily be accessed with the naked eye: none of these images displays a homogeneous representation of the FlipMap Phantom in terms of signal magnitude.

11.2.3 B1 Map creation (Matlab Script)

To apply the aforementioned method to the acquired results, Matlab was chosen as the primary tool. A small script was written to automatically apply this method to the acquired results, as well as some correction mechanisms that will now be described.

```
%% Both images, acquired with different flip angles, are
%% loaded and converted into doubles. A Flip Angle matrix
%% (FA) is defined, having the same size as the previously
%% loaded images. This FA matrix will later carry a flip
%% angle value for each pixel. doublei40 matrix is created
%% as the supposed multiple of matrix i20.
```

```
i40 = imread('NaP 1024av 40deg.jpg');
i80 = imread('NaP 1024av 80deg.jpg');
i40 = double(i40);
i80 = double(i80);

FA = zeros(128,128);
doublei40 = 2*i40;

%% A threshold (T) is set for the signal magnitude, below
%% which a specific pixel is considered to be noise.

T = 45;

for i = 1:1:128;
    for j =1:1:128;

        if  doublei40(i,j) < T
          doublei40(i,j) = 1;
        end

        if  i80(i,j) < T
          i40(i,j) = 1;
        end

        FA(i,j) = acosd(i80(i,j)/doublei40(i,j));
    end
end

%% New matrix FAR (Flip Angle Real) cuts out the imaginary
%% part of the FA matrix. Then, a noise reducing mechanism
%% is applied.

FAR = real(FA);

for i = 1:1:128;
    for j =1:1:128;
        if  FAR(i,j) > 80
          FAR(i,j) = 1;
        end
    end
end

imagesc(FAR, [20,70]);
```

For the code to work as intended, the position of the phantom/subject must be kept exactly the same in relation to the coil, as the algorithm assumes that the position of each pixel is the same for both acquired images.

11.2.4 Generated B1 maps

By applying the Matlab script as described we can finally see the abovementioned B1 map, in Fig 62 and **Error! Reference source not found.**, through which an easier interpretation is possible.

And while now there's a somewhat clear flip angle gradient from top to bottom, there are still a few things that could be done to improve this analysis. To start with, we know that every region in the second acquisition was exposed to a

higher powered pulse than the correspondent region in the first acquisition. Going by the power calibration done prior to acquisition, we also know that both pulses had a maximum flip angle (closer to the coil) that is lower than 90 degrees.

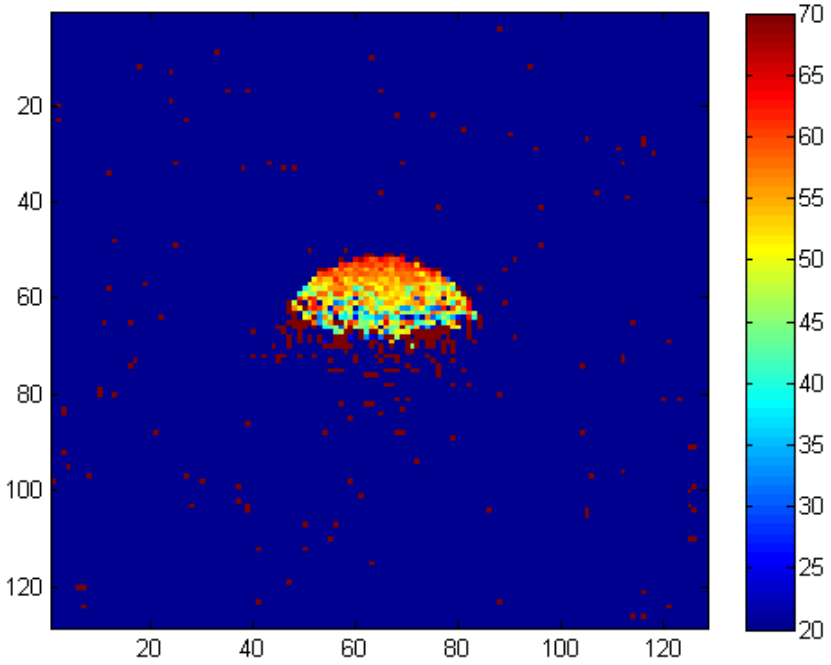

Fig 62 *Generated B1 map without the noise correction algorithm*

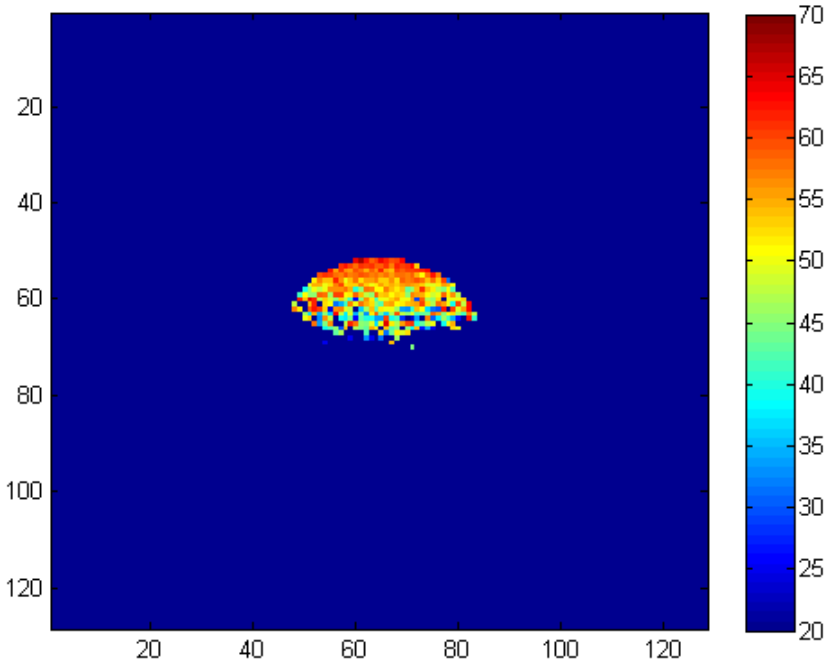

Fig 63 *Generated B1 map with the noise correction algorithm.*

The first thing one notices is that the Doty30 surface coil's average range

accounts for slightly less than 2cm (each pixel in Fig 62 and **Error! Reference source not found.** accounts for about 0.78 mm), which greatly reduces its functionality. Looking back, as a way to increase accuracy in this study, the FOV could have been reduced, while the data size matrix should have been upsized. There was no need for the field of view to be this extensive, given both the size of the phantom in question and the assumed (and now more or less known) range of the surface coil. A new data set could perhaps be acquired with these considerations in mind, hopefully with results even more precise than the ones present here.

In addition to the technical relevance of this apparent flip angle gradient to the SATSP sequence, these calculations are a good way to illustrate why the ISIS sequence didn't quite work as expected. As a sequence that relies heavily on the sum and subtraction of data acquired using different flip angles, it's no wonder the results had severe complications, even with the adiabatic pulses being used.

12. General Discussion

Generally speaking, with such a short number of subjects present in both control and disease model groups (only two for each) it's difficult to reach any indisputable conclusions about a specific kind of natural liver fibrosis/cirrhosis biomarker. Results were consistent with prior studies [4][42], but they're not necessarily statistically relevant due to such a low sample size. What we can say for sure is that these techniques, from subject preparation, pulse sequence parameters, to data analysis, look like a reliable and consistent way of acquiring liver composition data in a secure, non-invasive way. While ^{31}P MR Spectroscopy is already used for the attainment of liver metabolite data, few studies available have reached this level of detail throughout all the stages of the process. Producing a study with a much higher sample size would definitely yield statistically conclusive results and bring a lot more answers to the table.

Also, when considering the whole picture, probably the utmost obvious natural progression would be to perform a subsequent longitudinal study. While transversal studies (cross-sectional studies) usually lend themselves to an easier approach, it's important to recognize the significance of longitudinal data in this line of work. A longitudinal study, as a correlational research study that involves repeated observations of the same variables over long periods of time, is often used to study developmental trends across the life span of a subject, such as predictors of certain diseases (which fits right in in this study). The reason for this is that unlike cross-sectional studies, in which different individuals with same characteristics are compared, longitudinal studies track the same subjects, and therefore the differences observed in those subjects are less likely to be the result of slight differences across or within generations. Because of this benefit, longitudinal studies tend to make observing changes more accurate.

Still regarding the accuracy of the acquired data, and while the main driving force behind these novel techniques relies on the possibility of assessing the chemical composition of a living being in a non-invasive way, there is probably no better manner to verify the reliability of the acquired MR Spectroscopy data than performing a liver biopsy on the test subjects. This way it is possible to have a direct comparison between all the acquired data, which would be particularly useful to test the robustness of not only the applied MRS sequences, as well as the related methods of analysis, etc, thus reducing the need for this invasive procedure in the future. Still, this line of thinking brings several problems to the table. Possessing both MRS and biopsy data while performing a longitudinal study might prove itself to be quite complicated, as it is necessary for the subjects to remain alive throughout the whole study, which may take place over the course of several months. Considering the main point of acquiring longitudinal data is the possibility of studying the progression of a disease/condition in a single subject (or group of subjects) it would be a requirement to have both the biopsy and the MR Spectroscopy data acquisition performed roughly in the same timeframe, at several pre-determined points over the course of the study. As

stated before, previous studies have shown correlation between spectroscopic parameters and clinical, laboratory and histophatological findings to be very heterogeneous [42], so it would definitely be interesting to gather some results and compare them with these past studies.

While several phantoms were used throughout this study, it makes the most sense to focus on the Liver Phantom for this last discussion. As previously discussed, the variable sized third compartment would be a great addition to this phantom. In addition to this idea, and to further simplify the experimental setup, this new variable compartment wouldn't necessarily have to be filled with anything. As the main advantage in this variable sized compartment rests in the possibility of assessing an approximate voxel contamination/bleed due to the components present in the compartment closer to the coil, it would just act as a no signal barrier between the two compartments containing phosphorous components. All in all, tridimensional printing technologies have experienced an enormous growth on the past few years and this seems like a great path to take for the foreseeable future.

Looking at this investigation as a whole, results were mostly consistent between pulse sequences used, even if we take into account all the phase issues with the SATSP pulse sequence and the spin/flip angle problems with ISIS. A few other pulse sequences, such as STEAM, SPECIAL or PRESS were also used during the course of this study but due to the lack of noticeable improvement of the results after a few tries, optimization and use of these sequences was halted in favor of the pulse sequences we see described before.

The SATSP sequence was the only sequence made from the ground up for this study, and while it has shown some promising results, it's still very much in its early stage. The first improvement that comes to mind suggestion would be to build a dedicated User Interface. Each built-in Varian sequence comes with its own dedicated GUI, displaying only the relevant variables and parameters, simplifying the whole experience and preventing, or at the very least reducing the number of possible mistakes. This simplification makes it possible to use most sequences without any prior experience or detailed knowledge about the inner workings of each specific sequence. As every experiment that used the SATSP sequence was done under both mine and Dr. Maurits Jansen supervision, there wasn't an urgent need to build this simplified and dedicated user interface, meaning its implementation kept being constantly postponed. In retrospective, it would have been wiser and more practical to build it in parallel with the sequence itself, avoiding the annoyance of going back and forth between two different sequence layouts during the actual experiments, which can cause quite a bit of confusion after some time. Still, even if the GUI implementation constitutes the most obvious suggestion, it is definitely not the most important.

Looking at it on a more technical level, it would have been very interesting to see if the gradient crushers applied directly after the saturation pulse had any effect in the acquired results. For this idea to be tested one would have to use the SATSP sequence with and without the gradient crushers, under the exact same conditions and parameters for both acquisitions. As the original idea for this modified sequence was to implement a regular, localized saturation pulse before the usual excitation pulse, the concept of not using gradient crushers wasn't even put into consideration while the code was being written/modified, or even after the first few experiments. This apparently small lapse proved itself to be quite troublesome. As the first pulse was defined as a saturation pulse, gradient crushers are on by default. Simply erasing the gradient references from the code would either cause the sequence to not compile or absolutely no effect at all (depending on how bluntly you did it). Again, as it was not deemed severely important, and its implementation was not as straightforward as initially imagined, the idea was put on hold. Nevertheless, if one were to implement it: In theory, the easiest way to take the gradient crushers out of the whole equation would be to define the first, saturation pulse as a regular RF pulse, without using the saturation band function. This way, the gradient crushers wouldn't be directly attached to the pulse function. Again, and while it does sound simple when put this way, there might be some trouble as you can't simply call the *shapedpulse* function multiple times as only the last instance will remain active. Nevertheless, it does not seem like an overly complicated task, and I believe it should be part of further optimization.

13. Conclusion

As it was shown, Magnetic Resonance Spectroscopy can be considered a promising technique to simultaneously detect and quantify, in a non-invasive way, several cytosolic phosphorous-containing compounds involved in energy metabolism and membrane phospholipid metabolism.

All things considered there is still an awful lot of work that can be done to complement, enhance and continue this investigation, some of it mentioned in the previous chapter. Hopefully this report will help whoever tries to go along the same path.

14. Appendix

14.1 SATSP pulse sequence

```
#ifndef LINT
static char SCCSid[] = "modified SPULS/PRESS with saturation bands";
#endif
/*
 * Varian,Inc. All Rights Reserved.
 * This software contains proprietary and confidential
 * information of Varian, Inc. and its contributors.
 * Use, disclosure and reproduction is prohibited without
 * prior consent.
 */
/*********************************************************************
  SPULS + Saturation Slices

*********************************************************************/

#include <standard.h>
#include "sgl.c"


pulsesequence()
{
  /***** Internal variable declarations *****/
  double te_d1,te_d2,te_d3;             /* delays */
  double tr_delay;
  double freq1,freq2,freq3;
  char    volumercv[MAXSTR];


  get_parameters();
  get_ovsparameters();

  initparms_sis();  /* initialize standard imaging parameters */

  getstr("volumercv",volumercv);

  te2 = getvalnwarn("te2");

  /***** RF power calculations *****/
  init_rf(&p1_rf,p1pat,p1,flip1,rof1,rof2);
  init_rf(&p2_rf,p2pat,p2,flip2,rof1,rof2);
  calc_rf(&p1_rf,"tpwr1","tpwr1f");
  calc_rf(&p2_rf,"tpwr2","tpwr2f");

  /***** Initialize gradient structs *****/
  init_slice(&vox1_grad,"vox1",vox1);
  init_slice_refocus(&vox1r_grad,"vox1r");

  /***** Gradient calculations *****/
  calc_slice(&vox1_grad,&p1_rf,WRITE,"gvox1");
  calc_slice_refocus(&vox1r_grad,&vox1_grad,WRITE,"gvox1r");

  if (vox1_grad.rfDelayFront < 0.2e-6) vox1_grad.rfDelayFront = 0;
  if (vox1_grad.rfDelayBack  < 0.2e-6) vox1_grad.rfDelayBack  = 0;


  /* Optional Outer Volume Suppression and Saturation Bands */
  if (ovs[0] == 'y')  create_ovsbands();
  if (sat[0] == 'y')  create_satbands();

  /***** Min TR *****/
  trmin = 4e-6 + at;

  if (ovs[0] == 'y') trmin += ovsTime;
  if (sat[0] == 'y') trmin += satTime;

  if (mintr[0] == 'y') {
    tr = trmin+4e-6;  // ensure at least 4us between gradient events
    putvalue("tr",tr);
```

```
69    }
70    if (tr < trmin+4e-6) {
71      abort_message("tr too short. Minimum tr = %.2f ms\n",(trmin+4e-6)*1000);
72    }
73
74    /***** Calculate TR delay *****/
75    tr_delay = tr - trmin;
76
77
78    /* Frequency offsets */
79    freq1     = poffset(pos1,vox1_grad.ssamp); // First  RF pulse
80    roff      = resto-tof;    // receiver frequency, delta from transmitter
81    tof=5500;
82
83
84    /* Put gradient information back into VnmrJ parameters */
85    putvalue("gvox1",vox1_grad.ssamp);
86
87    putvalue("rgvox1",vox1_grad.tramp);
88
89    putvalue("tvox1",vox1r_grad.duration);
90    putvalue("rgvox1r",vox1r_grad.tramp);
91
92
93    sgl_error_check(sglerror);
94
95
96    /* Relaxation delay ***********************************/
97    status(A);
98    obsoffset(resto);
99    delay(4e-6);
100   rot_angle(vpsi,vphi,vtheta);
101   xgate(ticks);
102
103   if (ix == 1) grad_advance(tep);
104
105   /* Saturation bands ***********************************/
106   if (ovs[0] == 'y') ovsbands();
107   if (sat[0] == 'y') satbands();
108   delay(4e-6);
109
110   /* Slice selective 90 degree RF pulse *****/
111
112   obspower(tpwr);
113
114    shapedpulse(pwpat,pw,oph,rof1,rof2);
115
116    startacq(alfa);
117    acquire(np,(1.0/sw));
118    endacq();
119
120   delay(tr_delay);
121
122 }
```

14.2 Flip Angle map generation in matlab

```
/* Matlab code for B1 map generation (example) */

i40 = imread('NaP 1024av 40deg.jpg');
i80 = imread('NaP 1024av 80deg.jpg');
i40 = double(i40);
i80 = double(i80);

FA = zeros(128,128);
T = 45;

ii40 = 2*i40;

for i = 1:1:128;
    for j =1:1:128;

        if  ii40(i,j) < T
          ii40(i,j) = 1;
        end

        if  i80(i,j) < T
          i80(i,j) = 1;
        end

        FA(i,j) = acosd(i80(i,j)/ii40(i,j));
    end
end

FAR = real(FA);
for i = 1:1:128;
    for j =1:1:128;
        if  FAR(i,j) > 80
          FAR(i,j) = 1;
        end
    end
end

imagesc(FAR, [20,70]);
```

15.References

[1]
P. Rossi, P. Ricci, and L. Broglia, *Portal Hypertension: Diagnostic Imaging and Imaging-guided Therapy ; with 49 Tables*. Springer Science & Business Media, 2000.

[2]
R. N. Anderson and B. L. Smith, "Deaths: leading causes for 2001,"*Natl Vital Stat Rep*, vol. 52, no. 9, pp. 1–85, Nov. 2003.

[3]
L. Castéra, J. Vergniol, J. Foucher, B. Le Bail, E. Chanteloup, M. Haaser, M. Darriet, P. Couzigou, and V. De Lédinghen, "Prospective comparison of transient elastography, Fibrotest, APRI, and liver biopsy for the assessment of fibrosis in chronic hepatitis C,"*Gastroenterology*, vol. 128, no. 2, pp. 343–350, Feb. 2005.

[4]
I. R. Corbin, R. Buist, J. Peeling, M. Zhang, J. Uhanova, and G. Y. Minuk, "Hepatic 31P MRS in rat models of chronic liver disease: assessing the extent and progression of disease," *Gut*, vol. 52, no. 7, pp. 1046–1053, Jul. 2003.

[5]
M. Ronot, S. A. Lambert, M. Wagner, P. Garteiser, S. Doblas, M. Albuquerque, V. Paradis, V. Vilgrain, R. Sinkus, and B. E. Van Beers, "Viscoelastic Parameters for Quantifying Liver Fibrosis: Three-Dimensional Multifrequency MR Elastography Study on Thin Liver Rat Slices," *PLoS ONE*, vol. 9, no. 4, p. e94679, Apr. 2014.

[6]
H. J. Alter, Y. Nakatsuji, J. Melpolder, J. Wages, R. Wesley, J. W. Shih, and J. P. Kim, "The incidence of transfusion-associated hepatitis G virus infection and its relation to liver disease," *N. Engl. J. Med.*, vol. 336, no. 11, pp. 747–754, Mar. 1997.

[7]
K. K. Changani, B. J. Fuller, D. J. Bryant, J. D. Bell, M. Ala-Korpela, S. D. Taylor-Robinson, D. P. Moore, and B. R. Davidson, "Non-invasive assessment of ATP regeneration potential of the preserved donor liver. A 31P MRS study in pig liver," *J. Hepatol.*, vol. 26, no. 2, pp. 336–342, Feb. 1997.

[8]
E. M. Haacke, R. W. Brown, M. R. Thompson, and R. Venkatesan,*Magnetic Resonance Imaging: Physical Principles and Sequence Design*, 1st edition. New York: Wiley-Liss, 1999.

[9]
C. Westbrook, C. K. Roth, and J. Talbot, *MRI in Practice*, 4th Edition edition. Chichester, West Sussex ; Malden, MA: Wiley-Blackwell, 2011.

[10]
M. A. Flower, *Webb's Physics of Medical Imaging, Second Edition*. CRC Press, 2012.

[11]
V. Kuperman, *Magnetic Resonance Imaging: Physical Principles and Applications*. Academic Press, 2000.

[12]
J. C. Maxwell and F. Jenkin, "LXI. On the elementary relations between electrical measurements," *Philosophical Magazine Series 4*, vol. 29, no. 198, pp. 436–460, Jun. 1865.

[13]
F. Bloch, R. I. Condit, and H. H. Staub, "Neutron Polarization and Ferromagnetic Saturation," *Phys. Rev.*, vol. 70, no. 11–12, pp. 972–973, Dec. 1946.

[14]
R. A. de Graaf, *In Vivo NMR Spectroscopy: Principles and Techniques*, 2nd Edition edition. Chichester, West Sussex, England ; Hoboken, NJ: Wiley-Blackwell, 2007.

[15]
Lebon V, Petersen KF, Cline GW, Shen J, Mason GF, Dufour S, Behar KL, Shulman GI, Rothman DL. Astroglial contribution to brain energy metabolism in humans revealed by 13C nuclear magnetic resonance spectroscopy: elucidation of the dominant pathway for neurotransmitter glutamate repletion and measurement of astrocytic oxidative metabolism. J Neurosci 22, 1523–1531 (2002).

[16]
Bluml S, Moreno-Torres A, Shic F, Nguy CH, Ross BD. Tricarboxylic acid cycle of glia in the in vivo human brain. NMR Biomed 15, 1–5 (2002).

[17]
Blakely RD, Coyle JT. The neurobiology of N-acetylaspartylglutamate. *Int Rev Neurobiol* 30, 39–100 (1988).

[18]
H. Van As and D. van Dusschoten, "NMR methods for imaging of transport processes in micro-porous systems," *Geoderma*, vol. 80, no. 3–4, pp. 389–403, Nov. 1997.

[19]
G. R. Morrell, “A phase-sensitive method of flip angle mapping,” *Magn. Reson. Med.*, vol. 60, no. 4, pp. 889–894, Oct. 2008.

[20]
C. H. Cunningham, K. S. Nayak, and J. M. Pauly, “RF field mapping for magnetic resonance imaging,” US7446526 B2, 04-Nov-2008.

[21]
L. I. Sacolick, F. Wiesinger, I. Hancu, and M. W. Vogel, “B1 Mapping by Bloch-Siegert Shift,” *Magn Reson Med*, vol. 63, no. 5, pp. 1315–1322, May 2010.

[22]
R. Stollberger and P. Wach, “Imaging of the active B1 field in vivo,”*Magn. Reson. Med.*, vol. 35, no. 2, pp. 246–251, Feb. 1996.

[23]
R. Treier, A. Steingoetter, M. Fried, W. Schwizer, and P. Boesiger, “Optimized and combined T1 and B1 mapping technique for fast and accurate T1 quantification in contrast-enhanced abdominal MRI,” *Magn. Reson. Med.*, vol. 57, no. 3, pp. 568–576, Mar. 2007.

[24]
“Section 5.5: Spin-spin coupling,” *chemwiki.ucdavis.edu*. [Online]. Available: http://chemwiki.ucdavis.edu/Organic_Chemistry/Organic_Chemistry_With_a_Biological_Emphasis/Chapter_05%3A_Structure_Determination_II/Section_5.5%3A_Spin-spin_coupling. [Accessed: 11-Oct-2014].

[25]
R. Issa, X. Zhou, N. Trim, H. Millward-Sadler, S. Krane, C. Benyon, and J. Iredale, “Mutation in collagen-1 that confers resistance to the action of collagenase results in failure of recovery from CCl4-induced liver fibrosis, persistence of activated hepatic stellate cells, and diminished hepatocyte regeneration,” *FASEB J*, vol. 17, no. 1, pp. 47–49, 2003.

[26]
J. P. Iredale, “Hepatic Stellate Cell Behavior during Resolution of Liver Injury,” *Seminars in Liver Disease*, vol. 21, no. 03, pp. 427–436, 2001.

[27]
F. Ursini, M. Maiorino, M. Valente, L. Ferri, and C. Gregolin, “Purification from pig liver of a protein which protects liposomes and biomembranes from peroxidative degradation and exhibits glutathione peroxidase activity on phosphatidylcholine hydroperoxides,” *Biochimica et Biophysica Acta (BBA) - Lipids and Lipid Metabolism*, vol. 710, no. 2, pp. 197–211, Feb. 1982.

[28]
Y. Kamada, S. Tamura, S. Kiso, H. Matsumoto, Y. Saji, Y. Yoshida, K. Fukui, N. Maeda, H. Nishizawa, H. Nagaretani, Y. Okamoto, S. Kihara, J. Miyagawa, Y. Shinomura, T. Funahashi, and Y. Matsuzawa, “Enhanced carbon tetrachloride-induced liver fibrosis in mice lacking adiponectin,” *Gastroenterology*, vol. 125, no. 6, pp. 1796–1807, Dec. 2003.

[29]
G. Vendemiale, I. Grattagliano, M. L. Caruso, G. Serviddio, A. M. Valentini, M. Pirrelli, and E. Altomare, “Increased Oxidative Stress in Dimethylnitrosamine-Induced Liver Fibrosis in the Rat: Effect of N-Acetylcysteine and Interferon-α,” *Toxicology and Applied Pharmacology*, vol. 175, no. 2, pp. 130–139, Sep. 2001.

[30]
“Systemic Infusion of FLK1+ Mesenchymal Stem Cells Ameliorate... : Transplantation.” [Online]. Available:http://journals.lww.com/transplantjournal/Fulltext/2004/07150/Systemic_Infusion_of_FLK1__Mesenchymal_Stem_Cells.14.aspx. [Accessed: 11-Oct-2014].

[31]
C. Constandinou, N. Henderson, and J. P. Iredale, “Modeling Liver Fibrosis in Rodents,” in *Fibrosis Research*, J. Varga, D. A. Brenner, and S. H. Phan, Eds. Totowa, NJ: Humana Press, 2005, pp. 237–250.

[32]
A. Canbay, S. Friedman, and G. J. Gores, “Apoptosis: The nexus of liver injury and fibrosis,” *Hepatology*, vol. 39, no. 2, pp. 273–278, Feb. 2004.

[33]
P. Hammel, A. Couvelard, D. O’Toole, A. Ratouis, A. Sauvanet, J. F. Fléjou, C. Degott, J. Belghiti, P. Bernades, D. Valla, P. Ruszniewski, and P. Lévy, “Regression of Liver Fibrosis after Biliary Drainage in Patients with Chronic Pancreatitis and Stenosis of the Common Bile Duct,” *New England Journal of Medicine*, vol. 344, no. 6, pp. 418–423, Feb. 2001.

[34]
P. de la M Hall, C. S. Lieber, L. M. DeCarli, S. W. French, K. O. Lindros, H. Järveläinen, C. Bode, A. Parlesak, and J. C. Bode, “Models of alcoholic liver disease in rodents: a critical evaluation,” *Alcohol. Clin. Exp. Res.*, vol. 25, no. 5 Suppl ISBRA, p. 254S–261S, May 2001.

[35]
P. P. Simeonova, R. M. Gallucci, T. Hulderman, R. Wilson, C. Kommineni, M. Rao, and M. I. Luster, “The Role of Tumor Necrosis Factor-α in Liver Toxicity, Inflammation, and Fibrosis Induced by Carbon Tetrachloride,” *Toxicology and Applied Pharmacology*, vol. 177, no. 2, pp. 112–120, Dec. 2001.

[36]
S. Sawada, K. Murakami, J. Murata, K. Tsukada, and I. Saiki, "Accumulation of extracellular matrix in the liver induces high metastatic potential of hepatocellular carcinoma to the lung," *International Journal of Oncology*, vol. 19, no. 1, pp. 65–70, Jul. 2001.

[37]
J. A. Fallowfield and J. P. Iredale, "Targeted treatments for cirrhosis,"*Expert Opin. Ther. Targets*, vol. 8, no. 5, pp. 423–435, Oct. 2004.

[38]
Y. N. Kallis, A. J. Robson, J. A. Fallowfield, H. C. Thomas, M. R. Alison, N. A. Wright, R. D. Goldin, J. P. Iredale, and S. J. Forbes, "Remodelling of extracellular matrix is a requirement for the hepatic progenitor cell response," *Gut*, vol. 60, no. 4, pp. 525–533, 2011.

[39]
J. A. Fallowfield, "Therapeutic targets in liver fibrosis," *American Journal of Physiology - Gastrointestinal and Liver Physiology*, vol. 300, no. 5, pp. G709–G715, May 2011.

[40]
A. Pellicoro, P. Ramachandran, J. P. Iredale, and J. A. Fallowfield, "Liver fibrosis and repair: immune regulation of wound healing in a solid organ," *Nat Rev Immunol*, vol. 14, no. 3, pp. 181–194, Mar. 2014.

[41]
"Laboratory rat," *Wikipedia, the free encyclopedia*. 11-Oct-2014.

[42]
O. D. Bengt Noren, "Separation of advanced from mild fibrosis in diffuse liver disease using 31P magnetic resonance spectroscopy" *European journal of radiology*, vol. 66, no. 2, pp. 313–20, 2008.

[43]
J. D. Bell, I. J. Cox, J. Sargentoni, C. J. Peden, D. K. Menon, C. S. Foster, P. Watanapa, R. A. Iles, and J. Urenjak, "A 31P and 1H-NMR investigation in vitro of normal and abnormal human liver," *Biochim. Biophys. Acta*, vol. 1225, no. 1, pp. 71–77, Nov. 1993.

[44]
A. Kumar and P. A. Bottomley, "Optimized quadrature surface coil designs," *MAGMA*, vol. 21, no. 1–2, pp. 41–52, Mar. 2008.

[45]
R. J. Ordidge, A. Connelly, and J. A. B. Lohman, "Image-selected in Vivo spectroscopy (ISIS). A new technique for spatially selective nmr spectroscopy," *Journal of Magnetic Resonance (1969)*, vol. 66, no. 2, pp. 283–294, Feb. 1986.

[46]
S. S. Rajan, "MRI Hardware System Components," in *MRI*, Springer New York, 1998, pp. 25–39.

[47]
J. P. Hannon, "Effect of Temperature on the Heart Rate, Electrocardiogram and Certain Myocardial Oxidations of the Rat,"*Circulation Research*, vol. 6, no. 6, pp. 771–778, 1958.

[48]
X. He and D. A. Yablonskiy, "Biophysical mechanisms of phase contrast in gradient echo MRI," *PNAS*, vol. 106, no. 32, pp. 13558–13563, 2009.

[49]
Vanhamme, van den Boogaart A, and Van Huffel S, "Improved method for accurate and efficient quantification of MRS data with use of prior knowledge," *J. Magn. Reson.*, vol. 129, no. 1, pp. 35–43, Nov. 1997.

[50]
J. Weis, L. Johansson, F. Ortiz-Nieto, and H. Ahlström, "Assessment of lipids in skeletal muscle by LCModel and AMARES," *J Magn Reson Imaging*, vol. 30, no. 5, pp. 1124–1129, Nov. 2009.

[51]
D. E. Bohning, A. C. Wright, and K. M. Spicer, "In vivo phosphorus spectroscopy of human skin," *Magn. Reson. Med.*, vol. 35, no. 2, pp. 186–193, Feb. 1996.

[52]
"Plastic Properties of Acrylonitrile Butadiene Styrene (ABS)," *www.dynalabcorp.com* [Online]. Available: http://www.dynalabcorp.com/technical_info_abs.asp. [Accessed: 11-Oct-2014].

[53]
"Chemical Database" www.chemspider.com [Online]

[54]
C. J. Cooksey, E. J. Land, and P. A. Riley, "A SIMPLE ONE-POT PREPARATION OF 4-ALKOXY-AND 4-ALKYLTHIO-CATECHOLS AND *o* -BENZOQUINONES," *Organic Preparations and Procedures International*, vol. 28, no. 4, pp. 463–467, Aug. 1996.

[55]
K. Schrödter, G. Bettermann, T. Staffel, F. Wahl, T. Klein, and T. Hofmann, “Phosphoric Acid and Phosphates,” in *Ullmann’s Encyclopedia of Industrial Chemistry*, Wiley-VCH Verlag GmbH & Co. KGaA, 2000.

[56]
S. Fortune, M. A. Jansen, T. Anderson, G. A. Gray, J. E. Schneider, P. R. Hoskins, and I. Marshall, “Development and characterization of rodent cardiac phantoms: comparison with in vivo cardiac imaging,”*Magn Reson Imaging*, vol. 30, no. 8, pp. 1186–1191, Oct. 2012.

[57]
G. A. Webb, *Modern Magnetic Resonance: Part 1: Applications in Chemistry, Biological and Marine Sciences, Part 2: Applications in Medical and Pharmaceutical Sciences, Part 3: Applications in Materials Science and Food Science*. Springer Science & Business Media, 2007.

[58]
“Magnetism,” *Questions and Answers in MRI*. [Online]. Available:http://mriquestions.com/adiabatic-pulses.html. [Accessed: 03-Dec-2014].

[59]
B. Norén, P. Lundberg, M. Ressner, S. Wirell, S. Almer, and O. Smedby, “Absolute quantification of human liver metabolite concentrations by localized in vivo 31P NMR spectroscopy in diffuse liver disease,” *Eur Radiol*, vol. 15, no. 1, pp. 148–157, Jan. 2005.